EARTHQUAKES AND THE NEW PARADIGM OF DILUTED CORES IN GAS GIANT PLANETS

Thesis by
Benjamín Rodo Idini Zabala

In Partial Fulfillment of the Requirements for the
Degree of
Doctor of Philosophy

Caltech

CALIFORNIA INSTITUTE OF TECHNOLOGY
Pasadena, California

2022
Defended May 17th, 2022

ACKNOWLEDGEMENTS

iv

anomalies in Juno's data, and hence provided a motivation to most of the work contained in this thesis.

Finally, thanks to all of you who kept it positive by acting like decent people throughout these five years. Happily, the list runs so long that I would feel afraid of forgetting some of your names. I'm referring mainly to the supportive group of Planetary Science students, the Planet Haus (a.k.a. Greenwood estate), the Skiing Crew, and the Keck Institute for Space Studies cohort, to name a few. We shall meet again soon 8).

ABSTRACT

In this thesis, I present results on two distinct topics within geophysics: earthquake mechanics and the core of gas giant planets. A common element connecting this work is the similar research approach that I use to address each topic. Each chapter in this thesis attempts to provide a simple physical understanding on the fundamental aspects relevant to the system in question. Further, I use numerical models to expand my arguments in some cases, while in others I build up my case with mathematical modeling only.

Chapters II-IV focus on the gravitational field of Jupiter and connect radio science observations from NASA's Juno mission to the structure of Jupiter's dilute core. In Chapter II, I use dynamical tides to interpret a nonhydrostatic component in Jupiter's degree-2 tidal response—represented by the Love number k_2—observed by Juno at the mid-mission perijove (PJ) 17. The results presented here show how the Coriolis acceleration contributes with a dynamical effect to Jupiter's tidal response, providing a satisfactory fit to Juno's observed k_2. From these results, I conclude that Juno obtained the first unambiguous detection of the gravitational effect of dynamical tides in a gas giant planet.

In Chapter III, I build a perturbation theory to show that the high-degree tidal gravitational field of Jupiter is dominated by spherical harmonic coupling promoted by Jupiter's oblate figure as forced by the centrifugal effect. Based on this novel understanding of Jupiter's high-degree tidal gravitational field, I establish that Juno observed a 7σ nonhydrostatic component in k_{42} at mid-mission.

In Chapter IV, I invoke a core-orbital resonance between internal gravity waves trapped in Jupiter's dilute core and the orbital motion of Io to explain the 7σ nonhydrostatic component in the high-degree tidal response of Jupiter as observed by Juno at mid-mission—namely the Love number k_{42}. These results suggest that an extended dilute core in Jupiter ($r \gtrsim 0.7R_{Jup}$) reconciles the k_{42} nonhydrostatic component. This explanation of Juno's observation requires two ingredients: a dilute core in Jupiter that becomes smoother or shrinks over geological time, alongside with a high amount of dissipation provided by resonantly excited internal gravity waves.

In Chapter V, I connect observations of earthquake modes of propagation to the damaged rock often found around tectonic fault zones. Previous work showed

that pulse-like rupture—a propagation mode where slip propagates as a narrow pulse—can be induced by the dynamic effect of seismic waves reflected at the boundary of a cavity formed by the damaged material in fault zones. My main result shows that pulses are easier to produce than previously thought; pulses can appear in a highly damaged fault zone even in the absence of reflected seismic waves. In addition, these results provide a new explanation for back-propagating rupture fronts recently observed during large earthquakes and the rapid-tremor-reversal slip patterns observed in Cascadia and Japan.

In summary, the results contained in these four chapters advance our knowledge in fundamental problems related to geophysics. In relation to gas giant planets, my results include the development of a novel technique to reveal the structure of Jupiter's core using spacecraft observations of the tidal gravitational field. In relation to earthquakes, my results connect earthquake ruptures to observable fault zone properties.

PUBLISHED CONTENT AND CONTRIBUTIONS

B. Idini and J.-P. Ampuero. Fault-zone damage promotes pulse-like rupture and back-propagating fronts via quasi-static effects. *Geophysical Research Letters*, 47(23):e2020GL090736, 2020. doi:10.1029/2020GL090736.
B.I. contributed to the determination of the project's direction; performed numerical simulations, scaling arguments, and analysis to generate results; implemented new software features; and led the writing of the manuscript. This work was adapted to constitute Chapter V.

B. Idini and D. J. Stevenson. Dynamical tides in Jupiter as revealed by Juno. *The Planetary Science Journal*, 2(2):69, 2021. doi:10.3847/PSJ/abe715.
B.I. contributed to the determination of the project's direction, developed the mathematical theory, implemented numerical calculations, performed analysis to generate results, and led the writing of the manuscript. This work was adapted to constitute Chapter II.

B. Idini and D. J. Stevenson. The gravitational imprint of an interior–orbital resonance in Jupiter–Io. *The Planetary Science Journal*, 3(4):89, 4 2022a. doi:10.3847/PSJ/ac6179.
B.I. conceived of the project's primary objective, performed calculations and analysis to generate results, and led the writing of the manuscript. This work was adapted to constitute Chapter IV.

B. Idini and D. J. Stevenson. The lost meaning of Jupiter's high-degree Love numbers. *The Planetary Science Journal*, 3(1):11, 1 2022b. doi:10.3847/PSJ/ac4248.
B.I. contributed to the conception of the project, developed the mathematical theory, performed analysis to generate results, and led the writing of the manuscript. This work was adapted to constitute Chapter III.

TABLE OF CONTENTS

LIST OF ILLUSTRATIONS

LIST OF TABLES

C h a p t e r   1

INTRODUCTION

> *"The universe is made of stories, not of atoms."*
>
> — Muriel Rukeyser, *The Speed of Darkness*

Planets keep the secrets of the formation of planetary systems concealed in their deep interiors. The planetary scientist attempts to reveal such secrets, illuminating the materials and structures that define what a planet looks like deep below its crust or atmosphere. In such effort, the planetary scientist develops theories and models to connect observations obtained outside the planet to properties and processes active within the planet. Without such observations, the planetary scientist can hardly make any progress.

Since decades NASA has led humanity in exploring our solar system and beyond. The most distant planet in the solar system, Neptune, lies only a couple of decades away from NASA's reach assuming conventional spacecraft travel. This proximity allows NASA to routinely visit solar system planets and collect in situ observations using a diverse fleet of orbiters, probes, and rovers.

In situ observations hold the key to expose a planet's interior. In that sense, the best known planetary interior is our own Earth's. The measurement and analysis of Earth's vibrations provide enough information to reveal Earth's layered structure from its silicate crust to its solid iron core.

In situ observations also reveal the interior structure of the fluid giant planets (also known, perhaps imprecisely, as gas giant planets). These planets do not posses a solid surface from where to measure planetary vibrations. Alternatively, a ring system traps planetary vibrations in the case of Saturn, revealing that the planet's core has a fuzzy structure (also known as diluted core) rather than a distinct boundary like Earth's core. In Jupiter, the biggest planet in the solar system, the ring system is too faint and fails to record the planet's vibrations. Revealing Jupiter's interior requires another kind of in situ observation; for example, gravity.

In situ gravity observations of Jupiter's response to rotation suggest that Jupiter may host a diluted core, just like Saturn does. But contrary to Saturn's case, the radial extension of Jupiter's diluted core is poorly constrained. Unlike ring seismology,

the precision of the traditional gravity analysis depends on a precise description of the behavior of high-pressure hydrogen and helium, which is currently uncertain. A new mission concept to measure Jupiter's vibrations could settle the matter of the extension of Jupiter's dilute core. In the meantime, gravity remains one of the best available options to reveal Jupiter's interior.

This thesis explores the potential of using Jupiter's response to tidal forces to aliviate some of the limitations of a traditional gravity analysis. It contains my contribution to detect and characterize Jupiter's core from the tidal gravity field observed in situ by NASA's Juno mission. The main question I try to answer in this thesis is: what kind of core does Jupiter have? One end member core model concentrates the core material near the center in what is traditionally known as a compact core (Fig. 1.1). Another end member distributes the core material broadly along the planetary radius in what is emerging in recent years as the new paradigm of diluted cores in gas giant planets (Fig. 1.1).
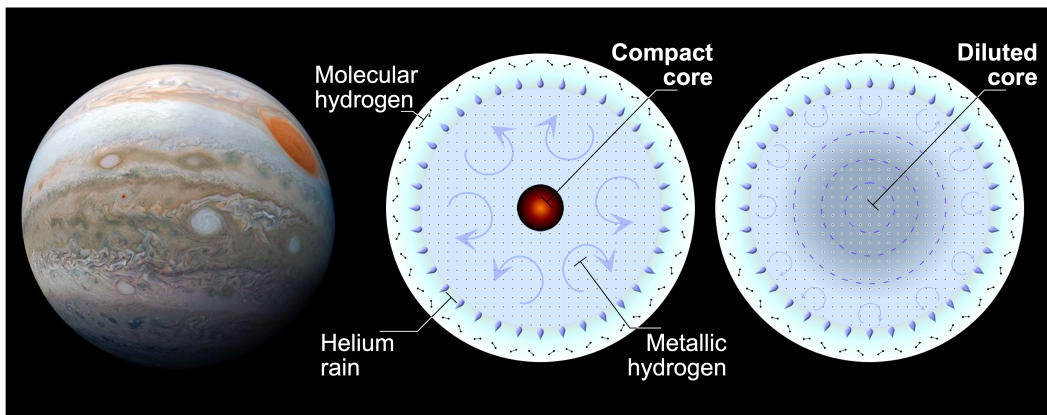
Figure 1.1: Schematic of two end member Jupiter core models.

In particular, here I develop theory and models that interpret anomalies in the tidal gravity field raised by the Galilean satellites on Jupiter. The tidal gravity field is advantageous to study Jupiter's interior in that it is small compared to the total gravity field of the planet. Consequently, perturbation theory provides an excellent approximation to represent the tidal gravity field, allowing us to simplify the mathematical understanding of the problem and circumvent the demand of precisely knowing the behavior of high-pressure hydrogen and helium.

The gravity anomalies mentioned here correspond to anomalies in Doppler shifts from the navigation data provided by a Ka-band antenna on board the Juno spacecraft. At every close encounter with Jupiter, Juno acts like a test particle perturbed

by Jupiter's gravitational field. While Juno flies at full speed through Jupiter's heterogeneous gravity field, the trajectory followed by the spacecraft generates Doppler shifts on radio signals that continuously interrogate Juno's Ka-band antenna with the Earth-based antennas from NASA's Deep Space Network. An analysis of the Doppler shift data recovers the gravity field required to explain Juno's trajectory.

I interpret this tidal gravity anomalies to be the dynamical component of Jupiter tides. In general for a planet-satellite system, the highest tide corresponds to the tidal bulge that balances the gravity perturbation of the satellite mass, namely the equilibrium tide (i.e., $\sum F = 0$). A dynamical tide perturbs the tidal bulge out of equilibrium due to dynamical effects that are frequency dependent (i.e., $\sum F = ma$). Formally, I define

$$\Delta k = \frac{k}{k_{eq}} - 1, \tag{1.1}$$

where the Love number k represents the nondimensional amplitude of tidal gravity, k_{eq} is the equilibrium tide, and Δk is the deviation from equilibrium tides due to dynamical tides.

Dynamical tides perturb the equilibrium tide depending on the tidal frequency, following a qualitative fashion that resembles the response of the harmonic oscillator (Fig. 1.2). A far-out satellite produces a negligible dynamical tide because the tidal frequency is almost zero. On the contrary, a satellite can resonate with the normal oscillations of the host planet, leading to large amplitude dynamical tides. Given complications in the equation of the tidal flow, the harmonic oscillator only constitutes a qualitative model. Tidal resonances can produce either positive or negative perturbations from the equilibrium tide depending on the specific character of the relevant host planet normal oscillation.

The work presented here concentrates in what may seem like mere details about one single planet in the universe. What is the merit in studying one single planet when we know of the existence of more than 5,000 others? Beyond our solar system, space exploration seems daunting. It would take a conventional spacecraft more than 70,000 years to reach Proxima Centauri, the closest star to our sun. The scarce number of photons that highly sophisticated telescopes struggle to capture say barely enough to constrain those distant planet's mass and radius. In some favorable cases, they may even provide rudimentary information about the composition and dynamics of the planetary atmosphere. However, in the absence of in situ observations, the deep interiors of this new multitude of planets may remain a mystery.
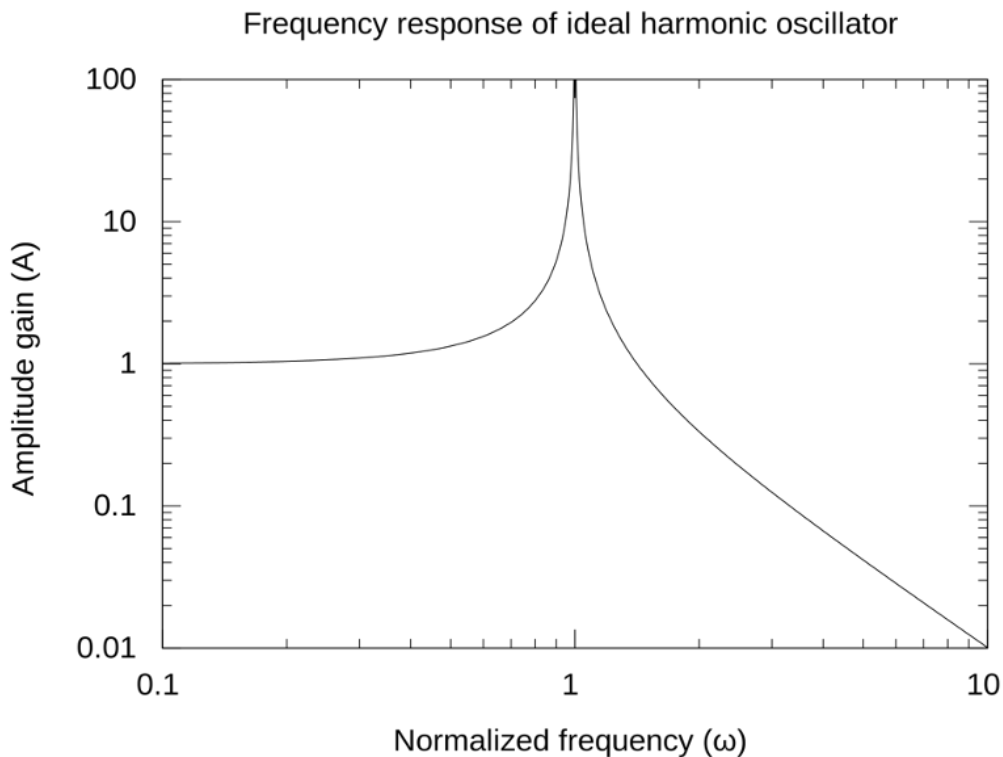
Figure 1.2: The frequency-dependent response of the ideal harmonic oscillator, a qualitative model for dynamical tides.

In this scenario, the solar system planets represent the ground truth to understand the interiors and formation of planets in the universe at large. These eight planets are the only places we can actually visit and understand to the similar degree we currently understand Earth. Any hypothetical general theory of planet formation would need first to explain these eight planets, which interiors remain to this day a largely unexplored frontier. Thus, more than ever understanding our place in the universe requires of space exploration. We live (still) in the infancy of an exploration era.

The rest of this thesis is organized as follows. In Chapter II, I provide a first approach to the gravitational signature of dynamical tides in a gas giant planet. This chapter introduces the use of perturbation theory to represent tidal gravity employed in Chapters II-IV. It also covers the intimate relationship between normal mode oscillations and tidal gravity using simple intuitive models. The main result in this chapter comes from unequivocally classifying a gravity anomaly detected by Juno as the gravitational effect of dynamical tides associated to Jupiter's fundamental mode

of oscillation. Our theory illuminates in detail the structure of the flow that leads to a -4% reduction in tidal gravity, mainly as a result of the Coriolis acceleration. In my simple perturbation theory, I find a compelling answer to the puzzling requirement of a negative dynamical effect when a simple harmonic oscillator predicts a positive dynamical effect.

Chapter III contains an attractive theoretical result for the reader interested in tidal theory and simple dynamical models. I again develop a perturbation theory to illuminate puzzling numerical results previously obtained by another group. Our main result defies the centenary tradition of using Love numbers to describe the tidal response of a fluid body. Our theory shows how the oblate figure of a rapidly rotating fluid body couples the tidal response at spherical harmonics of various degree ℓ. The result is that high-degree Love numbers are dominated by the tidal response at lower degree. As a consequence, the tidal response at high-degree attenuates less rapidly than the tidal forcing, causing an increment in the high-degree Love number with satellite semi-major axis that does not correspond to an increased tidal gravity field. An implication of this theory is that the often neglected tidal torque produced by the high-degree tidal bulge may play a sensitive role in satellite orbital migration.

To close my work on Jupiter dynamical tides, Chapter IV integrates the lessons learned in previous chapters to propose that an extended dilute core in Jupiter explains a gravity anomaly on the high-degree tidal gravity as recorded by Juno at mid-mission. In our proposed scenario, Jupiter's diluted core resonates with the tides raised by Io, leading to resonant internal gravity waves that significantly perturb Jupiter's tidal response and Io's orbital migration rate. I discuss that such a resonant state may be sustained over long geological timescales via resonant locking. An important prediction made in our scenario is that Jupiter possesses a normal mode of oscillation with frequency ~ 270 μHz and a Jupiter Love number k_{42} caused by Europa that is close to the equilibrium tide $k_{42} = 4.2$. The first prediction requires a seismological campaign/mission and the second prediction may be testable by Juno at the end of the mission.

In Chapter V, the last chapter in my thesis, I swerve off from the outer solar system to dive back into Earth. This chapter contains the results of my initial years of doctorate research in earthquake mechanics. Here I extend previous work on a numerical tool to simulate fault slip in an elastic and heterogenous medium that represents the damaged fault zones observed in strike-slip geological faults around the world. In a parametric exploration, I find that heavily damaged faults produce earthquake

pulses and back-propagating fronts that persist over multiple earthquake cycles. The results in this chapter strengthen the hypothesis that observable fault structure can modulate patterns of earthquake slip and explain some of the complexity observed in nature from simple mechanical ingredients.

Chapter 2

DYNAMICAL TIDES IN JUPITER AS REVEALED BY JUNO

"The tide is high but I'm holding on,
I'm gonna be your number one."
— The Paragons, *The Tide is High*

B.I. contributed to the determination of the project's direction, developed the mathematical theory, implemented numerical calculations, performed analysis to generate results, and led the writing of the manuscript. This work was adapted to constitute Chapter II.

2.1 Abstract

The Juno orbiter continues to collect data on Jupiter's gravity field with unprecedented precision since 2016, recently reporting a non-hydrostatic component in the tidal response of the planet. At the mid-mission perijove 17, Juno registered a Love number $k_2 = 0.565 \pm 0.006$ that is $-4 \pm 1\%$ (1σ) from the theoretical hydrostatic $k_2^{(hs)} = 0.590$. Here we assess whether the aforementioned departure of tides from hydrostatic equilibrium represents the neglected gravitational contribution of dynamical tides. We employ perturbation theory and simple tidal models to calculate a fractional dynamical correction Δk_2 to the well-known hydrostatic k_2. Exploiting the analytical simplicity of a toy uniform-density model, we show how the Coriolis acceleration motivates the negative sign in the Δk_2 observed by Juno. By simplifying Jupiter's interior into a coreless, fully convective, and chemically homogeneous body, we calculate Δk_2 in a model following an $n = 1$ polytrope equation of state. Our numerical results for the $n = 1$ polytrope qualitatively follow the behavior of the uniform-density model, mostly because the main component of the tidal flow is similar in each case. Our results indicate that the gravitational effect of the Io-induced dynamical tide leads to $\Delta k_2 = -4 \pm 1\%$, in agreement with the non-hydrostatic component reported by Juno. Consequently, our results suggest that Juno obtained the first unambiguous detection of the gravitational effect of dynamical tides in a gas giant planet. These results facilitate a future interpretation of Juno tidal gravity data with the purpose of elucidating the existence of a dilute core in Jupiter.

2.2 Introduction

The interior structure of a planet or star closely corresponds with its origin and evolution history. Seismology provides the tightest constraints on the interior structure of Earth (Dahlen and Tromp (1998) and references therein), Saturn (Fuller, 2014; Marley and Porco, 1993), the Sun (Christensen-Dalsgaard et al., 1985), and other distant stars (Aerts et al. (2010) and references therein). In particular, Saturn's ring seismology facilitates estimates of the planet's rotation rate (Mankovich et al., 2019) and possible dilute core (Mankovich and Fuller, 2021; Mankovich, 2020). Unlike Saturn, Jupiter lacks extensive optically thick rings with embedded waves that are excited by resonance of ring particle motions with internal normal modes. As an alternative to ring seismology, Doppler imaging reveals a suggested seismic behavior in Jupiter, limited to radial overtones of p-modes. At best, the current Doppler imaging data resolve the spacing in frequency space of low-order p-modes, providing a loose constraint compatible with simple interior models (Gaulme et al., 2011). Future efforts based on similar techniques promise to reveal additional information on Jupiter's seismic behavior.

In the current absence of detailed seismological constraints, the Juno orbiter (Bolton et al., 2017) emerges as the alternative directed to reveal Jupiter's interior by employing gravity field measurements of global-scale motions. Based on radiometric observations, Juno produces two kinds of gravity field measurements sensitive to Jupiter's interior structure: the zonal J_ℓ and tesseral $C_{\ell,m}$ gravity coefficients. The odd $J_{2\ell+1}$ coefficients reflect contributions from zonal flows, including atmospheric zonal winds and zonal flow in the dynamo region. The even $J_{2\ell}$ coefficients contain Jupiter's response to the centrifugal effect responsible for its oblateness, with minor contributions from zonal winds in the atmosphere (Iess et al., 2018) and the dynamo region (Kulowski et al., 2020). A time-dependent subset of $C_{\ell,m}$ coefficients contains Jupiter's tidal response to the gravitational pull from its system of satellites. Closely related to the time-dependent $C_{\ell,m}$, the Love number k represent the non-dimensional gravitational field of tides evaluated at the outer boundary of the planet (Munk and MacDonald, 1960). One common interpretation relates k to the degree of central concentration of the planetary mass (e.g., compressibility of the planetary material or the presence of a core). In a quadrupolar gravitational pull, the leading term in the tidal response relates to the Love number k_2, which corresponds to the $\ell = m = 2$ spherical harmonic.

Following linear perturbation theory, the Love number k_2 breaks down into two

contributions, one hydrostatic and the other dynamic. The hydrostatic k_2 ignores the time dependence of tides. The dynamical tide represents the tidal flow and perturbed tidal bulge solving the traditional equation of motion $F^T = M\ddot{u}$, rather than $F^T = 0$, where F^T is the satellite-induced tidal force, diminished by the opposing self-gravity of the perturbed planet.

Early studies of the Love numbers in the gas giant planets relied on purely hydrostatic theory, assisted by simple thermodynamic principles alongside loosely constrained interior models (Gavrilov and Zharkov, 1977). With the assistance of historical astrometric data, the Cassini mission provided the first occasion to test the accuracy of those first hydrostatic models, finding an ~10% discrepancy between the theoretical and observed k_2 of Saturn (Lainey et al., 2017). The discrepancy was solved after incorporating the oblateness produced by the centrifugal effect into the tidal model, not requiring to invoke the gravitational effects of Saturn dynamical tides. The oblateness produced by the centrifugal effect is large due to Saturn's fast rotation, leading to major higher-order cross-terms neglected in the earlier theory (Wahl et al., 2017a). This effect remains hydrostatic provided that rotation occurs on cylinders, which allows the centrifugal force to be represented as the gradient of a potential (i.e., Chachan and Stevenson (2019)).

Unlike Cassini, the Juno orbiter recently detected a 3σ deviation in Jupiter's observed k_2 from the revised hydrostatic theory that accounts for the interaction of tides with oblateness (Durante et al., 2020; Notaro et al., 2019). Importantly, the difference between the observed k_2 and hydrostatic theory cannot be attributed to a failure to correctly constrain the hydrostatic number. Hydrostatic tides are well constrained (i.e., the k_2 error in Wahl et al. (2020) is ±0.02% of the central value) because the effect of oblateness of the planet on the zonal gravity coefficients $J_{2\ell}$ is known to a high precision by Juno. Juno's non-hydrostatic detection motivates a more careful consideration of neglected effects that contribute to k_2, particularly the gravitational field related to dynamical tides.

Here we evaluate dynamical tides as a potential explanation for Juno's non-hydrostatic detection. We concentrate on the contribution of dynamical tides to the overall gravity field while ignoring their contribution to dissipation. In other words, we implicitly assume that the imaginary part of k_2 is too small to affect our results for the real part, in agreement with observations of the orbital evolution of Io ($Q_2 = -|k_2|/\text{Im}(k_2) \sim 10^5$; Lainey et al. (2009)).

We are motivated in our efforts by the prospect of finding an additional contribution

to k_2 coming from Jupiter's core. A traditional model of a Jupiter-like planet consists of a discreet, highly-concentrated central region of heavy elements (i.e., a core made of rock and ice) surrounded by a chemically homogeneous and adiabatic envelope of hydrogen-rich fluid material (Stevenson, 1982). Jupiter's observed radius indicates a supersolar abudance of heavy elements that accounts for a total of $\sim 20 M_E$. However, whether heavy elements reside in a traditional core or are distributed throughout the envelope is less clear. The observed J_2 and J_4 require some tendency toward central concentration but do not require a traditional core. In a subsequent investigation, we exploit our results of the dynamical tide presented here to answer questions about the origin and evolution of Jupiter by including in our model an enrichment of heavy elements that increases with depth (i.e., a dilute core; Wahl et al. (2017b)). Using the information contained in k_2, we plan to provide answers to the following questions about Jupiter. Whether solid or fluid, does Jupiter have a traditional core? Alternatively, do the heavy elements in Jupiter spread out from the center, forming a dilute core?

The remainder of this manuscript is organized as follows. In Section 2, we describe the Juno non-hydrostatic detection and develop the mathematical formalism used in the calculation of the fractional dynamical correction to k_2. In Section 3, we calculate the fractional dynamical correction to k_2 using simple tidal models, which leads to an unambiguous explanation of the non-hydrostatic Juno detection. In Section 4, we deliver a discussion on the limitations of our analysis, other physical processes potentially altering the Love number k, and future directions of investigation. In Section 5, we outline the conclusions and implications of our study.

2.3   Jupiter's Love number

A correction to the hydrostatic k_2

The main objective of this manuscript is to evaluate the hypothesis that Juno captured a systematic deviation of k_2 from the hydrostatic number and that most of the deviation can be explained by the neglected gravitational effect of dynamical tides. The mean k_2 Juno estimate at the time of perijove 17 (PJ17) is 0.565 (Durante et al., 2020), establishing a -4% deviation from the theoretical hydrostatic number $k_2^{(hs)} = 0.590$ (Wahl et al., 2020). The correction to the hydrostatic k_2 due to the rotational bulge is included in $k_2^{(hs)}$ and is of order $q = \Omega^2 R_J^3 / \mathcal{G} M_J \sim 0.1$, the ratio of centrifugal effects to gravity at the equator (Wahl et al., 2020); R_J is the equatorial radius, and M_J is Jupiter's mass. The satellite-independent 3σ uncertainty (confidence level $\approx 99.7\%$) in Juno's observation is 3% of $k_2^{(hs)}$ at perijove 17

(Durante et al., 2020), close to the mean of observed deviation. At the end of the prime mission, the satellite-independent 3σ uncertainty in Juno's observation is projected to decrease to 1% (William Folkner, personal communication, 2020 April 8). Following the optimistic assumption that the mean deviation remains the same at the end of the prime mission, $k_2^{(hs)}$ will require a non-hydrostatic correction from -5% to -3% to be reconciled with 3σ observations.

In our tidal models, we evaluate a dynamical correction to the hydrostatic k_2 as

$$\frac{k_2}{k_2^{(hs)}} = 1 + \Delta k_2 + O(1\%), \tag{2.1}$$

where Δk_2 is the fractional dynamical correction calculated for a spherical planet using perturbation theory and comes from the inertia terms in the equation of motion. The fractional dynamical correction is of order $\Delta k_2 \sim \omega^2/4\pi\mathcal{G}\bar{\rho} \sim 0.1$, where $\bar{\rho}$ is the mean density of the planet and ω is the forcing frequency related to the tide. The theoretical hydrostatic number $k_2^{(hs)}$ includes the effect of the oblateness of the planet, a realistic equation of state, and a density profile consistent with the zonal gravitational moments J_2 and J_4. From assuming that the number $k_2^{(hs)}$ is perfectly known, we aim to evaluate how the gravitational contribution of dynamical tides perturbs $k_2^{(hs)}$.

Instead of adding dynamical effects into the already complicated numerical model used to calculate $k_2^{(hs)}$, we use perturbation theory to isolate the dynamical effects in a much simpler interior model defined by an $n = 1$ polytropic equation of state. The $n = 1$ polytrope $p = K\rho^2$ closely follows the equation of state of a H-He mixture (Stevenson 2020) and is chosen for computational simplicity but is not crucial to the Δk_2 calculation. The density distribution in a non-rotating $n = 1$ polytrope is $\rho = \rho_c j_0(kr)$. The central density ρ_c is set to fit Jupiter's total mass; j_0 is the zero-order spherical Bessel function of second kind; $k^2 = 2\pi\mathcal{G}/K$ is a normalizing constant for the radius, where $K = 2.1 \cdot 10^{12}$ (cgs) for an H/He cosmic ratio (Hansen et al., 2012); $\mathcal{G}$ is the gravitational constant; r is the radial coordinate. Exploiting the compact equation of state and density profile of the $n = 1$ polytrope, we calculate the dynamical Love number by accounting for the dynamical terms in the equation of motion (Section 2.4). The fractional dynamical correction Δk_2 comes from comparing the hydrostatic and dynamical Love number in the polytrope; however, as the correction is expressed in fractional terms, Δk_2 calculated this way introduces dynamical effects into any hydrostatic model, to leading order approximation. The hydrostatic Love number in a spherical planet

following an $n = 1$ polytrope is obtained analytically (Fig. 2.1; Appendix A). For example, the degree-2 hydrostatic Love number of a spherical planet following an $n = 1$ polytrope is $k_2 = 15/\pi^2 - 1 \approx 0.520$. Stated explicitly, our approach assumes that the realistic elements included in the calculation of $k_2^{(hs)} = 0.590$ produce little effect on the dynamical tide and can be ignored for now.
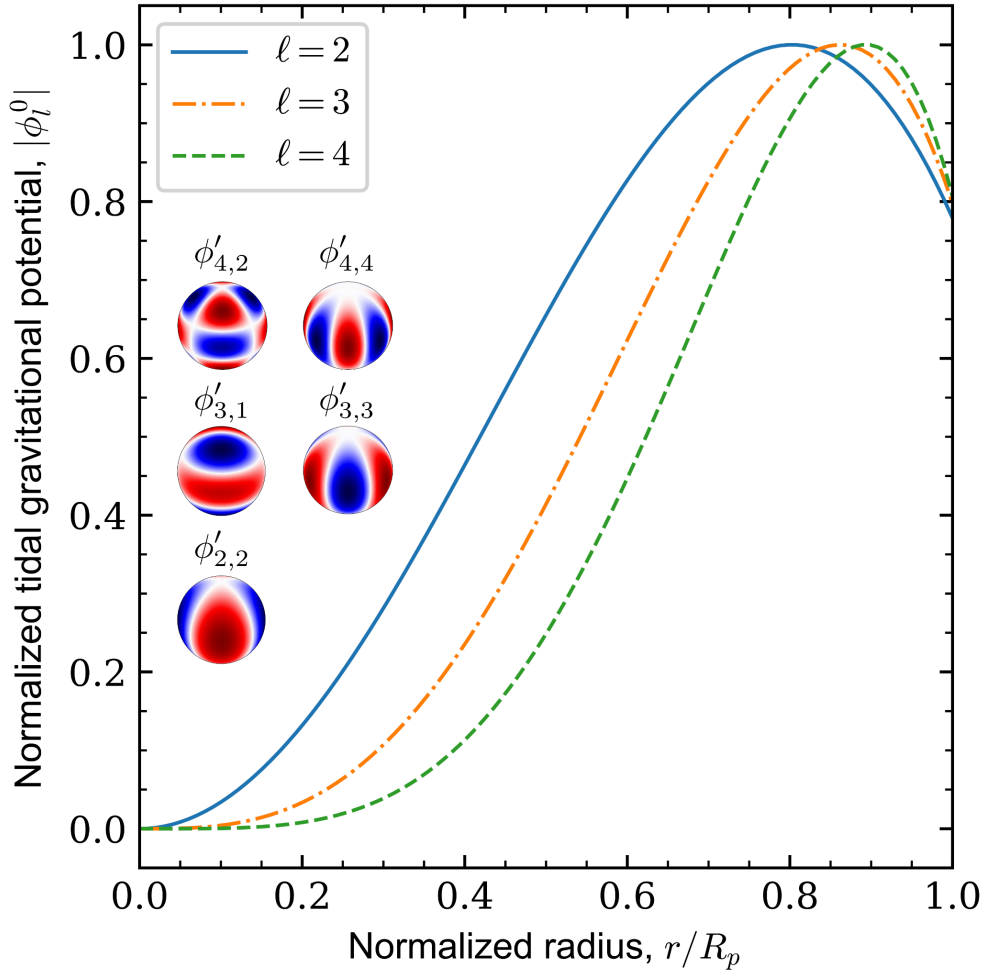
Figure 2.1: Angular patterns and radial functions describing the 3D structure of the gravitational field of tides. The radial functions are the normalized hydrostatic gravitational potential $|\phi^0|$ in an $n = 1$ polytrope (Equation (A.9)). The sign of the hydrostatic ℓ−tide is $(-1)^{(\ell+m)/2}$. The hydrostatic tide is zero for ℓ and m of different parity.

The uncertainty $\mathcal{O}(1\%)$ in equation (4.1) is an order-of-magnitude estimate of the neglected cross-term that accounts for the effect of the centrifugal effect on dynamical tides. Individually, the centrifugal and the dynamical effects are both of order

~10%. In linear perturbation theory, the cross-term is roughly the multiplication of the individual terms, resulting in ~1%. The uncertainty may be smaller as the dynamical correction involves terms that tend to cancel each other. This cancellation is expected to remain when an account is made of the oblateness of the planet, since (as our analysis shows below) it is the small difference between ω and 2Ω that matters, with or without oblateness.

The remainder of this manuscript deals with the calculation of the dynamical Love number.

Equations of tides in an adiabatic gas giant planet

To calculate the Love number k, we must compute the tidal gravitational potential ϕ' on Jupiter. The Love number k represents the ratio of ϕ' over the gravitational pull of the satellite ϕ^T evaluated at the outer boundary of the planet,

$$k_{\ell,m} = \left(\frac{\phi'_{\ell,m}}{\phi^T_{\ell,m}}\right)_{r=R_p}. \tag{2.2}$$

At a distance r from the center of a planet of radius R_p, the potential ϕ^T from a satellite orbiting in a circular orbit aligned with the equatorial plane of the planet is

$$\phi^T = \sum_{\ell=2}^{\ell} \sum_{m=-\ell}^{\ell} U_{\ell,m} \left(\frac{r}{R_p}\right)^{\ell} Y_\ell^m(\theta,\varphi)e^{i\omega t}, \tag{2.3}$$

where $U_{\ell,m}$ are a numerical constants and Y_ℓ^m are normalized spherical harmonics (Appendix A). The tidal frequency $\omega = |m(\Omega - \omega_s)|$ represents the frequency of a standing wave as observed from the perspective of an observer rotating with the planet at a spin rate Ω, where ω_s is the orbital frequency of the satellite and m is the order of the tide. We follow the convention where ω is always positive and retrograde tides are represented by a negative order m that flips the coordinate frame. The simplifications applied to the orbit are consistent to first order with the observed eccentricities $e < 0.01$ and inclinations $i < 0.5°$ of the Galilean satellites.

We calculate the tidal response of a rigidly rotating planet from a problem defined by the linearly perturbed momentum, continuity, and Poisson's equations, respectively,

$$-i\omega\mathbf{v} + 2\mathbf{\Omega} \times \mathbf{v} = -\frac{\nabla p'}{\rho} + \frac{\rho'}{\rho^2}\nabla p + \nabla\tilde{\phi}', \tag{2.4}$$

$$\nabla \cdot (\rho\mathbf{v}) = i\omega\rho', \tag{2.5}$$

$$\nabla^2\tilde{\phi}' = -4\pi\mathcal{G}\rho'. \tag{2.6}$$

The tidal response of the planet produces adiabatic perturbations to the gravitational potential ϕ', the density profile ρ', and pressure p'. The potential of the gravitational pull ϕ^T and the tidal gravitational potential ϕ' are combined into $\tilde{\phi}' = \phi^T + \phi'$ for analytical simplicity. Adiabatic perturbations in an adiabatic planet follow the thermodynamic statement (e.g., Wu (2005)),

$$\frac{p'}{p} = \Gamma_1 \frac{\rho'}{\rho} = c_s^2 \frac{\rho'}{p}, \tag{2.7}$$

where Γ_1 is the first adiabatic index (Aerts et al., 2010). Unprimed pressure and density represent the unperturbed state of the planet in hydrostatic equilibrium. We rewrite the momentum equation of an adiabatic planet as

$$-i\omega \mathbf{v} + 2\mathbf{\Omega} \times \mathbf{v} = \nabla \left(\tilde{\phi}' - \frac{p'}{\rho} \right) = \nabla \left(\tilde{\phi}' - c_s^2 \frac{\rho'}{\rho} \right) = \nabla \psi. \tag{2.8}$$

In equation (2.8), hydrostatic tides follow $\psi = 0$ (Appendix A).

The tidal flow becomes a function of the potential ψ after operating the divergence and curl on the momentum equation (Goodman and Lackner, 2009; Wu, 2005),

$$\mathbf{v} = -\frac{i\omega}{4\Omega^2 - \omega^2} \left(\nabla \psi + \frac{2}{i\omega} \mathbf{\Omega} \times \nabla \psi - \frac{4}{\omega^2} \mathbf{\Omega} (\mathbf{\Omega} \cdot \nabla \psi) \right). \tag{2.9}$$

After replacing the flow into the continuity equation, the governing equations of tides in an adiabatic planet reduce to

$$\nabla \cdot \left(\rho \left(\nabla \psi + \frac{2}{i\omega} \mathbf{\Omega} \times \nabla \psi - \frac{4}{\omega^2} \mathbf{\Omega} (\mathbf{\Omega} \cdot \nabla \psi) \right) \right) = \left(\frac{4\Omega^2 - \omega^2}{4\pi \mathcal{G}} \right) \nabla^2 \tilde{\phi}', \tag{2.10}$$

$$\psi = \frac{c_s^2}{4\pi \mathcal{G} \rho} \nabla^2 \tilde{\phi}' + \tilde{\phi}'. \tag{2.11}$$

Perturbation theory allows us to decouple the weakly coupled potentials ψ and $\tilde{\phi}'$ in equations (2.10) and (2.11). According to perturbation theory, the tidal gravitational potential splits into a static and dynamic part,

$$\phi' = \phi^0 + \phi^{dyn}, \tag{2.12}$$

where ϕ^0 corresponds to the gravitational potential of the hydrostatic tide after solving equation (2.11) with $\psi = 0$ (Fig. 2.1; Appendix A). By definition, the sound speed in an $n = 1$ polytrope follows $c_s^2 = 2K\rho$, which reduces the hydrostatic version of equation (2.11) to

$$\frac{\nabla^2 \phi^0}{k^2} + \phi^0 + \phi^T = 0. \tag{2.13}$$

As a good approximation, we ignore the contribution from dynamical tides to the potential ψ by setting $\nabla^2 \tilde{\phi}' \approx \nabla^2 \phi^0$ on the right-hand side in equation (2.10). According to equation (2.10), the potentials satisfy $\psi \sim \phi' \omega^2 / 4\pi \mathcal{G} \bar{\rho}$, which leads to $\phi' \gg \psi$ given a tidal frequency $\omega^2 \ll 4\pi \mathcal{G} \bar{\rho}$. By continuity, the approximation means that the tidal flow mostly advects the mass in the hydrostatic tidal bulge (i.e., $\rho' \approx \rho^0$ and equation (2.6)). The decoupled tidal equations simplify to

$$\nabla \cdot \left(j_0(kr) \left(\nabla \psi + \frac{2}{i\omega} \boldsymbol{\Omega} \times \nabla \psi - \frac{4}{\omega^2} \boldsymbol{\Omega} (\boldsymbol{\Omega} \cdot \nabla \psi) \right) \right) = \left(\frac{4\Omega^2 - \omega^2}{4\pi \mathcal{G} \rho_c} \right) \nabla^2 \phi^0, \quad (2.14)$$

$$\psi = \frac{\nabla^2 \phi^{dyn}}{k^2} + \phi^{dyn}. \quad (2.15)$$

We obtain the dynamical gravitational potential ϕ^{dyn} first solving ψ from equation (2.14) and then using the result to calculate ϕ^{dyn} from equation (2.15).

The boundary condition at the center of the planet imposes a finite solution for both potentials, allowing us to discard the divergent term characteristic of problems that include the Laplace operator. As required for a free planetary boundary, the condition at the outer boundary sets the Lagrangian perturbation of pressure equal to zero (e.g., Goodman and Lackner (2009)),

$$v_r = \mathbf{v} \cdot \hat{n} = -i\omega \frac{p'}{\partial_r p} = -i\omega \rho' \frac{c_s^2}{\rho g}, \quad (2.16)$$

or,

$$\hat{n} \cdot \nabla \psi + \frac{2}{i\omega} \hat{n} \cdot (\boldsymbol{\Omega} \times \nabla \psi) - \frac{4}{\omega^2} (\hat{n} \cdot \boldsymbol{\Omega})(\boldsymbol{\Omega} \cdot \nabla \psi) = - \left(\frac{4\Omega^2 - \omega^2}{4\pi \mathcal{G}} \right) \frac{c_s^2}{\rho g} \nabla^2 \tilde{\phi}'$$

$$= - \left(\frac{4\Omega^2 - \omega^2}{g} \right) (\psi - \tilde{\phi}'), \quad (2.17)$$

where v_r is the radial component of the tidal flow, $\hat{n}$ is a unitary vector normal to the outer boundary, and g is the gravitational acceleration at the outer boundary. The sound speed and density nearly vanish near the outer boundary of a compressible body, resulting in a finite radial flow (e.g., $v_r = -2K\omega \rho' / g$ in an $n = 1$ polytrope). The outer boundary condition (2.17) indicates $\psi / R_J \sim (\tilde{\phi}' - \psi) \omega^2 / g$. The Jupiter-Io system prescribes $1/R_J \gg \omega^2/g$, which leads to $\tilde{\phi}' \gg \psi$ and simplifies equation (2.17) into

$$\hat{n} \cdot \nabla \psi + \frac{2}{i\omega} \hat{n} \cdot (\boldsymbol{\Omega} \times \nabla \psi) - \frac{4}{\omega^2} (\hat{n} \cdot \boldsymbol{\Omega})(\boldsymbol{\Omega} \cdot \nabla \psi) = \left(\frac{4\Omega^2 - \omega^2}{g} \right) (\phi^0 + \phi^T). \quad (2.18)$$

Also at the outer boundary, the gravitational potential should be continuous in amplitude and gradient with a gravitational potential external to the planet that decays as $r^{-(l+1)}$.

In the following section, we solve the tidal equations for a uniform-density model and an $n = 1$ polytrope model with and without the Coriolis effect.

2.4 Dynamical tides in a gas giant planet

Following our simplified model of dynamical tides, we calculate Δk_2 in a coreless, chemically homogeneous, and adiabatic Jupiter-like model. The thermal state becomes almost adiabatic in a convecting fluid planet with homogeneous composition. From the point of view of tidal calculations, the deviation from adiabaticity is negligible in the interior because the superadiabaticity required to sustain convection is a tiny fraction of the adiabatic temperature gradient, despite the possible inhibitions arising from rotation and convection. A fluid parcel in an adiabatic interior that is adiabatically displaced by a tidal perturbation will find itself in a new state that is essentially unchanged in density and temperature from the unperturbed state at that pressure. This definition of neutral stability begins to break down near the photosphere, where the density is low and the radiative time constant is no longer huge for blobs with spatial dimension of order the scale height. However, that region represents only a tiny fraction of the planet and does not produce enough gravity to significantly alter the real part of the Love number k. We discuss hypothetical contributions to k from a core and depth-varying chemical composition in Section 4.

As a matter of simplifying the arguments presented in this section, we mostly concentrate on the Love number at $\ell = m = 2$, commonly known as k_2. Correspondingly, k_2 is forced by the degree-2 component in the gravitational pull,

$$\phi_2^T = \frac{3}{16} \frac{G m_s}{a^3} r^2 \sin^2 \theta e^{-i(\omega t + 2\varphi)}. \tag{2.19}$$

Dynamical effects scale with the satellite-dependent ω. We concentrate on the dynamical effects caused by Io, the Galilean satellite with the dominant gravitational pull on Jupiter.

A non-rotating gas giant

To an excellent approximation, dynamical tides in a non-rotating planet represent the forced response of the planet in the fundamental normal mode of oscillation (f-mode) (Vorontsov et al., 1984). Despite Cassini suggesting that higher-order normal mode

overtones (p-modes) dominate the gravitational field of Saturn's free-oscillating normal modes (Markham et al., 2020), the forced response of normal modes depends on the coupling of the gravitational pull and the mode radial eigenfunction. The forced response of p-modes contributes negligibly to the gravitational field of dynamical tides (Vorontsov et al., 1984) because of the bad coupling between the zero-node radial component of the gravitational pull and p-modes' eigenfunctions, the latter having one or more radial nodes. Conversely, the gravitational pull more efficiently excites f-modes, whose radial eigenfunctions roughly follow the radial scaling of the gravitational pull ($\propto r^\ell$).

The harmonic oscillator analogy

In the following, we use the forced harmonic oscillator as an analog model to tidally forced f-modes. In this model, the fractional dynamical correction to k_2 acquires a simple analytical form. The equation of motion of a mass M connected in harmonic motion to a spring of stiffness $\mathcal{K}$ and negligible dissipation is

$$- M\omega^2 u + \mathcal{K}u = F^T, \tag{2.20}$$

where ω is the forcing frequency and F^T is the tidal forcing. F-modes oscillate at frequencies ω_0 that are much higher than the forcing tidal frequency, meaning that tidal resonances with f-modes are highly unlikely. Assuming that the dynamical effects are small so that the tidal forcing is mostly balanced by static effects (i.e., $F^T \approx \mathcal{K}u_s$), the displacement of the mass is

$$u = u_s \left(\frac{\omega_0^2}{\omega_0^2 - \omega^2} \right). \tag{2.21}$$

The mass assumes the static equilibrium position u_s as the forcing frequency tends to zero. The displacement u is analogous to the Love number k; thus, the fractional dynamical correction becomes

$$\Delta k = \frac{u - u_s}{u_s} = \frac{\omega^2}{\omega_0^2 - \omega^2}. \tag{2.22}$$

The Coriolis-free $n = 1$ polytrope

To verify the analogy of the forced harmonic oscillator to tidally forced f-modes, we calculate the tidal response of a non-rotating $n = 1$ polytrope directly from the

governing equations of tides. When $\Omega = 0$, the governing equation (2.14) reduces to

$$j_0(kr)\nabla^2\psi - j_1(kr)\partial_r(\psi) = -\left(\frac{\omega^2}{4\pi G\rho_c}\right)\nabla^2\phi^0. \tag{2.23}$$

For the potential ψ at $\ell = m = 2$, the boundary condition at the outer boundary $r = R_p$ (Equation (2.17)) is

$$\frac{g}{\omega^2}\partial_r\psi_2 - \psi_2 = -5j_2(kR_p). \tag{2.24}$$

For the same degree and order, the continuity of the gravitational potential and its gradient at the outer boundary requires

$$\partial_r\phi_2^{dyn} = -\left(\frac{3\phi_2^{dyn} + 5}{R_p}\right). \tag{2.25}$$

At the center of the planet $r = r_0 \to 0$, we find the following scaling $\nabla^2\phi^0 \sim 0$, $j_1(kr_0) \sim 0$, and $j_0(kr_0) \sim$ constant. A finite potential ψ satisfying equation (2.23) is $\psi_2 \sim r^2$ near r_0, or,

$$\partial_r\psi_2 - \frac{2}{r_0}\psi_2 = 0. \tag{2.26}$$

Similarly, a finite gravitational potential of dynamical tides is $\phi_2^{dyn} \sim r^2$ at the center of the planet, satisfying

$$\partial_r\phi_2^{dyn} - \frac{2}{r_0}\phi_2^{dyn} = 0. \tag{2.27}$$

We compute the fractional dynamical correction to k_2 first projecting the tidal equations into spherical harmonics (Appendix B) and later solving for the relevant potentials using a Chebyshev pseudospectral numerical method (Appendix C). After projecting equations (2.23) and (2.15) into spherical harmonics, we obtain two decoupled equations for the radial parts of the potentials ψ and ϕ (Appendix B.1). After numerically solving the radial equations in Appendix B.1 using Io's gravitational pull $\omega_s \approx 42\mu$Hz), the fractional dynamical correction corresponds to $\Delta k_2 \approx 1.2\%$, in close agreement with the forced harmonic oscillator analogy applied to the oscillation frequency of the degree-2 f-mode $\omega_0 \approx 740\,\mu$Hz (Vorontsov et al., 1976). We observe a similar agreement between the harmonic oscillator and the Coriolis-free $n = 1$ polytrope at higher-degree spherical harmonics (Table 2.1). Our results agree with a previously reported fractional correction to the gravitational coefficient $C_{2,2} \propto k_2$ due to dynamical tides in a non-rotating Jupiter. (Vorontsov et al., 1984).

Table 2.1: Io-induced fractional dynamical correction Δk in a Coriolis-free Jupiter.

Type	Harmonic oscillator[1] (%)	$n = 1$ polytrope (%)
Δk_2	+15	+13
Δk_{42}	+5	+5
Δk_{31}	+2	+2
Δk_{33}	+19	+15
Δk_{44}	+25	+19

[1] See equation (F.2). The mode frequency without rotation comes from Vorontsov et al. (1976).

When Vorontsov et al. (1984) excluded Jupiter's spin, they were doing something that was mathematically sensible but physically peculiar. Tides occur much more frequently in Jupiter's rotating frame of reference, and the tidal flow is accordingly much larger than if one had Jupiter at rest, which implies a much larger dynamical effect. Consequently, Δk_2 increases by an order of magnitude after partially including Jupiter's rotation in the tidally forced response of f-modes. Without the Coriolis effect but including Jupiter's spin rate ($\Omega \approx 176\ \mu$Hz) in the calculation of Io's tidal frequency ($\omega \approx 270\ \mu$Hz), the fractional dynamical correction in an $n = 1$ polytrope corresponds to $\Delta k_2 \approx 13\%$, close to the $\Delta k_2 \approx 15\%$ from the forced harmonic oscillator analogy (Equation (F.2)). In general, for a non-rotating planet, the dynamical correction increases as the tidal frequency approaches the characteristic frequency of Jupiter's f-modes ($\sqrt{GM_J/R_J^3} \sim 600\ \mu$Hz).

The Coriolis effect in a rotating gas giant

The Galilean satellites produce dynamical tides for which the Coriolis effect plays an important role. Following relatively slow orbits ($\omega_s \ll \Omega$), the Galilean satellites produce tides on Jupiter with a tidal frequency $\omega \sim 2\Omega$. Consequently, the two inertial terms responsible for dynamical tides on the left-hand side of the equation of motion (Equation (F.1)) have similar amplitudes. Moreover, Juno observes k_2 to be less than the predicted number for a purely hydrostatic tide (Section 2.3) and yet our analysis above produces a positive Δk_2 when dynamical effects are included and the Coriolis effect is neglected (see equation (F.2)). We must accordingly motivate the change in sign when Coriolis is included.

In the following, we first calculate the gravitational effect of dynamical tides in a

uniform-density sphere to reveal the fundamental behavior of the tidal equations, avoiding most of the technical difficulties related to using an $n = 1$ polytrope. We later found that the more complicated case of an $n = 1$ polytrope introduces a minor quantitative difference but leads to the same general behavior.

A uniform-density sphere

First, we explain why Δk_2 changes sign because of the Coriolis effect in a specially simple model with uniform density. We calculate the fractional dynamical correction to k_2 in two steps: (1) we calculate the potential of the flow ψ in a uniform-density sphere, and (2) we use the ψ calculated this way to calculate the gravity potential ϕ'.

In a uniform-density sphere, the sound speed c_s is infinite, and Equation (2.10) reduces to the well-known Poincaré problem (Greenspan et al., 1968),

$$\nabla^2 \psi - \frac{4}{\omega^2}(\boldsymbol{\Omega} \cdot \nabla)^2 \psi = 0, \tag{2.28}$$

where the boundary condition at the outer boundary requires to satisfy equation (2.18).

Following the incompressibility of a uniform-density sphere, ψ_2 retains the symmetry and degree-2 angular structure from the gravitational pull in equation (2.19), thus acquiring exact solutions in the form

$$\psi_2 \propto (x - iy)^2. \tag{2.29}$$

The numerical factor in ψ_2 is set by the outer boundary condition (2.17), corresponding to (Goodman and Lackner, 2009)

$$\psi_2 = \frac{3\omega(2\Omega - \omega)}{8\pi G \bar{\rho}} \tilde{\phi}'_2 = \frac{R_p \omega(2\Omega - \omega)}{2g} \tilde{\phi}'_2. \tag{2.30}$$

In a constant-density sphere, tides act displacing the sphere's boundary within an infinitesimally thin shell. According to the momentum equation, the tidal gravitational potential relates to the potential ψ following

$$\tilde{\phi}' - \psi - \frac{p'}{\bar{\rho}} = 0. \tag{2.31}$$

The radial tidal displacement projected into spherical harmonics is

$$\xi = \sum_{\ell,m} \xi_{\ell,m}(r) Y_\ell^m(\theta, \varphi), \tag{2.32}$$

and the pressure perturbation follows

$$p' = -\xi \frac{\partial p}{\partial r} = \xi \bar{\rho} g. \tag{2.33}$$

The gravitational potential of a thin spherical density perturbation follows directly from the definition of the gravitational potential and integration throughout the volume,

$$\phi' = \sum_{\ell,m} \frac{4\pi G \bar{\rho}}{(2\ell + 1)} \frac{R_p^{\ell+2}}{r^{\ell+1}} \xi_{\ell,m} Y_\ell^m. \tag{2.34}$$

The degree-2 tidal gravitational potential corresponds to

$$\phi_2' = \frac{4\pi G \bar{\rho}}{5} \frac{R_p^4}{r^3} \xi_2 = \frac{3}{5} \left(\frac{R_p}{r} \right)^3 g \xi_2. \tag{2.35}$$

We once again use perturbation theory to split the hydrostatic and dynamic contributions to the tidal displacement (i.e., $\xi_2 = \xi^0 + \xi^{dyn}$). We first solve the well-known problem of the hydrostatic k_2 (i.e., $\psi = 0$) in a uniform-density sphere (Love, 1909). At the sphere's boundary (i.e., $r = R_p$), the hydrostatic gravitational potential follows $\phi^0 = 3g\xi^0/5$. From equation (2.31) evaluated at $r = R_p$, the potential of the gravitational pull becomes $\phi^T = 2g\xi^0/5$. Following the last two results, the Love number is $k_2 = 3/2$, as expected.

The dynamical contribution to the tidal displacement ξ^{dyn} produces the gravitational potential $\phi^{dyn} = 3g\xi^{dyn}/5$. After applying perturbation theory and canceling the hydrostatic terms in equation (2.31), the potential ψ_2 becomes $\psi_2 = -2g\xi^{dyn}/5$. Combined with equation (2.30), the last result for ψ_2 allows us to reach an expression for the fractional dynamical correction in a uniform-density sphere,

$$\Delta k_2 = \frac{\xi^{dyn}}{\xi^0} \approx - \left(\frac{5R_p}{4g} \right) \omega(2\Omega - \omega). \tag{2.36}$$

Two effects contribute to the fractional dynamical correction: a negative contribution from the Coriolis effect $\propto 2\Omega\omega/\pi G \bar{\rho}$ and a positive contribution from the dynamical amplification of f-modes $\propto \omega^2/\pi G \bar{\rho}$. The two contributions cancel each other at $2\Omega = \omega$, where the tide achieves hydrostatic equilibrium. Tides become hydrostatic not only when the planetary spin is phase-locked with the orbit of the satellite ($\Omega = \omega_s$), but also in planet-satellite systems where the central body is rotating at a rate many orders of magnitude faster than the orbit of the satellite (i.e., $\Omega \gg \omega_s$). As the frequency of the degree-2 f-mode approximately follows $\omega_0^2 \sim g/R_p$, Δk_2 in
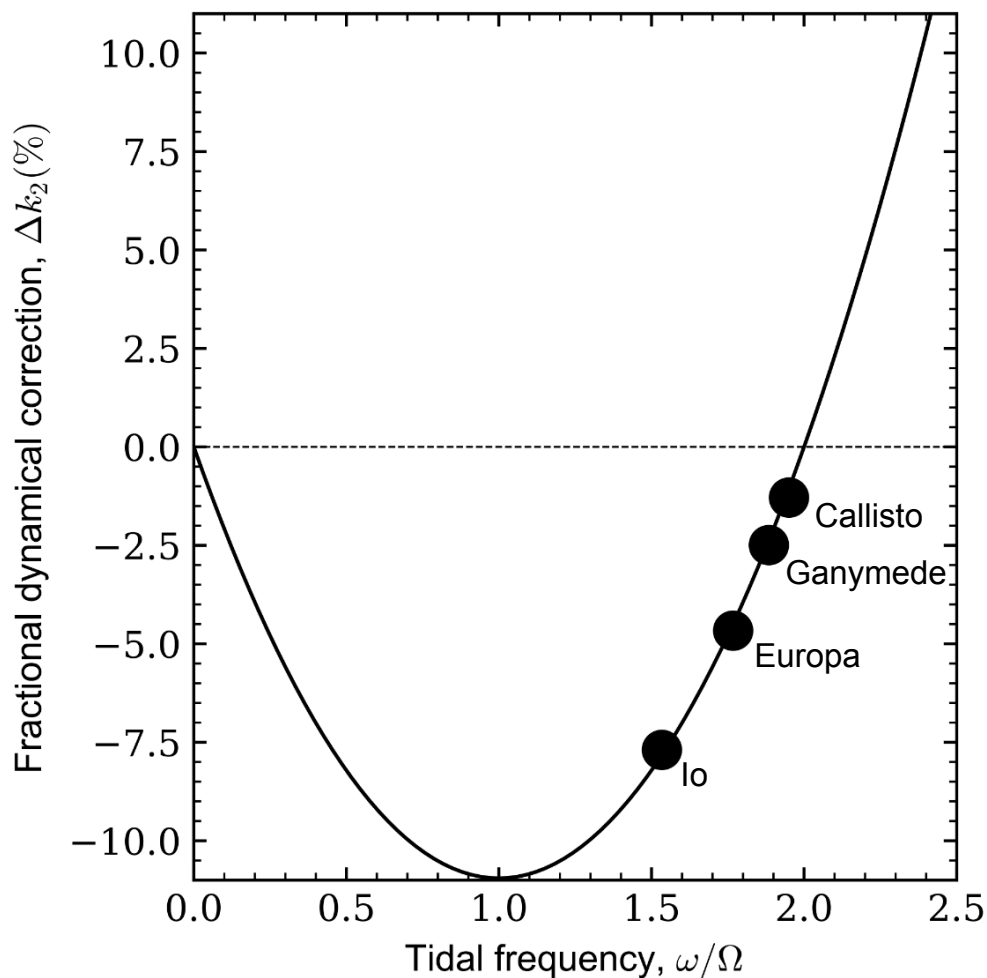
Figure 2.2: Fractional dynamical correction Δk_2 in a rotating uniform-density sphere including the Coriolis effect as a function of tidal frequency (see equation (2.36)).

equation (2.36) approximately becomes the positive fractional correction determined in Section 2.4 after setting $\Omega = 0$.

At the degree-2 Io-induced tidal frequency, the fractional dynamical correction corresponds to $\Delta k_2 \approx -7.8\%$. The other Galilean satellites lead to a smaller Δk_2 because their tidal frequency falls closer to hydrostatic equilibrium (Fig. 2.2). A negative Δk_2 works in the direction required by the non-hydrostatic component identified by Juno in Jupiter's gravity field (Section 2.3).

The direction of the flow provides an explanation for the negative sign of the fractional dynamical correction via the Coriolis acceleration. By definition, a uniform-density sphere has no density perturbations in its interior and thus produces

an interior tidal gravitational potential that satisfies $\phi' \propto r^\ell Y_\ell^m \propto \phi^T$. We adopt equation (2.30) as the degree-2 potential ψ and obtain analytical solutions for the Cartesian components of the resulting degree-2 tidal flow using equation (2.9),

$$\mathbf{v}_2 = -\frac{A\omega R_p}{g} \left(\hat{x}(ix + y) + \hat{y}(x - iy) \right), \tag{2.37}$$

where A is a constant depending on ξ (Appendix D). The degree-2 tidal flow purely exist in equatorial planes, showing no vertical component of motion (Fig. 2.3b).
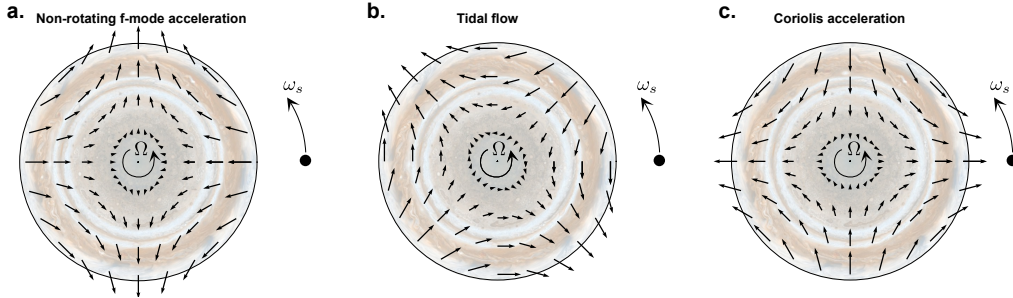
Figure 2.3: Degree-2 ($\ell = m = 2$) tidal perturbations on a uniform-density sphere forced by the gravitational pull of a companion satellite: (a) the non-rotating f-mode acceleration $-\omega^2\xi$, (b) tidal flow as shown in equation (2.37), and (c) Coriolis acceleration $\mathbf{\Omega} \times \mathbf{v}$ according to the right-hand rule.

The Coriolis acceleration plays a major role in setting the sign of the fractional dynamical correction for the Galilean satellites. Without Coriolis, the acceleration of non-rotating f-modes sustains a positive dynamical tidal displacement that follows $\xi^{dyn} \approx 5R_p\omega^2\xi^0/4g$. A $\xi^{dyn} > 0$ increases the tidal gravitational field, which leads to a positive Δk_2. Conversely, as shown in equation (2.36), the fractional dynamical correction flips sign when Coriolis promotes $\xi^{dyn} < 0$. A Coriolis term enters the momentum equation, introducing an acceleration that competes with the acceleration of non-rotating f-modes, ultimately impacting ξ^{dyn}. According to the right-hand rule, the Coriolis acceleration (i.e., $\mathbf{\Omega}\times\mathbf{v}$, Fig. 2.3c) opposes the direction of the acceleration of non-rotating f-modes (i.e., $-\omega^2\xi$, Fig. 2.3a). The resulting gravitational field is smaller than the hydrostatic field if $\omega < 2\Omega$, where the Coriolis acceleration beats the acceleration of non-rotating f-modes.

The $n = 1$ polytrope

In the following, we consider the more relevant case of a compressible planet that follows an $n = 1$ polytropic equation of state (Equation (2.14)). In contrast to

the localized tidal perturbation of a uniform-density sphere, a compressible body yields a tidally induced density anomaly that arises from advection of the isodensity surfaces within the body. The resulting tidal gravitational potential is different in each case owing to differences in the tidally perturbed density distribution obtained in a uniform-density sphere and a compressible body.

Despite the aforementioned difference between models, the tidal flow remains similar so that dynamical tides motivate a negative correction to k_2 in each case. In an $n = 1$ polytrope, the continuity equation (2.5) tells us that the degree-2 radial component of the flow takes the form $v_r \propto j_2(kr)/j_1(kr)$ when the flow has small divergence, as it does. Remarkably, the dominant contribution to the Taylor series expansion of v_r is linear in r, even out to a large fraction of the planetary radius. In a uniform-density sphere, the potential ψ is $\psi_2 \propto r^2$, which leads to a tidal flow that follows $v_2 \propto \nabla\psi_2$; therefore, v_r is also linear in r in this model. As shown, the dominant contribution to v_r scales with radius as $\propto r$, both in an $n = 1$ polytrope and in a uniform-density sphere. In an $n = 1$ polytrope, the dominant contribution to v_r is curl- and divergence-free and provides the $\psi_2 \propto r^2$ part of the solution to the potential ψ (Fig. 2.4a). Since the $n = 1$ polytrope also contains terms where ψ is of higher order in r, it produces a flow with non-zero curl and nonzero divergence, causing ψ_2 to depart from $\psi_2 \propto r^2$. Because high-order terms in r are smaller than the dominant term, dynamical effects on k_2 in a uniform-density sphere are qualitatively similar to those in an $n = 1$ polytrope.

We compute the fractional dynamical correction to k_2 in a rotating polytrope following the same strategy used in Section 2.4. In opposition to the Coriolis-free polytrope, solving equation (2.14) is technically challenging due to the ℓ−coupling of the potential $\psi_{\ell,m}$ (e.g., mode mixing) promoted by the Coriolis effect. Mode mixing is also found in hydrostatic tides over a planet distorted by the effect of the centrifugal force (Wahl et al., 2017a). The result of projecting equation (2.14) into spherical harmonics is an infinite ℓ−coupled set of ordinary differential equations for $\psi_{\ell,m}$ (Appendix B.2), similarly observed in the problem of dissipative dynamical tides (Ogilvie and Lin, 2004a). The Coriolis-promoted ℓ−coupling comes from the sine and cosine in the spin rate of the planet ($\mathbf{\Omega}/\Omega = \hat{r}\cos\theta - \hat{\theta}\sin\theta$), which changes the degree of the spherical harmonics related to ψ. As a consequence, a given spherical harmonic from ϕ^0 on the right-hand side of Equation (2.14) forces multiple spherical harmonics of the potential ψ with different ℓ.

Projected into spherical coordinates, the boundary condition (2.17) at $r = R_p$

corresponds to:

$$\partial_r \psi - \frac{2\Omega}{i\omega R_p}\partial_\varphi \psi - \frac{4\Omega^2}{\omega^2}\left(\cos^2\theta\partial_r\psi - \sin\theta\cos\theta\frac{\partial_\theta\psi}{R_p}\right) = \left(\frac{4\Omega^2 - \omega^2}{g}\right)(\phi^0 + \phi^T).$$

(2.38)

The outer boundary condition is also $\ell-$coupled after projected into spherical harmonics (Appendix B.2).
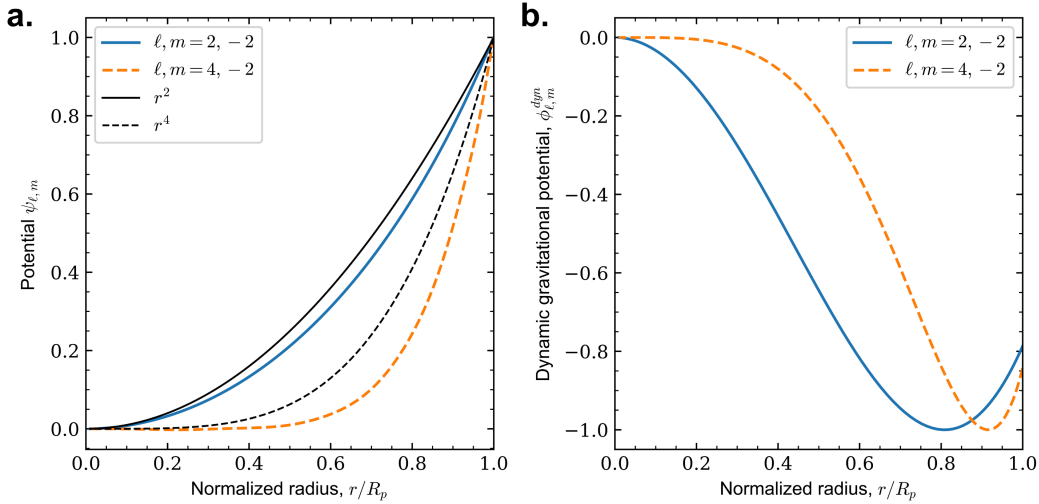
Figure 2.4: Radial functions in an $n = 1$ polytrope (thick blue and orange curves) of the (a) potential ψ and the (b) dynamical gravitational potential ϕ^{dyn}. The thinner black curves in panel (a) represent the radial scaling of the potential ψ in a uniform-density sphere.

At the center of the planet $r = r_0 \to 0$, we find the following scaling: $\nabla^2\phi^0 \sim 0$ and $j_0(kr_0) \sim$ constant. As a result, the tidal equation (2.14) becomes the previously solved problem of the potential ψ in a uniform-density sphere (2.28) near the center. Required to be finite near the center and to satisfy equation (2.28), the radial part of the potential ψ follows $\psi_{\ell,m} \sim r^\ell$. The boundary condition for $\psi_{\ell,m}$ near the center corresponds to

$$\partial_r \psi_{\ell,m} - \frac{\ell}{r_0}\psi_{\ell,m} = 0.$$

(2.39)

The equation for the gravitational potential of dynamical tides ϕ^{dyn} remains unchanged compared to the Coriolis-free polytrope (Appendix B.1). The outer and inner boundary conditions for the gravitational potential generalize in degree as

$$\partial_r \phi^{dyn}_{\ell,m} = -\left(\frac{(\ell+1)\phi^{dyn}_{\ell,m} + (2\ell+1)U_{\ell,m}}{R_p}\right),$$

(2.40)

$$\partial_r \phi_{\ell,m}^{dyn} - \frac{\ell}{r_0} \phi_{\ell,m}^{dyn} = 0. \tag{2.41}$$

By projecting $\psi_{\ell,m}$ and $\phi_{\ell,m}$ into a series of N Chebyshev polynomials oriented in the radial component (Appendix C), we numerically solve (B.14) and (B.4) truncating the infinite series of ℓ−coupled equations at an arbitrary $\ell = L_{max}$. We choose a truncation limit $L_{max} = 50$ and the number of Chebyshev polynomials $N_{max} = 100$ based on numerical evidence of convergence for k_2 and k_{42}.

Table 2.2: Jupiter Love numbers.

Type	Hydrostatic[1]	Juno PJ17 3σ[2]	3σ fractional difference[3]	Δk (rotating)[4] (%)			
	Number	Number	(%)	Io	Eu	Ga	Ca
k_2	0.590	0.565 ± 0.018	-7/-1	**-4**	-2	-1	-1
k_{42}	1.743	1.289 ± 0.189	-37/-15	**+7**	+8	+10	+12
k_{31}	0.190	0.248 ± 0.046	+6/+55	**+1**	+3	+4	+5
k_{33}	0.239	0.340 ± 0.116	-6/+91	**+2**	+5	+7	+8
k_{44}	0.135	0.546 ± 0.406	+4/+605	**+7**	+11	+13	+15

[1] The hydrostatic number is from Wahl et al. (2020).
[2] The Juno PJ17 3σ number is the satellite-independent number from Durante et al. (2020).
[3] The 3σ fractional difference represents the minimal/maximal 3σ non-hydrostratic fractional correction required to explain the Juno observations.
[4] The fractional dynamical correction is valid for an $n = 1$ polytrope forced by the gravitational pull of the Galilean satellites (Eu = Europa, Ga = Ganymede, Ca = Callisto).

We obtain $\Delta k_2 = -4.0\%$ at the degree-2 Io-induced tidal frequency (Table 3.1), which is of slightly lower amplitude than the estimate in a uniform-density sphere and in agreement with the k_2 non-hydrostatic component observed by Juno at PJ17. However different models, both the uniform-density sphere and the polytrope produce fractional dynamical corrections that fall within the order-of-magnitude estimate $\Delta k_2 \sim \omega^2/4\pi \mathcal{G}\rho \sim 0.1$. As argued before, the dominant contribution to the potential ψ follows the radial scaling $\psi_\ell \propto r^\ell$ (Fig. 2.4a). Ignoring the sign, the radial scaling of the dynamical gravitational potential ϕ^{dyn} (Fig. 2.4b) closely follows the shape of the hydrostatic gravitational potential (Fig. 2.1).

Due to the essentially circular and equatorial geometry of the Galilean orbits, the spherical harmonic $\ell = m = 2$ dominates Jupiter's tidal gravitational field. Consequently, we concentrate in comparing k_2 Juno observation to our model prediction. Of significantly higher uncertainty, the mid-mission Juno report of Love numbers

at PJ17 includes other spherical harmonics in addition to k_2 (Table 3.1). Our polytropic model predicts an Io-induced tidal gravitational field in a 3σ agreement with most Love numbers observed at PJ17, save for k_{42} and k_{31}.
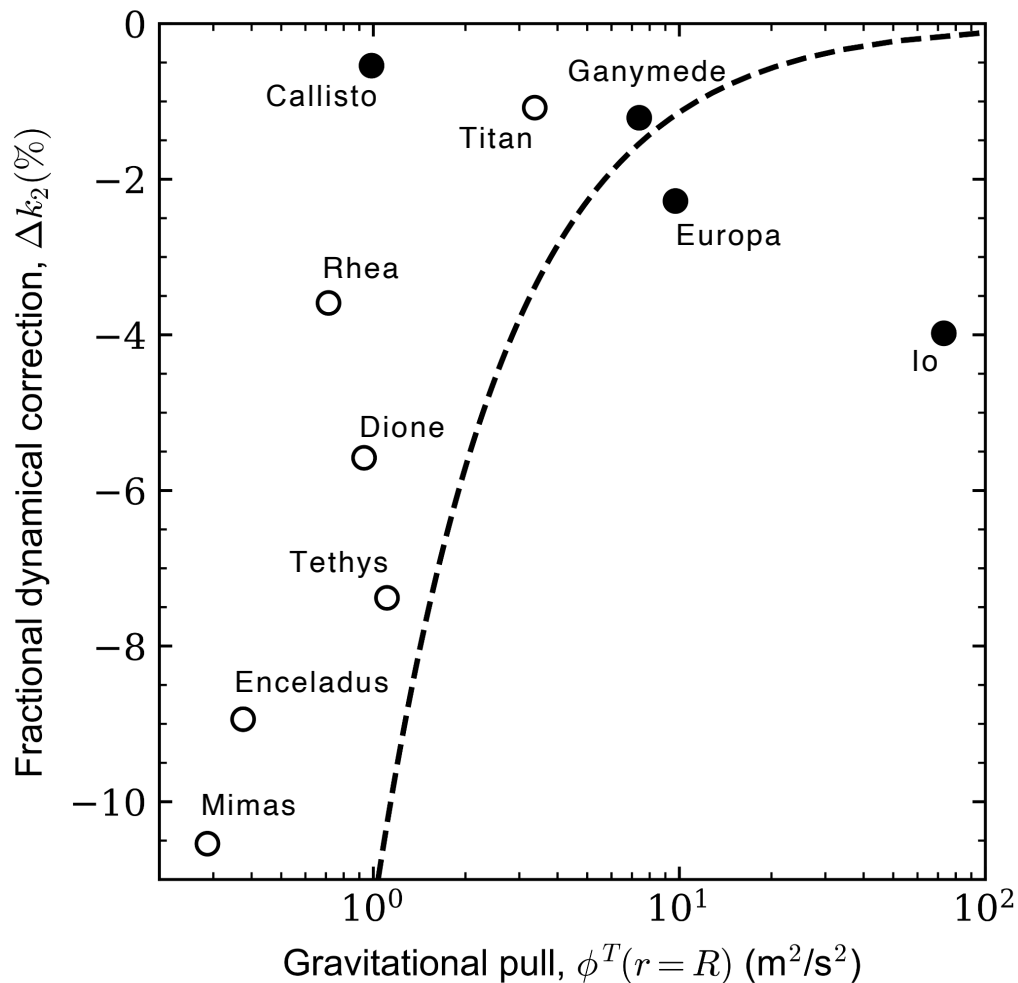
Figure 2.5: Conditions for the detection of dynamical tides evaluated for the Galilean satellites (black) and inner Saturn satellites (white). Satellites to the right of the dashed line have favorable conditions for a detection of dynamical tides assuming an uncertainty roughly similar to that of Io's k_2 on Jupiter at the end of Juno's extended mission. The fractional dynamical correction Δk_2 is for an $n = 1$ polytrope.

Detection of dynamical tides in systems other than Jupiter-Io

A detection of dynamical tides via direct measurement of the gravitational field will be challenging in bodies other than Jupiter (Fig. 2.5). The 1σ uncertainty in the gravitational field of degree-2 Io tides is projected to be $\sigma_J \sim 6 \cdot 10^{-2}$ m^2/s^2 at the end

of the proposed Juno extended mission (William Folkner, personal communication, 2020 April 8). The uncertainty in the measured tidal gravity field depends on the number and design of spacecraft orbits, the uncertainty in ephemerides, and instrumental capabilities. Assuming the uncertainty σ_J, we roughly estimate the gravitational pull required to produce a detectable dynamical component in the gravity field using

$$\phi^T(r = R) \gtrsim \frac{\sigma_J}{k_2|\Delta k_2|}. \tag{2.42}$$

Our calculation indicates that detecting dynamical tides in Saturn will require a mission with a more precise determination of the gravity field than that obtained by Juno (Fig. 2.5). A 1σ detection of Europa-induced dynamical tides seems plausible at the end of Juno's extended mission, assuming that the factors determining the uncertainty in the gravity field remain similar to those of Io. We calculate a model prediction for the satellite-dependent Jupiter Love number for all of the Galilean satellites (Table 3.1). We obtain $k_2 = 0.578$ in the case of Europa, a prediction testable by the recently approved Juno extended mission.

2.5 Discussion

Future updates to Juno Love number observations

The discrepancy between our predicted k_{42}, k_{31}, and the Juno PJ17 observations may allude to several reasons: (1) a suggestion to revise the hydrostatic $\ell-$coupled $k_{\ell,m}$ in Wahl et al. (2020), (2) a failure of perturbation theory in our model when accounting for the $\ell-$coupled $k_{\ell,m}$, (3) other physical reasons, for example, tidal resonance with normal modes or the neglected correction from a dilute core. We strongly suggest a thorough analysis of these possibilities in future investigations. Ultimately, the perijove passes required to complete the scheduled Juno mission may change the still highly uncertain numbers reported in Table 3.1. A recent revision to Juno observations at PJ29 (Daniele Durante, personal communication, 2020 November 18) suggests an agreement of our k_{31} prediction with the revised satellite-independent $k_{31} = 0.234 \pm 0.016 \,(1\sigma)$. The PJ29-revised $k_{42} = 1.5 \pm 0.095$ (1σ) remains in disagreement with our k_{42} prediction, but the difference is much narrower than that attained at PJ17. A disagreement between our predicted $k_{\ell,m}$ and high-degree Juno observations does not impair the much more relevant agreement observed for k_2. Compared to the amplitude of the tidal gravitational potential related to k_2, the tidal gravitational potential related to k_{42} represents an order-of-magnitude smaller contribution to the tidal gravitational field due to the factor $R_p/a \sim 1/6$ in $\phi^T_{\ell,m}$. In addition, whereas the predicted k_2 simply depends on the

contribution from the Coriolis effect and the dynamical response of f-modes, the more complicated predicted k_{42} additionally depends on the numerical solution of the $\ell-$coupled system of equations described in Section B.2.

Ignoring for the moment other possibilities related to the k_{42} discrepancy, resonant tides have been previously invoked as a potential candidate to explain the current structure of the Laplace resonance in Saturn (Fuller et al., 2016; Lainey et al., 2020). As planets in the solar system rotate far from breakup, there is no overlap between the frequencies of tides and f-modes in adiabatic, non-rotating planets. However, compositional gradients (g–modes) and rotation (inertial modes) introduce additional normal modes whose frequencies can become close to the tidal frequency, either by chance or by planetary evolution. These hypothetically resonant tides could produce high dissipation rates and thus a detectable imaginary part in the Love number that would consequently induce a significant change in the real part of the Love number. Equivalently, the high dissipation rate from an hypothetically resonant tide would cause a phase between the gravitational pull and the degree-2 tidal bulge. However, the degree-2 tidal dissipation in Jupiter due to Io tides is modest (Lainey et al., 2009). This argument does not necessarily apply for higher-degree tides ($\ell > 2$) that have much smaller amplitudes and therefore whose phase shifts would be much harder to detect.

We compare our Io-induced fractional dynamical corrections to the Juno PJ17 satellite-independent observations. We justify the use of the satellite-independent k_2 uncertainty because our results indicate small variations in the Love number due to dynamical effects (Table 3.1), assuming the absence of degree-2 tidal resonances. In the hypothetical of an $\ell = 4$, $m = 2$ tidal resonance, the Love number k_{42} would vary significantly among satellites. In such a case, we would be required to use a satellite-dependent uncertainty (Durante et al., 2020), in which no a priori information is used at the time of inferring the Love number. So far, we neither confirm nor deny resonant tides that may be having an impact on k_{42} or k_{31}. An improved version of the satellite-independent k_2 uncertainty could be obtained a priori assuming that the Love number increases ~4% outward when comparing the inner to the outer satellites. A stronger conclusion on the possibility of tidal resonances observed in Juno data requires additional progress in the mission to reduce the uncertainty on k_{42} and k_{31}, plus a thorough analysis of resonances with Jupiter interior models that include a compositional gradient.

A tighter constraint on the satellite-dependent k_2 from satellites other than Io will

test the prediction of our model of satellite-dependent dynamical tides. Despite the relatively large fractional dynamical correction obtained for the inner Saturn satellites (e.g., Mimas or Enceladus), their small mass leads to an overall small tidal disturbance that is difficult to detect in the gravity field. From all Jupiter and Saturn satellites, only Europa elevates a short-term prospect of obtaining a new detection of dynamical tides via Juno's extended mission (Fig. 2.5). A detection of dynamical tides due to other satellites will require an uncertainty on k_2 that is significantly lower than that produced by Juno.

Other potential contributions to k_2
Free-oscillating normal modes

Free oscillations of normal modes cannot explain the bulk of the non-hydrostatic Juno detection discussed here. The small gravitational field of tides becomes resolvable by Juno in part because the phase of the signal is well known. The unknown phase of non-resonant free oscillations departs from the phase of the satellite used in determining k_2. Even if freely oscillating normal modes were detected in Jupiter as they were in Saturn (Iess et al, 2019), the anticipated high frequency of their gravity field would render them irrelevant to the tidal problem. In order for free oscillations to play a role in the observed gravity, they require avoiding a rapid decay after becoming excited (i.e., a very high Q). It is not known whether free oscillations persist over multiple Juno perijove passes.

Jupiter's rheology

A central viscoelastic region in Jupiter's interior could potentially reduce k_2 below the hydrostatic number; however, evidence suggests that such a possibility is unlikely. Viscoelastic deformation of a body produces a k_2 between the purely elastic and the hydrostatic numbers, a model that helps to explain Titan's observed k_2 (Iess et al., 2012). Assuming that a traditional core in Jupiter exists, the core radius should remain small (i.e., $\sim 0.15 R_J$) to satisfy the constraint on the total abundance of heavy elements and the supersolar enrichment of the envelope (Wahl et al., 2020). At this core radius, the tidal deformation of the core does not contribute to $\text{Re}(k_2)$ (Storch and Lai, 2014). Whether rigid, elastic, or viscoelastic, a small traditional core produces a small effect on $\text{Re}(k_2)$ due to the added heavy elements, already included in the hydrostatic number (Wahl et al., 2020). Beyond the possibility of a viscoelastic traditional core, the hydrogen-rich envelope most likely behaves as

an inviscid fluid. The kinematic viscosity of the fluid external to the core needs to reach $v \sim 10^{11}$ m^2/s in order for its viscosity to become relevant at tidal timescales (i.e., $\omega \sim v/R_J^2$). Such kinematic viscosity exceeds by ~17 orders of magnitude the realistic estimates of the hydrogen-dominated fluid viscosity (Stevenson and Salpeter, 1977). A similar argument applies to a dilute core, which most likely consists of a mixture dominated by hydrogen.

The dynamical contribution of a traditional core

A traditional core blocks the tidal flow from extending to the center of the planet by forcing a zero-flow boundary condition at the core radius. As shown earlier, the radial tidal flow sets the amplitude of the tidal gravitational potential and roughly scales with distance from the center following $v_r \propto r$ in an $n = 1$ polytrope. Consequently, the tidal flow is nearly zero in the area where a traditional core would exist, minimizing a potential effect of the traditional core on the fractional dynamical correction. A thorough quantification of Δk_2 in a model with a traditional core that blocks the flow requires further investigation. We expect an effect going from negligible to small (i.e., less than +1% applied to the current estimate in Table 3.1) given the limits to traditional core size imposed by the constrained total abundance of heavy elements.

A dilute core

A dilute core may promote an additional departure of the tidal response from the hydrostatic tide to that caused by dynamical tides. The hydrostatic tide in k_2 provides the same information about the planet as J_2 (Hubbard, 1984). In the presence of a dilute core, the gravity produced by tides fundamentally differs from the $J_{2\ell}$ coefficients due to the different timescales associated with tidal perturbations and the evolution of the rotation rate. Tidal timescales are short compared to the timescale required for the tidal perturbation to equilibrate with the environment by either heat transport or compositional evolution. By contrast, the timescale at which the rotation rate evolves is so long that the planet adjusts to any perturbation caused by the centrifugal effect. Tidal displacements remain roughly adiabatic, whereas displacements induced by changes in the rotation rate reach thermodynamic equilibrium. A fluid parcel in the proximity of the dilute core responds differently depending on the timescale of the perturbation; only an adiabatic perturbation leads to changes in the buoyancy of the fluid parcel, causing a wave-like oscillation known

as static stability. Consequently, the dilute core produces a signature in the tidal response of the planet not registered by J_2. We address the tidal effects of a dilute core in a subsequent investigation.

2.6 Conclusions

Our tidal models suggest that the gravity field observed by Juno captured the dynamical tidal response of Jupiter to the gravitational pull of the Galilean satellites. We show that two effects contribute to the dynamical gravity field of tides in Jupiter: the dynamical response of f-modes and the Coriolis acceleration. When the Coriolis effect is ignored, tides closely follow the dynamical response of f-modes modeled as a forced harmonic oscillator. In ignoring the Coriolis effect, dynamical amplification in a harmonic oscillator accounts for the dynamical response of f-modes in the planet's interior, forced by the gravitational pull of the companion satellites. As the tidal frequency is lower than the f-mode oscillation frequency, the dynamical response of f-modes amplifies the gravity field of the hydrostatic tide. Motivated by Jupiter's fast rotation, we show that the Coriolis effect leads to a significant additional contribution to the dynamical tide. When the Coriolis effect is included in our tidal models, we show that the Coriolis acceleration produces a competing effect of opposite sign compared to the dynamical response of f-modes. When both dynamical effects are considered together, they reduce the Love number k_2 below the hydrostatic number if $\omega < 2\Omega$ and amplify it otherwise. Following our theoretical prediction, dynamical effects lead to a negative correction to Jupiter's hydrostatic Love number k_2 in the case of the Galilean satellites, for which the degree-2 tidal frequency is $\omega < 2\Omega$. The fractional dynamical correction for the Jupiter-Io system is $\Delta k_2 = -4\%$. Our analysis provides an explanation for the recently observed non-hydrostatic component in the gravity field of Jupiter tides obtained by the Juno mission.

In conclusion, our analysis proposes that the Juno non-hydrostatic detection is the first unambiguous measurement of the gravitational effects of dynamical tides in a gas giant. Our conclusion depends on the assumption that the degree-2 tidal frequency of the Galilean satellites is far from resonance with Jupiter's normal modes. In a subsequent investigation, we will utilize the results reported here to infer the extension and static stability of Jupiter's dilute core from k_2. The uncertainty expected in the observed k_2 at the end of the mission exceeds the uncertainty achieved by our model, suggesting that a more detailed tidal model will be required in the future to fully exploit the information contained in the data

provided by Juno.

Chapter 3

THE LOST MEANING OF JUPITER'S HIGH–DEGREE LOVE NUMBERS

"So baby, tell me where your love lies"

— Khalid & Normani, *Love Lies*

3.1 Abstract

NASA's Juno mission recently reported Jupiter's high–degree (degree ℓ, azimuthal order $m = 4, 2$) Love number $k_{42} = 1.289 \pm 0.063$ (1σ), an order of magnitude above the hydrostatic k_{42} obtained in a nonrotating Jupiter model. After numerically modeling rotation, the hydrostatic $k_{42} = 1.743 \pm 0.002$ is still 7σ away from the observation, raising doubts about our understanding of Jupiter's tidal response. Here, we use first–order perturbation theory to explain the hydrostatic k_{42} result analytically. We use a simple Jupiter equation of state ($n = 1$ polytrope) to obtain the fractional change in k_{42} when comparing a rotating model with a nonrotating model. Our analytical result shows that the hydrostatic k_{42} is dominated by the tidal response at $\ell = m = 2$ coupled into the spherical harmonic $\ell, m = 4, 2$ by the planet's oblate figure. The $\ell = 4$ normalization in k_{42} introduces an orbital factor $(a/s)^2$ into k_{42}, where a is the satellite semimajor axis and s is Jupiter's average radius. As a result, different Galilean satellites produce a different k_{42}. We conclude that high–degree tesseral Love numbers ($\ell > m$, $m \geq 2$) are dominated by lower–degree Love numbers and thus provide little additional information about interior structure, at least when they are primarily hydrostatic. Our results entail important implications for a future interpretation of the currently observed Juno k_{42}. After including the coupling from the well–understood $\ell = 2$ dynamical tides ($\Delta k_2 \approx -4\%$), Jupiter's hydrostatic k_{42} requires an unknown dynamical effect to produce a fractional correction $\Delta k_{42} \approx -11\%$ in order to fit Juno's observation within 3σ. Future work is required to explain the required Δk_{42}.

3.2 Introduction

NASA's Juno mission recently registered Jupiter's tidal response in a set of Love numbers, observing $k_{42} = 1.289 \pm 0.063$ (1σ) at the mid–mission perijove 17 (Durante et al., 2020). The observation requires imposing the same Love number for all Galilean satellites as an a priori constraint, resulting in a Juno k_{42} that represents the dominant tidal influence of Io (Durante et al., 2020). Ignoring the effect of rotation on tides, the modeled hydrostatic tidal response is $k_{42} = 0.1279$ in a Jupiter model with a density profile that fits the radius and zonal gravity up to J_4 (Wahl et al., 2020). In the same Jupiter model, numerical modeling indicates that rotation increases k_{42} by an order of magnitude to $k_{42} = 1.743 \pm 0.002$ in the case of Io's tidal forcing (Wahl et al., 2020), which is 7σ above the Juno k_{42}. The purpose of this paper is to illuminate on the rotational effect that leads to an order of magnitude enhancement in k_{42}, which is key to a correct interpretation of Juno's k_{42}.

Love numbers traditionally represent an interior property of the planet. A property of the planet must be independent of forcing; for example, the adiabatic sound speed. The Love number k_{42} corresponds to the tidal gravitational potential of Jupiter normalized by the tidal forcing produced by the satellite, both in the $\ell, m = 4, 2$ term of the spherical harmonics projection. The oblate figure of a rotating planet distorts the traditional meaning attributed to Love numbers by introducing spherical harmonic coupling; that is, the tidal forcing at given ℓ produces a tidal response in multiple spherical harmonics. In particular, Jupiter's Love number k_{42} contains a small contribution from the tidal response to the $\ell, m = 4, 2$ tidal forcing, plus a dominant contribution from the coupled tidal response to the $\ell = m = 2$ tidal forcing. For the sake of brevity, we partially omit further references to the order m, which should always be considered $m = 2$ throughout this paper.

The coupled tidal response promoted by the oblate figure of Jupiter enhances Jupiter's hydrostatic Love number k_{42} by an order of magnitude when compared to a hypothetical nonrotating Jupiter (Wahl et al., 2020). To order of magnitude, we can estimate $k_{42} \sim q k_2 (a/R)^2$, where a is the semimajor axis of the satellite, R is the planetary radius, k_2 is the $l = m = 2$ Love number, and q is the adimentional rotational parameter,

$$q = \frac{\Omega^2 s^3}{\mathcal{G}M},$$

(3.1)

where M is the mass of the planet, Ω is the planet's rotational frequency, s is the average planetary radius, and $\mathcal{G}$ is the gravitational constant. In the case of

Jupiter-Io, we obtain $q \approx 0.09$ and $k_{42} \sim 1.9$. The coupled tidal response to the $\ell = 2$ tidal forcing that contributes to k_{42} is of order $\sim q k_2$. The factor $(a/R)^2$ describes how much smaller the tidal forcing is at $\ell = 4$ when compared to $\ell = 2$. As numerically shown by Wahl et al. (2020), the resulting hydrostatic Love number k_{42} varies greatly among the Galilean satellites according to the semimajor axis of each orbit, a result that contradicts the traditional concept of the hydrostatic Love number defined as a property of the planet.

Here, we use first–order perturbation theory to analytically explain the correction to the hydrostatic Love number introduced by rotation, a result only known so far via implementation of numerical strategies (Wahl et al., 2017a). As a response to rotation, the oblate figure of the planet promotes mixing in the tidal response at different zonal degree ℓ, causing a $\sim +10\%$ correction to k_2 observed both in Saturn (Lainey et al., 2017; Wahl et al., 2017a) and Jupiter (Durante et al., 2020; Idini and Stevenson, 2021; Wahl et al., 2020), and an order of magnitude increment in k_{42} that is key to correctly interpreting Juno's k_{42} observation.

The remainder of this paper is organized as follows. In Section 2, we derive the general solution for the hydrostatic tidal response in the interior of a gas giant planet mostly made of H-He. In Section 3, we use first–order perturbation theory to obtain the hydrostatic Love numbers while including the oblate figure of the planet introduced by rotation. In Section 4, we use our theoretical results from Section 3 to calculate Jupiter's hydrostatic k_{42}. In Section 5, we discuss the implications of our results. In Section 6, we summarize our conclusions.

3.3 The hydrostatic tidal response

In this section, we derive the equation and general solution for the hydrostatic tidal response of a gas giant planet mostly made of H-He fluid. Tides in hydrostatic equilibrium follow Poisson's equation and a simple equation of motion

$$\nabla^2 \phi = -4\pi \mathcal{G} \rho, \tag{3.2}$$

$$\nabla p = \rho \nabla \phi. \tag{3.3}$$

The potential ϕ represents the relevant gravitational forces, p is pressure, and ρ is density. In a gas giant planet mostly made of H-He, the equation of state of the fluid can be conveniently approximated by an $n = 1$ polytrope (Stevenson, 2020), which follows

$$p = K\rho^2, \tag{3.4}$$

where K is a constant describing the material properties. The simple result $\nabla p = 2K\rho\nabla\rho$ combined with Equations (3.2) and (3.3) allows us to obtain

$$\frac{\nabla^2\phi}{k^2} + \phi = 0, \tag{3.5}$$

where $k^2 = 2\pi\mathcal{G}/K$.

The first approximation to the hydrostatic tidal response comes from considering tides as a perturbation ϕ' over a spherical planet with a spherically symmetric gravitational potential ϕ_0. Perturbation theory correctly approximates the tidal response because the tidal gravitational potential only constitutes a $\sim 10^{-6}$ part of the total gravitational potential. In such scenario, the potential ϕ can be written as

$$\phi = \phi_0 + \phi' + \phi_T, \tag{3.6}$$

where the tidal forcing potential takes the form

$$\phi_T = \sum_{\ell=2}^{\infty} \sum_{m=-\ell}^{\ell} U_\ell^m \left(\frac{r}{s}\right)^\ell Y_\ell^m, \tag{3.7}$$

$U_{\ell,m}$ is a numerical factor defined by

$$U_{\ell,m} = \left(\frac{s}{a}\right)^\ell \left(\frac{\mathcal{G}m_s}{a}\right) \left(\frac{4\pi(\ell-m)!}{(2\ell+1)(\ell+m)!}\right)^{1/2} \mathcal{P}_l^m(0), \tag{3.8}$$

$\mathcal{P}_\ell^m$ are the associated Legendre polynomials of degree ℓ and azimuthal order m, Y_ℓ^m are spherical harmonics, and m_s the mass of the satellite. The hydrostatic tidal response that solves Equation (3.5) follows (Idini and Stevenson, 2021)

$$\phi' = \sum_{\ell=2}^{\infty} \sum_{m=-\ell}^{\ell} \left(A_\ell j_\ell(kr) - \left(\frac{r}{s}\right)^\ell\right) U_\ell^m Y_\ell^m, \tag{3.9}$$

where j_ℓ is the spherical Bessel function of the first kind.

The boundary condition for ϕ' at the outer boundary of the planet defines the coefficients A_ℓ. At the outer boundary of the planet, the tidal response ϕ' should match an external potential that decays with distance r away from the planet, according to the factor $(s/r)^{\ell+1}$. Both potentials should also match in their directional derivative normal to the outer boundary of the planet. In a spherical planet, the directional derivative is simply ∂_r due to the convenient decomposition of the tidal response into an axially symmetric factor and a spherical harmonic. In an oblate planet, however, the directional derivative involves additional terms that depend on the oblate figure

of the planet. Additionally, the boundary of the planet is no longer the average radius s, but instead an oblate figure that varies with colatitute θ (i.e., roughly following a $\mathcal{P}_2(\cos\theta)$ figure). In the following section, we consider those effects to calculate A_ℓ^m and obtain first order corrections to the hydrostatic Love number due to the oblate figure of a rotating planet.

3.4 The hydrostatic tidal response in a rotating planet

In this section, we use first–order perturbation theory to illuminate on the effect that the oblate figure of a rotating planet has on the hydrostatic Love number. To q order of approximation, the oblate figure of a gas giant mostly made of H-He follows (Appendix E)

$$R(\theta) \approx s\left(1 - \frac{5}{\pi^2}q\mathcal{P}_2(\cos\theta)\right). \tag{3.10}$$

At the outer boundary of the oblate planet (i.e., $r = R(\theta)$), the gravitational tidal response requires to satisfy the boundary condition

$$\nabla\phi'(R)\cdot\hat{n} = \nabla\Theta'(R)\cdot\hat{n}, \tag{3.11}$$

where Θ is an external gravitational potential that matches ϕ' at $r = R$,

$$\Theta_\ell^{m\prime} = \left(\frac{R}{r}\right)^{\ell+1}\phi_\ell^{m\prime}(R), \tag{3.12}$$

$$\partial_r\Theta_\ell^{m\prime} = -\frac{(\ell+1)}{r}\left(\frac{R}{r}\right)^{\ell+1}\phi_\ell^{m\prime}(R), \tag{3.13}$$

$$\partial_\theta\Theta_\ell^{m\prime} = \frac{(\ell+1)}{R}\left(\frac{R}{r}\right)^{\ell+1}\phi_\ell^{m\prime}(R)\partial_\theta R + \left(\frac{R}{r}\right)^{\ell+1}\partial_\theta\phi_\ell^{m\prime}(R), \tag{3.14}$$

and $\hat{n}$ is the vector normal to the oblate surface of the planet $R(\theta)$,

$$\hat{n} = \left(1 - \frac{5}{\pi^2}q\mathcal{P}_2(\cos\theta)\right)\hat{r} - \frac{15}{\pi^2}q\cos\theta\sin\theta\hat{\theta}. \tag{3.15}$$

After applying the differential operator in spherical coordinates and keeping only terms of order q, the boundary condition reduces to

$$\sum_\ell\left(1 - \frac{5}{\pi^2}q\mathcal{P}_2(\cos\theta)\right)\partial_r\phi_\ell^{m\prime}(R) = \sum_\ell -\frac{(\ell+1)}{s}\phi_\ell^{m\prime}(R). \tag{3.16}$$

Assuming that rotation only causes a small deviation from a sphere, we can write $R = s(1 - \epsilon\mathcal{P}_2)$, where $\epsilon = 5q/\pi^2$ is a small parameter. We evaluate the hydrostatic

tidal response at the oblate outer boundary of the rotating planet by Taylor expansion of ϕ' over ϵ,

$$\phi_\ell^{m'}(R) \approx \phi_\ell^{m'}(s) - \epsilon s \partial_r \phi_\ell^{m'}(s) \mathcal{P}_2, \tag{3.17}$$

$$\partial_r \phi_\ell^{m'}(R) \approx \partial_r \phi_\ell^{m'}(s) - \epsilon s \partial_{r,r} \phi_\ell^{m'}(s) \mathcal{P}_2. \tag{3.18}$$

From Equation (3.9), the hydrostatic tidal response of a sphere evaluated at $r = s$ follows

$$\phi_\ell^{m'}(s) = (A_\ell j_\ell(ks) - 1) U_\ell^m Y_\ell^m, \tag{3.19}$$

$$\partial_r \phi_\ell^{m'}(s) = \left(A_\ell \partial_r j_\ell(ks) - \frac{\ell}{s} \right) U_\ell^m Y_\ell^m, \tag{3.20}$$

$$\partial_{r,r} \phi_\ell^{m'}(s) = \left(A_\ell \partial_{r,r} j_\ell(ks) - \frac{\ell(\ell-1)}{s^2} \right) U_\ell^m Y_\ell^m. \tag{3.21}$$

We replace Equations (3.17) and (3.18) into Equation (3.16) to obtain the final equation for the coupled hydrostatic tidal response of an oblate rotating planet,

$$\sum_\ell \left(A_\ell \left(j_\ell(ks) \left(\frac{\ell+1}{s} \right) + \partial_r j_\ell(ks) \right) - \frac{2\ell+1}{s} \right) U_\ell^m Y_\ell^m$$

$$= \frac{15}{\pi^2} q \sum_\ell \left(A_\ell \left(s \partial_{r,r} j_\ell(ks) + (\ell+2) \partial_r j_\ell(ks) \right) - \frac{\ell(2\ell+1)}{s} \right) U_\ell^m Y_\ell^m \mathcal{P}_2. \tag{3.22}$$

We use a recursive relation based on Clebsch-Gordan coefficients to calculate the coupling in spherical harmonics introduced by the term $Y_\ell^m \mathcal{P}_2$ (Idini and Stevenson, 2021),

$$Y_\ell^m \cos^2 \theta = p_{\ell-1} p_\ell Y_{\ell-2}^m + (p_\ell^2 + p_{\ell+1}^2) Y_\ell^m + p_{\ell+1} p_{\ell+2} Y_{\ell+2}^m, \tag{3.23}$$

$$p_\ell = \left(\frac{\ell^2 - m^2}{4\ell^2 - 1} \right)^{1/2}. \tag{3.24}$$

Using the recursive relation above, we can write the term that couples the spherical harmonics of the hydrostatic tidal response as

$$Y_\ell^m \mathcal{P}_2 = \frac{3}{2} \cos^2 \theta Y_\ell^m - \frac{Y_\ell^m}{2} = \frac{3}{2} p_{\ell-1} p_\ell Y_{\ell-2}^m + \left(\frac{3}{2} (p_\ell^2 + p_{\ell+1}^2) - \frac{1}{2} \right) Y_\ell^m + \frac{3}{2} p_{\ell+1} p_{\ell+2} Y_{\ell+2}^m. \tag{3.25}$$

In the following section, we use Mathematica (Wolfram, 1999) to evaluate Equations (3.8), (3.22), and (3.25) to obtain A_ℓ in the case of Jupiter when tidally perturbed by the gravitational pull of Io.

3.5 Jupiter's hydrostatic Love numbers

For the sake of simplicity, we analyze the case of coupling between Jupiter's rotational and hydrostatic tidal responses in $\ell = 2$ and $\ell = 4$, ignoring terms of higher degree. To order of magnitude, the contribution to k_{42} from $\ell = 6$ tides follows $\sim q k_{62}(R/a)^2 \sim q^2 k_{42}$, a second-order correction in q and thus neglected here. From Equation (3.22), we can write a linear system of equations in the form

$$c_1 A_2 + c_2 A_4 = c_3, \tag{3.26}$$

$$c_4 A_2 + c_5 A_4 = c_6, \tag{3.27}$$

where we obtain the c_n coefficients from evaluating the sum in Equation (3.22) truncated at $\ell = 4$ and set for $m = 2$.

Table 3.1: Rotational correction to Jupiter's hydrostatic Love number under the tidal perturbation of Io, Europa, and Ganymede.

Type[1]	polytrope[2]			CMS[3]		
	Io	Europa	Ganymede	Io	Europa	Ganymede
δk_2	1.11	1.11	1.11	1.10	1.10	1.10
δk_{42}	14.4	35.0	87.6	13.6	32.8	83.7

[1] The rotational correction $\delta k_{\ell m}$ is the ratio between the Love number in an oblate rotating Jupiter model, over the Love number in a spherical nonrotating Jupiter model. Jupiter's rotation rate follows $q = 0.0892$.

[2] We obtain the analytical results in an $n = 1$ polytrope from the ratio between Equation (3.30) and Equation (3.29).

[3] We calculate δk from Love numbers reported in Wahl et al. (2020), which were numerically obtained with the Concentric Maclaurin Spheroid (CMS) method.

Our analytical polytropic Jupiter model approximates the rotational correction to the hydrostatic Love number reported in Wahl et al. (2020) to q–order accuracy (Table 3.1). In the case of tides raised by Io, we obtain a $\sim 10\%$ increment in k_2 and an order of magnitude increment in k_{42}, both results previously reported in numerical calculations using the Concentric Maclaurin Spheroids (CMS) method (Wahl et al., 2016, 2020). The order of magnitude enhancement in k_{42} comes from the the tidal response to the $\ell = 2$ tidal forcing rotationally–coupled into the $\ell = 4$ gravitational field. We calculate the rotational correction $\delta k_{\ell m}$ in Table 3.1 as the ratio between the Love number in an oblate rotating polytrope over the Love number in a spherical

nonrotating polytrope,

$$\delta k_{\ell m} = \frac{k_\ell}{k_\ell^{(s)}}. \tag{3.28}$$

The Love number in a spherical nonrotating polytrope follows (Idini and Stevenson, 2021)

$$k_\ell^{(s)} = \left(\frac{2\ell + 1}{\pi}\right) \frac{j_\ell(\pi)}{j_{\ell-1}(\pi)} - 1, \tag{3.29}$$

while the Love number in an oblate rotating polytrope follows (i.e., from evaluating Equations (3.7) and (3.9) at $r = s$)

$$k_\ell = A_\ell j_\ell(\pi) - 1, \tag{3.30}$$

where the A_ℓ coefficients come from solving Equations (3.26) and (3.27). In the case of Jupiter's rotation ($q = 0.0892$) and Io's semimajor axis, we obtain $A_2 = 5.19$ and $A_4 = 42.2$. For the sake of comparison, the nonrotating $n = 1$ polytrope in hydrostatic equilibrium produces $A_2 = 5$ and $A_4 = 17.3$.

We can apply our rotational corrections calculated from Equation (3.28) to the nonrotating Love numbers of a Jupiter model with a more realistic equation of state and density profile (i.e., Wahl et al. (2020)). Our Io results agree with the CMS results within a margin of 2% and 3% for k_2 and k_{42}, respectively (Table 3.2). The difference between both results comes from second order effects not included in our analysis. As we show here, the correct Love number in a rotating planet comes from the boundary condition that forces the smoothness of the tidal gravitational potential over an oblate planetary figure.

Table 3.2: Jupiter's hydrostatic Love numbers under the tidal perturbation of Io, Europa, and Ganymede.

	CMS Nonrotating[1]	$n = 1$ polytrope[2] Io	CMS[3] Io	Europa	Ganymede
k_2	0.5364	0.60	0.5898	0.5894	0.5893
k_{42}	0.1279	1.8	1.7432	4.1975	10.7058

[1] Numerical results obtained with the Concentric Maclaurin Spheroid (CMS) method applied to a nonrotating Jupiter model that follows an equation of state derived from ab initio simulations (Wahl et al., 2020).

[2] We obtain the analytical results in an $n = 1$ polytrope from applying the fractional correction in Equation (3.28) to the nonrotating result.

[3] CMS Numerical results for the Love number of a rotating Jupiter model (Wahl et al., 2020).

3.6 Discussion

The lost meaning of Love numbers in rotating gas giant planets

High–degree tesseral Love numbers ($\ell > m$, $m \geq 2$) lose their original meaning in a rotating planet with an oblate figure. As first proposed by A.E.H. Love in 1909, Love numbers represent the tidal response of a planet normalized by the tidal forcing, both at the same ℓ, m spherical harmonic. Accordingly, the hydrostatic tidal gravitational field of a spherical planet is a sum over terms $k_{\ell,m}\phi_{\ell,m}^T$. In this original meaning, the Love number represents an interior property of the planet. In the context of gas giant exoplanets, the Love number may describe the degree of central concentration of mass, with a lower Love number indicating a more centrally concentrated planet (Batygin et al., 2009). However, the coupling introduced by rotation complicates this convenient picture.

As shown in Equation (3.17), the hydrostatic tidal response to the forcing at a given ℓ contains terms from multiple spherical harmonics. Rotation introduces a significant term with $\ell = 4$ spherical harmonic corresponding to part of the tidal response to the $\ell = 2$ tidal forcing. In fact, this term dominates Jupiter's $\ell = 4$ tidal gravitational field, with 7% of the amplitude arising from the tidal response to the $\ell = 4$ tidal forcing and 93% from the tidal response to the $\ell = 2$ tidal forcing coupled by the oblate figure of the planet (Table 3.1). According to this new term, the $\ell = 4$ tidal gravitational field is (Equation (3.17)),

$$\phi_4^{2\prime} \sim \frac{5}{\pi^2}q\phi_2^{2\prime}\mathcal{P}_2 \sim \frac{5}{\pi^2}q\left(\frac{r}{s}\right)^2 k_2 U_{2,2}Y_4^2. \tag{3.31}$$

When computing k_{42} after normalization of Equation (3.31) by the tidal forcing ϕ_{4T}^2, the term introduced by rotation promotes a dependency of k_{42} on the semimajor axis of the satellite,

$$k_{42} \sim \frac{5}{\pi^2}q\left(\frac{a}{s}\right)^2 k_2. \tag{3.32}$$

Explicitly revealed here using perturbation theory, the dependency of k_{42} on semi-major axis was previously observed in numerical results obtained with CMS (Wahl et al., 2017a, 2020). The difference in k_{42} among the Galilean satellites can be explained by the orbital factor $(a/s)^2$, where a/s is roughly 6 for Io, 10 for Europa, and 15 for Ganymede (Table 3.1).

The 7σ discrepancy observed by Juno

Our analytical results validate the accuracy of CMS to obtain the hydrostatic k_{42} (Table 3.2), confirming a 7σ discrepancy between Juno's k_{42} and hydrostatic tides at

perijove 17. The CMS hydrostatic k_{42} requires a $\Delta k_{42} \approx -15\%$ fractional correction to fit the Juno observation within 3σ. Due to rotational coupling (Equation (3.32)), one part of the required correction comes from dynamical effects on k_2 that include the Coriolis effect. The $\Delta k_2 \approx -4\%$ effect introduced by dynamical tides (Idini and Stevenson, 2021; Lai, 2021) reduces the fractional correction required by Juno to $\Delta k_{42} \approx -11\%$. This residual effect must come from additional dynamical effects related to the $\ell = 4$ tidal response, which is only a small fraction (7%) of the hydrostatic k_{42}. At perijove 17, Juno 3σ uncertainty on k_2 is only 3% (Idini and Stevenson, 2021), much smaller than the required $\Delta k_{42} \approx -11\%$. Consequently, additional hypothetical dynamical effects applied to k_2 are constrained by Juno to be small and insufficient. We require future studies to understand the origin of the Δk_{42} fractional correction required to fit Juno observations.

The uncertainty $\sigma = 0.063$ at perijove 17 depends on imposing the same Love number for all Galilean satellites. When k_{42} is let to freely vary among satellites, an orbital resonance between the Juno spacecraft and Io–Europa–Ganymede (in mean–motion resonance 1:2:4) conspires against a unique decomposition of the joint tidal gravitational field, leading to a tradeoff among individual contributions that sharply increases uncertainty ($\sigma = 0.353$ for Io). Future perijove passes from Juno's extended mission will break the tradeoff given a recent change in Juno's orbital period. Currently, the best representation of Jupiter's k_{42} due to Io's gravitational pull comes from assuming a reasonable a priori constraint to the k_{42} caused by the other satellites. Imposing the same Love number to all Galilean satellites equals to assume that Io dominates the k_{42} tidal gravitational field, which is true unless Europa or Ganymede cause a tidal resonance with Jupiter.

3.7 Conclusions

We used first–order perturbation theory to calculate the rotational correction to Jupiter's hydrostatic Love number k_{42}. We showed that the oblate figure of the rotating planet forces the $\ell = m = 2$ tidal response to couple into the $\ell, m = 4, 2$ tidal gravitational field, increasing the hydrostatic k_{42} beyond an order of magnitude for Io and roughly by two orders of magnitude for Ganymede. As a result, we conclude that low–degree hydrostatic Love numbers dominate high–degree hydrostatic tesseral Love numbers ($\ell > m, m \geq 2$), and thus the latter provide little additional information about interior structure. The exception is the case where dynamical effects particular to a given high–degree Love number acquire relevant amplitude due to, for example, tidal resonances.

Our analysis leads to important implications for the correct interpretation of a 7σ anomaly in Jupiter's k_{42} as observed by NASA's Juno mission. The Juno k_{42} anomaly is slightly attenuated by the coupled $\ell = 2$ dynamical tides ($\Delta k_2 \approx -4\%$). At Juno's mid–mision perijove 17, Jupiter's hydrostatic Love number k_{42} requires an additional fractional correction $\Delta k_{42} \approx -11\%$ from unknown dynamical effects associated to its tidal response to the $\ell = 4$ tidal forcing. We require further analysis to unravel the origin of the required fractional correction.

C h a p t e r   4

THE GRAVITATIONAL IMPRINT OF AN INTERIOR–ORBITAL RESONANCE IN JUPITER–IO

"You've got me locked in"

— Judas Priest, *Locked In*

4.1   Abstract

At mid-mission perijove 17, NASA's Juno mission has revealed a 7σ discrepancy between Jupiter's observed high–degree tidal response and the theoretical equilibrium tidal response, namely the Love number k_{42}. Here, we propose an interpretation for this puzzling disagreement based on an interior–orbital resonance between internal gravity waves trapped in Jupiter's dilute core and the orbital motion of Io. We use simple Jupiter models to calculate a fractional correction Δk_{42} to the equilibrium tidal response that comes from the dynamical tidal response of a g–mode trapped in Jupiter's dilute core. Our results suggest that an extended dilute core ($r \gtrsim 0.7 R_J$) produces an interior–orbital resonance with Io that modifies Jupiter's tidal response in $\Delta k_{42} \sim -11\%$, allowing us to fit Juno's k_{42}. In our proposed self–consistent scenario, Jupiter's dilute core evolves in resonant locking with Io's orbital migration, which allows the interior–orbital resonance to persist over geological timescales. This scenario requires a dilute core that becomes smoother or shrinks over time, together with a ${}_{4}^{2}g_1$ mode ($\ell, m, n = 4, 2, 1$) with resonant tidal dissipation reaching $Q_4 \sim 1000$. Jupiter's dilute core evolution path and the dissipation mechanism for the resonant ${}_{4}^{2}g_1$ mode are uncertain and motivate future analysis. No other alternative exists so far to explain the 7σ discrepancy in Juno k_{42}. Our proposed interior–orbital resonance can be tested by Juno observations of k_{42} tides raised on Jupiter by Europa as obtained at the end of the extended mission (mid 2025), and by future seismological observations of Jupiter's ${}_{4}^{2}g_1$ mode oscillation frequency.

4.2 Introduction

In the traditional view of Jupiter's interior, an envelope of H-He fluid with small traces of heavier elements overlays a compact core of $10 - 20M_E$ made entirely of elements heavier than H-He (Guillot, 2005). The traditional view follows from the simplest scenarios of planet formation via core accretion (Mizuno, 1980; Mizuno et al., 1978; Perri and Cameron, 1974; Pollack et al., 1996; Safranov, 1969), ignoring the disaggregation or dissolution of incoming planetesimals that recent work considers (Bodenheimer et al., 2018; Helled and Stevenson, 2017). An adiabatic Jupiter requires $10 - 20M_E$ of heavy elements to attain its observed radius, irrespective of how those heavy elements distribute inside the planet. However, no direct geophysical evidence exists to justify the presence of a compact core over a smoother distribution of heavy elements. Opposing the traditional view, Juno recently obtained accurate zonal gravitational moments $J_{2\ell}$ that suggest that heavy elements distribute broadly along the radius rather than tightly concentrating near the center in a compact core (Miguel et al., 2022; Wahl et al., 2017b) (Militzer et al., 2022).

In addition to $J_{2\ell}$, Juno also recently obtained accurate Love numbers that contain Jupiter's tidal response to the gravitational perturbation caused by the Galilean satellites. Intriguinly, the high–degre Love number k_{42} observed by Juno is 7σ away from the hydrostatic k_{42} calculated in a Jupiter model that fits the observed radius, J_2, and J_4 (Durante et al., 2020; Wahl et al., 2020). The Love number k_{42} represents the $\ell, m = 4, 2$ spherical harmonic term in Jupiter's tidal gravitational field normalized by the respective tidal forcing spherical harmonic term. The oblate figure of Jupiter introduces part of the tidal response to the $\ell = 2$ tidal forcing into the $\ell = 4$ tidal gravitational field, enhancing k_{42} then compared to a hypothetical spherical Jupiter. In the case of tides raised on Jupiter by Io, only 7% of k_{42} corresponds to the tidal response to the $\ell = 4$ tidal forcing and the remaining 93% corresponds to the coupled k_2 ($\ell = m = 2$) (Idini and Stevenson, 2022).

Here, we use simple Jupiter models to propose an explanation to the 7σ disagreement between Juno and the hydrostatic k_{42}. We calculate a fractional correction to the hydrostatic k_{42} introduced by the dynamical response of Jupiter's dilute core to tidal excitation. The hypothesized dilute core promotes static stability in the interior of Jupiter, allowing internal gravity waves to propagate and organize in normal modes of oscillation (i.e., g–modes) restored by buoyancy (Fuller, 2014; Mankovich and Fuller, 2021). Our proposal depends on an interior–orbital resonance between g–

modes trapped in Jupiter's dilute core and the orbital motion of Io, a scenario that is highly unlikely to happen by pure chance. Accordingly, we invoke a state of resonant locking (Fuller et al., 2016) to allow the required interior–orbital resonance to remain active over geological timescales.

Our results support a previous suggestion that Jupiter's dilute core may extend as far as $\sim 0.7 R_J$ (Militzer et al., 2022), without allowing us to rule out a less extended dilute core. A future tight constraint to the extension of Jupiter's dilute core will lead to important consequences for our current understanding of the formation and evolution of gas giants. Extending outwards from a compact core, a narrow compositional gradient appears in some standard core accretion models (Helled and Stevenson, 2017). Double–diffusive convection could potentially broaden a narrow compositional gradient near the center by upward transport of heavy elements. On the other hand, convection over the age of Jupiter (~ 4.5 Ga) promotes mixing in the envelope, potentially erasing compositional gradients that extend too far from the center (Müller et al., 2020). Perhaps an extended compositional gradient survives convective mixing only in the case of a "cold" formation process (Vazan et al., 2018), which is not compatible with standard core accretion models (Müller et al., 2020). Alternatively, a head-on giant impact could disturb Jupiter after formation, leading to an extended compositional gradient resistant to convective mixing (Liu et al., 2019). However, head–on giant impacts occur rarely and oblique giant impacts may not accomplish the desired heavy element distribution (Helled et al., 2022).

4.3   An interior–orbital resonance solves the Juno discrepancy

At mid–mission perijove 17, Juno registers a 7σ discrepancy in the observed k_{42} when compared to the hydrostatic k_{42} expected in a rotating Jupiter model that follows a density profile consistent with the observed radius and Juno zonal gravity up to J_4 (Durante et al., 2020; Wahl et al., 2020). The hydrostatic Love number is $k_{42} = 1.743 \pm 0.002$ (Wahl et al., 2020), while the Juno observation is $k_{42} = 1.289 \pm 0.063$ (1σ) (Durante et al., 2020). The hydrostatic k_{42} requires a fractional correction $\Delta k_{42} \approx -15\%$ to be reconciled at 3σ with the k_{42} observed by Juno.

One part of the required fractional correction comes from the -4% effect introduced by $\ell = 2$ f–mode dynamical tides on k_2 (Dewberry and Lai, 2022; Idini and Stevenson, 2021; Lai, 2021) and coupled by the oblate figure of the planet into the $\ell = 4$ gravitational field (Idini and Stevenson, 2022). The $\ell = 4$ f–mode dynamical tide produces a negligible effect on k_{42}, thus the remaining $\Delta k_{42} \approx -11\%$ comes

from additional dynamical effects related to the tidal response of nonfundamental modes to the $\ell = 4$ tidal forcing.

In the rest of this section, we present a self–consistent scenario where resonantly enhanced internal gravity waves trapped in Jupiter's extended dilute core produce the tidal gravity required to reconcile the 7σ Juno discrepancy.

Instead of a compact traditional core, gas giant planets most likely host a dilute core where the abundance of heavy elements changes with depth (Fuller, 2014). Recent observations of normal oscillations in Saturn's rings confirm this picture in Saturn (Mankovich and Fuller, 2021), whereas high–degree zonal gravitational coefficients observed by Juno suggest an analogous situation in Jupiter (Wahl et al., 2017b). Contrary to a homogeneous envelope, a dilute core permits the propagation of internal gravity waves (i.e., waves restored by buoyancy) that organize in normal modes of oscillation called g–modes. The oscillation frequency of g–modes spans a wide frequency range that includes the forcing tidal frequency of the Galilean satellites. Consequently, in a gas giant planet hosting a dilute core, the orbital motion of the satellites may resonate with internal gravity waves trapped in the dilute core, leading to what we denominate an interior–orbital resonance. As we show in Section 4.5, internal gravity waves trapped in the dilute core fail at producing enough gravity to explain Juno's observation when out of resonance.

The tidal excitation of g–modes trapped inside Jupiter's dilute core produces a fractional correction Δk_{42} to the hydrostatic Love number defined as

$$\Delta k_{42} = \frac{k_{42}}{k_{42}^{(hs)}} - 1, \tag{4.1}$$

where k_{42} is the dynamical Love number (Appendix F) and $k_{42}^{(hs)} \approx 0.12$ the hydrostatic Love number (Idini and Stevenson, 2022), both calculated in an $n = 1$ polytrope. The $n = 1$ polytrope closely approximates the equation of state of H-He, the elements that dominate the composition of gas giant planets (Stevenson, 2020). We use perturbation theory to obtain the Δk_{42} required by Juno rather than directly trying to fit the observed k_{42}. A polytropic equation of state and our perturbative approach greatly simplify an otherwise much more complicated numerical procedure without compromising the generality of our results.

A gyrotidal effect on Jupiter couples Love numbers to rotation (Idini and Stevenson, 2022; Dewberry and Lai, 2022) and introduces an additional complication when comparing Equation (4.1) to the fractional correction required by Juno. Due to the

gyrotidal effect, an interior–orbital resonance only affects the contribution to k_{42} that comes from the $\ell = 4$ tidal forcing, which represents only a small fraction (7%) of the total k_{42} associated to Io (Idini and Stevenson, 2022); the contribution to k_{42} from the nonresonant coupled response to the $\ell = 2$ forcing remains hydrostatic. Consequently, we calculate the g–mode fractional dynamical correction Δk_{42} as

$$\Delta k_{42} \simeq 0.07 \left(\frac{4\pi}{9k_{42}^{(\text{hs})}}\right) \left(\frac{Q^2}{\omega_g^2 - (2C\Omega + \omega)^2}\right), \tag{4.2}$$

where the numerical factor 0.07 accounts for Jupiter's gyrotidal effect, ω_g is the g–mode frequency, ω is the tidal frequency, Q is the dimensionless coupling integral that represents how well the tidal forcing couples to the eigenvector of the normal mode, and C is the dimensionless amplitude of the first–order correction to the mode frequency due to Jupiter's rotation rate Ω,

$$Q = \frac{4\pi}{MR^\ell} \int_0^R r^{\ell+2} \delta\rho^* dr, \tag{4.3}$$

$$C = \frac{4\pi}{MR^2} \int_0^R \left(2\xi_r\xi_\perp + \xi_\perp^2\right) \rho r^2 dr, \tag{4.4}$$

where $\delta\rho^*$ is the complex conjugate of the Eulerian densitiy perturbation of the mode, ξ_r is the radial eigenfunction of the mode, and $\xi_\perp$ is the horizontal eigenfunction of the mode. At $\ell = 4$, rotation produces only a small shift on the g–mode frequency (e.g., $C \leq 0.05$ for models shown in this paper), thus resonances still appear roughly at $\omega_g \approx \omega$. At a given satellite, the tidal frequency at $m = 2$ follows

$$\omega = -2(\Omega - \omega_s), \tag{4.5}$$

where ω_s is the orbital frequency of the satellite that depends on the semimajor axis according to $\omega_s \propto a^{-3/2}$.

To fit the Juno observation, we require to approach an interior–orbital resonance from the resonance branch that produces a negative fractional correction to k_{42}. According to Equation (4.2), we obtain the required negative fractional correction only when $|\omega| > \omega_g$. Pure chance hardly favors an interior–orbital resonance in the hypothetical scenario that the Galilean satellites are randomly placed in orbit around Jupiter. Tidal torques constantly force the satellite to migrate outwards, increasing the semimajor axis a and ω over time. Likewise, the dilute core structure evolves over time due to convection (either overturning convection or double–diffusive convection), correspondingly changing the g–mode frequency. Resonant locking

(Appendix G) allows us to circumvent the invocation of a historical coincidence to explain why these two frequencies match in present days. Resonant locking is an equilibrium state where the evolution of the dilute core roughly matches the orbital migration of the forcing satellite (Fuller et al., 2016).

We propose the following scenario to maintain an interior–orbital resonance over geological timescales that produces a negative fractional correction to k_{42} and fits Juno's observation (Fig. 4.1). An initially nonresonant extended dilute core (i.e., $r \gtrsim 0.7R_J$) hosts a g–mode that evolves into higher frequency due to some kind of convection. In this initial stage, the Galilean satellites slowly migrate outward, expanding their orbits due to dissipation associated with $\ell = 2$ tides. Eventually, the g–mode frequency encounters a resonance with Io, the Galilean satellite of lowest tidal frequency. The onset of the resonance increases tidal dissipation at $\ell = 4$, accelerating Io's orbital migration until achieving a state of resonant locking (Section 4.6). The system could remain in resonant locking for geological timescales until present day, assuming that the g–mode evolved faster toward higher frequency than the orbital migration of Io while they were out of resonance.
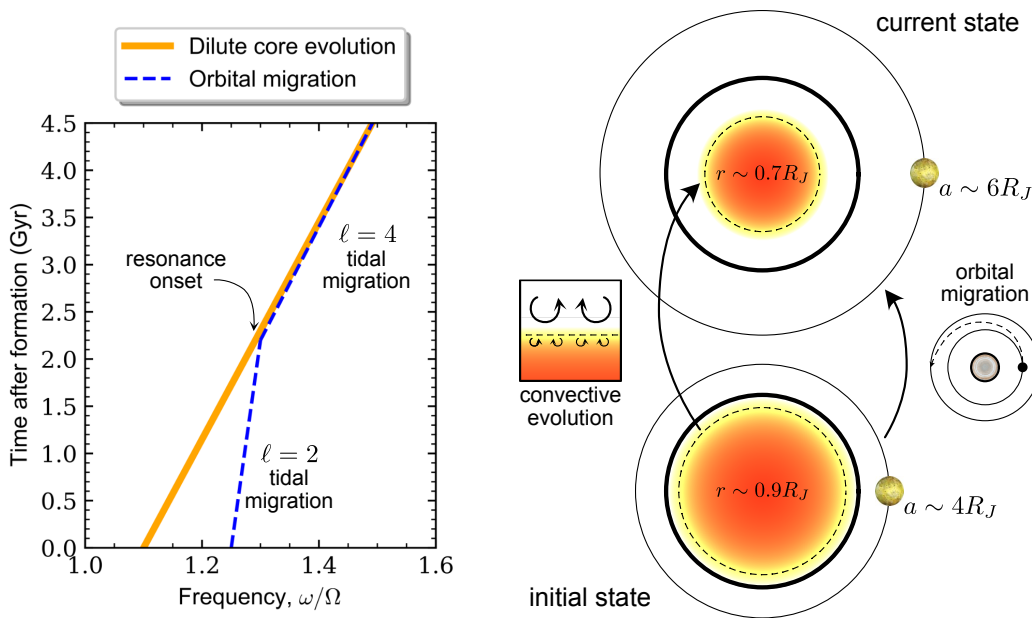
Figure 4.1: Pictographic orbital migration and dilute core evolution required to explain Juno's k_{42} using a core–orbital resonance. The dilute core forms with a g–mode frequency lower than the satellite tidal frequency. Initially out of resonance, the satellite migrates outward at an almost negligible rate. After some uncertain time, the dilute core evolves into a locked interior–orbital resonance, increasing the rate of satellite orbital migration.

In the following, we evaluate the plausibility of the scenario shown in Fig. 4.1. In Section 4.4, we describe our simple models of Jupiter's dilute core. In Section 4.5, we show that an interior–orbital resonance in Jupiter–Io prefers an extended dilute core. In Section 4.6, we calculate the tidal dissipation required to attain $\ell = 4$ resonant locking.

4.4   Jupiter dilute core models

The density ρ of a mixture of H-He fluid and heavy elements as a function of pressure p (Fig. 4.2) can be obtained from volume additivity of the individual constituents (Appendix H)

$$\frac{1}{\rho} = (1 - Z) \left(\frac{K}{p}\right)^{1/2} + \frac{Z}{\rho_z}, \tag{4.6}$$

where ρ_z is the density of heavy elements, Z the fraction of mass corresponding to elements heavier than H-He, and $K \approx 2.1 \cdot 10^{12}$ cgs represents the bulk elastic properties of the H-He fluid for a cosmic abundance of He. For simplicity, we again adopt an $n = 1$ polytrope to approximately represent the response of the H-He fluid. Provided Z is not large, the solution to Equation (4.6) is not much different from the $n = 1$ polytrope. For example, the dilute core models of Militzer et al. (2022) closely follow an $n = 1$ polytrope with a slightly different effective K (Stevenson, 2020).

For convenience, we parameterize the enrichment of heavy elements in a dilute core of width L_c and inner radius x_{ic} following (Fuller, 2014)

$$Z(x) = Z_e + (Z_c - Z_e) \sin^2 \left(\frac{\pi(x_{ic} + L_c - x)}{2L_c}\right), \tag{4.7}$$

where Z_e and Z_c represent the enrichment of heavy elements in the envelope ($x > x_{ic} + L_c$) and at center of the planet ($x < x_{ic}$), respectively. The normalized radius follows $x = kr$, where $k^2 = 2\pi G/K$. The enrichment of heavy elements decays from Z_c to Z_e following the $\sin^2$ function along the dilute core width (Fig. 4.2).

The total mass of heavy elements in our models range from 18 to 25 M_E, in agreement with estimates provided by other interior models (Guillot, 2005). We construct our dilute core models by fixing the enrichment of heavy elements in the envelope to $Z_e = 0.0167$, the value observed by two independent instruments in the Galileo entry probe. The free parameters in our models are Z_c and L_c. The presence of heavy elements shrinks Jupiter's radius when compared to a planet made of pure H-He fluid. We set the parameter x_{ic} to fit the target planetary radius $R = 3/k$ in
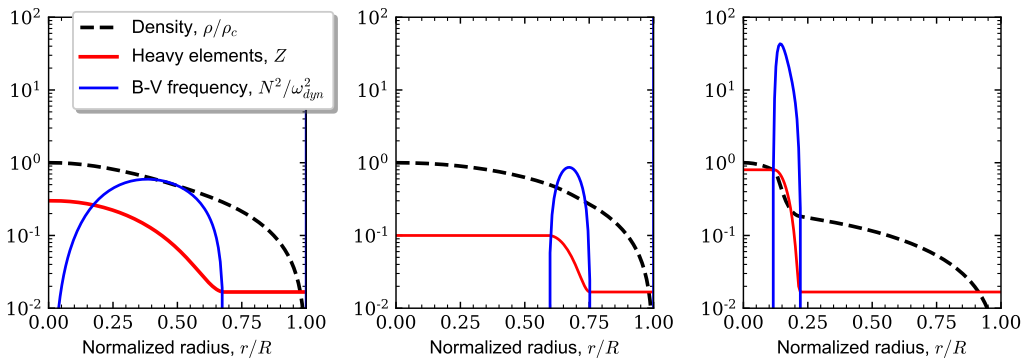
Figure 4.2: Jupiter interior models with a dilute core defined as a gradient in the enrichment of heavy elements. (a) A wide dilute core with a smooth compositional gradient similar to that proposed in Debras and Chabrier (2019), (b) a narrow dilute core with a sharp compositional gradient similar to that proposed in Militzer et al. (2022), and (c) a compact dilute core with a sharp compositional gradient constrained to a central region, similar to a traditional core. The density profile is normalized by a central density ρ_c equal to 5.8, 4.6, and 23.1 g cm^{-3}, respectively. The enrichment of heavy elements Z corresponds to the mass fraction of elements heavier than H and He. The Brunt-Vaisala (B-V) frequency is normalized by Jupiter's dynamical frequency $\omega_{dyn}^2 = \mathcal{G}M_J/R_J^3$.

all of our models. The target planetary radius ultimately constrains the total mass of heavy elements.

A compositional gradient in heavy elements introduces static stability to the interior of Jupiter, represented by the Brunt-Vaisala frequency (Fig. 4.2),

$$N^2 = g \left(\frac{1}{\gamma} \frac{\partial \ln p}{\partial r} - \frac{\partial \ln \rho}{\partial r} \right). \tag{4.8}$$

In calculating N^2, we set the first adiabatic index to $\gamma = 2$, which represents the adiabatic response of an $n = 1$ polytrope. Thermal effects could possibly modify the static stability, but those effects are small for reasonable central temperatures (Mankovich and Fuller, 2021) and neglected here.

4.5   Tidal excitation of the dilute core

In this section, we calculate the fractional dynamical correction Δk_{42} produced by the tidal excitation of our simple models of Jupiter's dilute core. We restrict our analysis to the first–order $\ell, m = 4, 2$ g–mode (i.e., $^2_4g_1$), which produces a better coupling with the respective tidal forcing compared to higher order g–modes (i.e, $^2_4g_n$ modes, where $n > 1$). We obtain ω_g, $\mathcal{Q}$, and C in Equation (4.2) using the
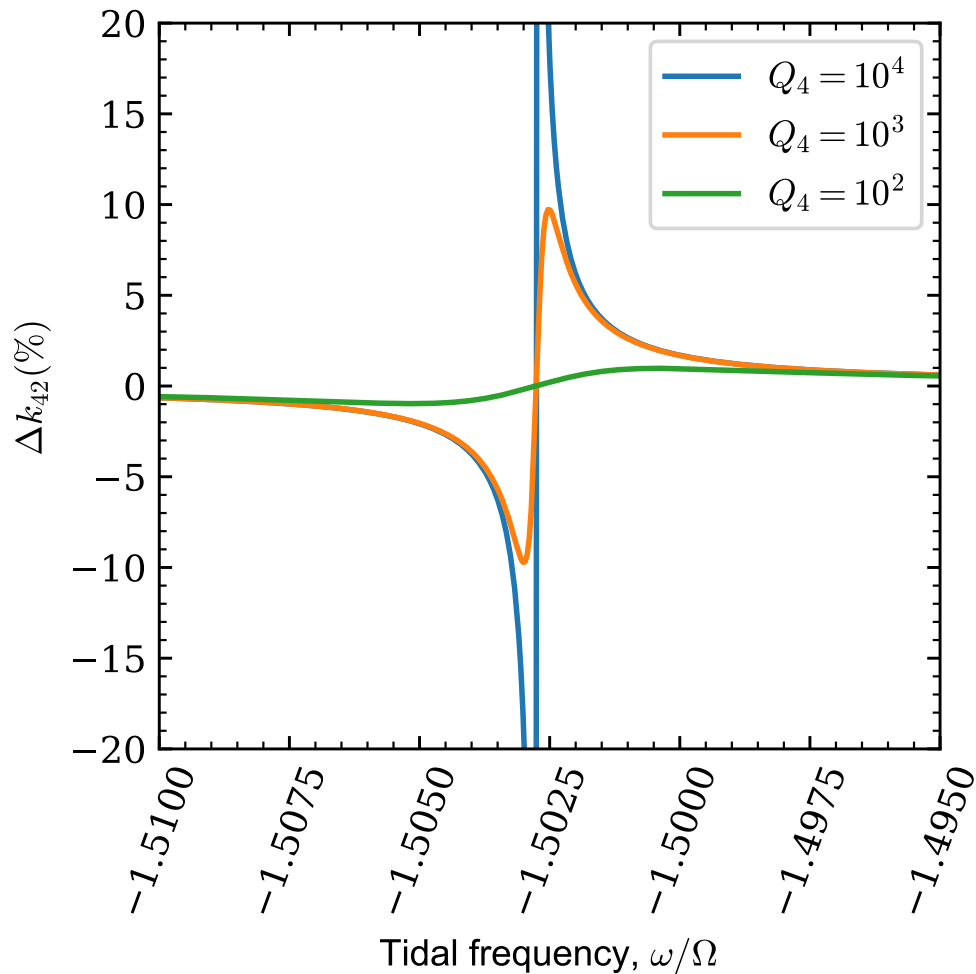
Figure 4.3: Fractional correction to the hydrostatic Love number k_{42} as a function of tidal frequency and dissipation Q_4. The dilute core model (Fig. 4.2b) produces a g_1–mode in resonance with the tidal frequency $\omega \approx -1.5\Omega$, a forcing frequency close to Io's tidal frequency $\omega_{Io} \approx -1.53\Omega$.

stellar oscillations code GYRE (Townsend and Teitler, 2013) applied to our simple Jupiter models. We observe a fractional dynamical corection capable of reaching the required $\Delta k_{42} \approx -11\%$ only when the $^2_4 g_1$ mode frequency approaches a resonance with the tidal frequency of the Galilean satellites (i.e., Fig. 4.3). The resonant model in Fig. 4.3 produces a ~1 m radial displacement of Jupiter's outer boundary in order to obtain the required gravitational signal.

The amount of tidal dissipation in the $^2_4 g_1$ mode is limited to $Q_4 \gtrsim 1000$, otherwise internal gravity waves are damped below the amplitude required to explain Juno k_{42}

(Fig. 4.3). Our account of dissipation represents only a rough estimate, following a substitution in Equation (4.2) of the g–mode frequency,

$$\tilde{\omega}_g = \omega_g \left(1 + \frac{i}{2\pi Q}\right). \tag{4.9}$$

Our simplified dissipation model is equivalent to introducing the term $\mathbf{v}/(2\pi Q)$ in the right-hand side of the equation of motion (Equation (F.1)), a term that accounts for a convenient mathematical representation of frictional damping (Ogilvie, 2009).

Our results indicate that an extended dilute core (i.e., extending as far as $\gtrsim 0.7R_J$) produces a $^2_4g_1$ mode frequency that resonates with the tidal frequency of the Galilean satellites (Fig. 4.4). Our compact dilute core models produce a $^2_4g_1$ mode frequency considerably above the tidal frequency of the Galilean satellites $\omega < 2\Omega$, thus far from resonance. We cannot rule out the possibility of a resonance in a compact core with higher order $^2_4g_n$ modes (i.e., $^2_4g_n$ modes with extra radial nodes, where $n > 1$) of worse tidal coupling because the $^2_4g_n$ mode frequency diminishes with increasing order n (Aerts et al., 2010). Consequently, we cannot constrain the extension of the dilute core purely based on the identification of an interior–orbital resonance at certain frequency. However, the lower tidal coupling of higher order $^2_4g_n$ modes leads to narrower resonances with lower saturation points, making the establishment of resonant locking harder when compared to the $^2_4g_1$ mode (Appendix G).

Can the dilute core trap a satellite in an interior–orbital resonance at $\ell = 2$? In general, the g–mode frequency scales down with lower degree ℓ (Aerts et al., 2010). At low degree ℓ and large number of radial nodes n, we can write

$$\omega_{\ell,n} \simeq \frac{\sqrt{\ell(\ell + 1)}}{\pi n} \int_0^R \frac{N}{r} dr. \tag{4.10}$$

According to Equation (4.10), the first–order $\ell = 2$ g–mode (i.e., $^2_2g_1$) approximately oscillates with a frequency that is roughly $1/\sqrt{3}$ times lower than the $^2_4g_1$ mode frequency. The g–mode spacing determined this way represents only a rough estimate because the $^2_2g_1$ and $^2_4g_1$ modes are far from the high–n asymptotic limit. Considering a current $\ell = 4$ interior–orbital resonance at $\omega_g \approx 1.5\Omega$, the corresponding $^2_2g_1$ mode frequency is $\omega_g \approx 0.87\Omega$, which is far from resonant. The $\sqrt{3}$ factor provides enough spacing between the mode frequency at different ℓ for the dilute core to evolve into a $\ell = 4$ resonance without interfering with the $^2_2g_1$ mode.

Our dilute core models could potentially produce an $\ell = 2$ interior–orbital resonance for realistic dilute core geometries (Fig. 4.5), but Juno k_2 observation argues against
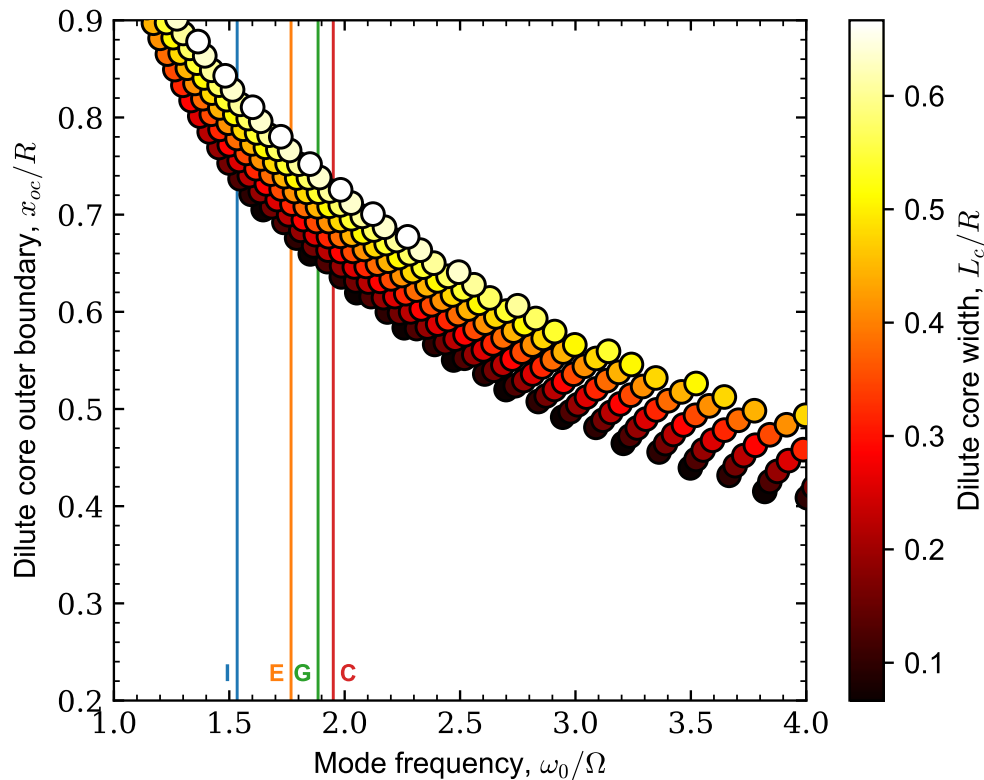
Figure 4.4: The $^2_4g_1$ mode frequency of several dilute core models. The vertical lines represent the tidal frequency $|\omega|$ of Io, Europa, Ganymede, and Callisto, from left to right, respectively.

such scenario in present times. Juno observed $k_2 = 0.565 \pm 0.006$ at perijove 17 (Durante et al., 2020), which is in close agreement with a rotating gas giant out of any significant interior resonance at $\ell = 2$ (Dewberry and Lai, 2022; Idini and Stevenson, 2021; Lai, 2021). The Juno k_2 could only admit a small near–resonance effect of a few percent, which would not be enough to explain the $\Delta k_{42} \approx -11\%$ required to reconcile the 7σ discrepancy in k_{42}.

4.6 Constraints to tidal dissipation imposed by resonant locking

In this section, we show that the $\ell = 4$ tidal bulge can dominate the orbital migration of a satellite over the migration produced by $\ell = 2$ tides, a requirement to establish a long–lived $\ell = 4$ interior–orbital resonance via resonant locking.

The orbit of a satellite evolves in time due to a gravitational torque Γ exerted on the satellite by the tidal bulge raised on the planet. In particular, the semimajor axis of a satellite of mass m_s evolves as $\dot{a} \propto \Gamma$, with the gravitational torque following

(Murray and Dermott, 1999)

$$\Gamma_\ell = -m_s \frac{\partial \left({}^m_\ell \Theta' \right)}{\partial \alpha}, \tag{4.11}$$

where α is the angle that the tidal bulge lags behind the gravitational pull of the satellite due to tidal dissipation. The tidal bulge produces an external potential Θ proportional to $r^{-(\ell+1)} \mathcal{P}_\ell(\cos \alpha)$, which is a solution to Laplace's equation. The $\ell = 2$ external potential evaluated at the position of the satellite can be written as

$$ {}^2_2\Theta' = \frac{\mathcal{G} m_s}{a} \left(\frac{s}{a} \right)^5 k_2 \mathcal{P}_2(\cos \alpha_2), \tag{4.12}$$

where s is the average planetary radius.

The oblate figure of a rotating planet introduces significant changes to the structure of the tidal gravitational field. The $\ell = 4$ tidal gravitational field acquires a new coupled nonresonant term from the $\ell = 2$ tidal forcing, in addition to the term related to the direct response to the $\ell = 4$ tidal forcing (Idini and Stevenson, 2022). The external potential induced by the coupled nonresonant term and the direct term evaluated at the satellite position are, respectively,

$$ {}^2_4\Theta' \sim \frac{5q}{\pi^2} \frac{\mathcal{G} m_s}{a} \left(\frac{s}{a} \right)^7 k_2 \mathcal{P}_4(\cos \alpha_4), \tag{4.13}$$

$$ {}^2_4\Theta' = \frac{\mathcal{G} m_s}{a} \left(\frac{s}{a} \right)^9 k_{42} \mathcal{P}_4(\cos \alpha_4), \tag{4.14}$$

where q is the dimensionless rotational parameter of a planet of mass M,

$$q = \frac{\Omega^2 s^3}{\mathcal{G} M}. \tag{4.15}$$

We explicitly indicate different lag angles α_ℓ because dissipation can vary depending on the proximity between the tidal frequency and the mode frequency. The angle α increases when the mode frequency approaches a resonance with the tidal frequency. In Equation (4.13), the relevant mode frequency is the $\ell = 2$ $f-$mode, which is much higher than the tidal frequency of the Galilean satellites and hence leads to a comparatively small α_4. In Equation (4.14), on the other hand, the relevant mode frequency is the ${}^2_4 g_1$ mode, which can resonate with Io's tidal frequency, leading to a comparatively large α_4.

Assuming that α remains a small angle in all cases, we compare the evolution of the satellite's semimajor axis promoted by the $\ell = 2$ tidal torque and the two $\ell = 4$ tidal

torques. The coupled nonresonant term and the direct term produce significantly different migration rates, respectively,

$$\frac{\dot{a}_2}{\dot{a}_4} \sim \frac{3\pi^2}{50q} \left(\frac{Q_4}{Q_2}\right) \left(\frac{a}{s}\right)^2,$$ (4.16)

$$\frac{\dot{a}_2}{\dot{a}_4} = \frac{3}{10} \left(\frac{k_2}{k_{42}}\right) \left(\frac{Q_4}{Q_2}\right) \left(\frac{a}{s}\right)^4,$$ (4.17)

where we use $2\alpha_\ell \approx Q_\ell^{-1}$, and Q_ℓ is the tidal dissipation at a given degree ℓ.

We require $Q_4 \lesssim 1000$ for the $\ell = 4$ external potential in Equations (4.13) and (4.14) to significantly contribute to Io's orbital migration (i.e., $\dot{a}_4 \gtrsim \dot{a}_2$), under the reasonable parameters $q \sim 0.1$, $a/s \approx 6$, $k_2/k_{42} \approx 0.4$, and $Q_2 \sim 10^5$. The nonresonant potential in Equation (4.13) hardly produces the low Q_4 required in the analysis above, and therefore produces a negligible contribution to orbital migration. However, the external potential in Equation (4.14) can reach the relatively low Q_4 required as a result of a resonance between Jupiter's $^2_4g_1$ mode and the tidal frequency associated to Io (Fuller et al., 2016). In this case, the dissipation in the required low Q_4 describes kinetic energy leaving the $^2_4g_1$ mode mostly due to energy cascading into higher degree $^2_\ell g_1$ modes ($\ell > 4$) sustained by mode coupling. Particularly for internal gravity waves, dissipation mostly occurs in the turbulent breaking of oscillations at short wavelengths. Currently, no widely accepted explanation exists for the origin of the tidal Q inside gas giant planets, which should be the subject of future work.

The Q_4 required to guarantee dominance of the $\ell = 4$ tidal torque (upper bound) is of the same order of magnitude than the Q_4 required to obtain the necessary gravitational effect to explain Juno's k_{42} (lower bound), namely $Q_4 \sim 1000$. The coincidence suggests a limitation in our proposal, which can be resolved by the following possibilities. Firstly, the upper bound extends upward if Q_2 is higher than what has been assumed so far, a possibility we discuss in further detail in Section 4.7. Secondly, the linear approach implied in Fig. 4.3 and Equation (4.9) may not adequately represent tidal dissipation to the extend required in this problem. Finally, we should consider the fortuitous possibility that the current dissipation lies at $Q_4 \sim 1000$. Notwithstanding these concerns, there is no known alternative to explain the k_{42} observed by Juno.
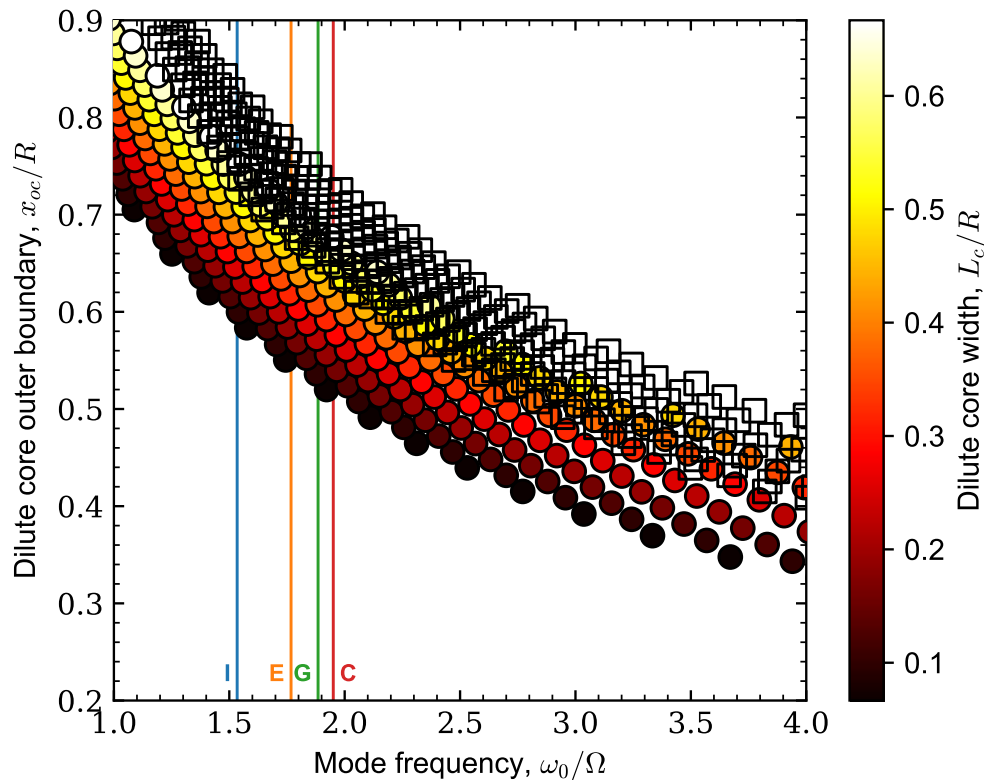
Figure 4.5: Same as Fig. 4.4 but for the $^2_2g_1$ mode frequency. The empty rectangles show the higher–frequency $^2_4g_1$ mode of the same dilute core models.

4.7 Discussion

Previous estimates of Jupiter's tidal dissipation

A century of astrometric observations of the Galilean satellites ephemerides constrains Jupiter's recent dissipation to $k_2/Q_2 \approx 10^{-5}$, which leads to $Q_2 \approx 6 \cdot 10^4$ for a realistic $k_2 \approx 0.6$ (Lainey et al., 2009). The analysis assumes the same Jupiter k_2/Q_2 at each satellite (i.e., no dynamical tides) and neglects any contribution to orbital migration from k_{42}/Q_4 or other higher degree tides. A different set of assumptions may lead to a much larger Jupiter's Q_2 than previously considered, which would allow us to reconcile our upper ($Q_4 \gtrsim 1000$) and lower bound ($Q_4 \lesssim 1000$) on Q_4. In particular, our scenario suggest a resonant $k_{42}/Q_4 \sim 10^{-3}$ that in principle could contribute to set Io's ephemerides as registered in the last century, allowing k_2/Q_2 to assume a lower value while maintaining the same secular migration rate $\dot{a} \sim 10$ cm/yr. A small k_2/Q_2 is in agreement with the nonresonant $Q_2 \sim 10^6$ predicted by dynamical tide theories of gas giant planet dissipation (Ogilvie and Lin, 2004b).

Further analysis is required to test this hypothesis.

In our proposed scenario, an interior–orbital resonance vigorously pushes Io outward against the mean-motion resonance with the other Galilean satellites. A short-lived eccentricity cycle (Ojakangas and Stevenson, 1986) can explain the astrometic suggestion that Io has migrated inward in the last century without compromising our proposal of outward migration at a longer secular timescale. The width of the resonance required to maintain resonant locking is $\delta\omega \sim 0.3$ μHz (Fig. 4.3 with Jupiter's spin–rate $\Omega \approx 170$ μHz). Astrometry suggest that Io's orbital migration is $\dot{\omega}_s/\omega_s \sim 10^{-11}$/yr in the last century (Lainey et al., 2009). When we apply the currently observed migration rate over a period of 100 years, Io's migration only changes the tidal frequency by $\Delta\omega_s \sim 4 \cdot 10^{-8}$ μHz (Io's orbital frequency $\omega_s \approx 41$ μHz), a quantity much smaller than the width of the resonance. Io would require more than ~1 Gyr to migrate out of the proposed resonance at the migration rate observed by Lainey et al. (2009).

Evolution of Jupiter's dilute core

Orbital evolution can drive a satellite into a transient resonance with a normal mode for normal modes with frequency $\omega_\alpha < 2\Omega$. However, satellites evolve fast out of the resonance due to the temporally acquired enhanced dissipation. In a planet where normal modes assume a spectrum fixed in time (i.e., no planetary evolution), the observation of an interior–orbital resonance becomes a historical coincidence.

Jupiter's dilute core possibly evolves as convective currents erode the dilute core from the top. Due to dilute core erosion, an initially smooth compositional gradient turns sharper over geological timescales, reducing the effective width and extension of the dilute core. For a fixed dilute core outer boundary, our models show that the $^2_4 g_1$ mode frequency evolves towards lower frequency as the dilute core becomes narrower (Fig. 4.4). Alternatively to dilute core erosion, double diffusive convection promotes a contrary evolution path for the dilute core, increasing the effective width and extension of the dilute core. The $^2_4 g_1$ mode frequency in our models evolves towards higher frequency as the dilute core becomes wider at fixed extension (Fig. 4.4). Inertial modes restored by the Coriolis force are unlikely to lead to long–lived interior–orbital resonances because the inertial mode frequency mostly depends on the planet's rotation rate (Dewberry and Lai, 2022), which rapidly evolves into an essentially constant value a few hundred million years after formation. The possibility of a slowly evolving inertial mode matching the evolution of the Galilean

satellites should be assessed in a future effort.

Principal uncertainties in our proposal

Our proposed scenario of a long–lived interior–orbital resonance contains large uncertainties. The evolution rate of the dilute core is hard to estimate and it should be high enough as to produce a $^2_4g_1$ mode evolution that exceeds the evolution rate of the Galilean satellites in the absence of resonances (Fig. 4.1). Not even the sign of the resulting change in the $^2_4g_1$ mode frequency is known, with core erosion and double diffusive convection evolving the dilute core in different directions. Even by formation or evolution, we require an initially extended dilute core with a compositional gradient located at $r \gtrsim 0.7R_J$ to obtain an initial $^2_4g_1$ mode frequency that is lower than Io's current tidal frequency. Formation models struggle to produce an extended dilute core that survives convective mixing over the age of the solar system (Liu et al., 2019; Müller et al., 2020; Vazan et al., 2018).

The duration of the interior–orbital resonance and the initial dilute core structure are also uncertain. If the dilute core formed with an initial extension $r \sim 0.7R_J$, then the interior–orbital resonance needs to be short-lived to produce almost negligible migration for Io over ~4.5 Gyr. If the initial dilute core reached $r \sim 0.9R_J$ and shrank or became broader over time, the interior–orbital resonance could be as old as ~1.5 Gyr assuming a resonant migration rate of ~10 cm/yr (for a compilation of current estimates, see Table 1 in Lainey et al. (2009)) and negligible migration when out of resonance. In the latter scenario of an initial dilute core with $r \sim 0.9R_J$, Io's semimajor axis can expand at most ~$2R_J$ after formation, which requires Io's formation to occur at ~$4R_J$.

Finally, interior–orbital resonances become less likely to occur with high order $^2_4g_n$ modes due to lower coupling with the tidal potential but cannot be ruled out. An interior–orbital resonance with a high order $^2_4g_n$ mode in a less extended dilute core ($r \lesssim 0.7R_J$) could alternatively explain Juno's k_{42} and also be maintained over geological timescales. In this scenario, Io is free to migrate beyond ~$2R_J$ and the initial dilute core may extend below $r \sim 0.9R_J$.

Future tidal and seismological observables of an interior–orbital resonance in Jupiter–Io

Our proposed scenario of an interior–orbital resonance can be tested against future seismological observations of Jupiter's normal modes and to a lesser extent by the Juno extended mission. We predict that Europa should raise nonresonant tides on

Jupiter following the hydrostatic $k_{42} = 4.4$ (Wahl et al., 2020). In a scenario alternative to our proposed interior–orbital resonance, the $\Delta k_{42} = -11\%$ may come from a unknown nonresonant effect and should equally apply to all satellites, leading to the prediction $k_{42} = 3.9$ for Europa. At the end of the Juno extended mission, the Europa k_{42} Juno observation will reach an uncertainty $\sigma \approx 0.4$ (Luciano Iess, personal communication, 2021 September 26), perhaps allowing us to discriminate between an interior–orbital resonant and a nonresonant model. Ultimately, we require seismological observations to robustly identify the spectrum of Jupiter's normal modes (Gaulme et al., 2011). In particular, we predict the $^2_4g_1$ mode frequency to be near Io's current tidal frequency $\omega \approx 270\ \mu$Hz.

He rain

We discard Jupiter's He rain layer as a potential contributor to the 7σ discrepancy in k_{42} observed by Juno. The He rain layer in Jupiter produces g–modes that oscillate with a frequency that is much lower than the tidal frequency of the Galilean satellites. The immiscibility of He in H produces a He gradient that starts with $Y \approx 0.24$ at $r \approx 0.85 R_J$ and ends with $Y \approx 0.28$ at $r \approx 0.75 R_J$. In this cavity, the $^2_2g_1$ mode oscillates with frequency $\omega_g \approx 0.54\Omega$ and the $^2_4g_1$ mode with frequency $\omega_g \approx 0.87\Omega$, both much lower than the lowest tidal frequency among the Galilean satellites $|\omega| \approx 1.5\Omega$ (Io). Higher order He rain g–modes oscillate at even lower frequency (Equation (4.10)). In the context of gas giant planet evolution, the He rain layer forms near the atmosphere and migrates inward in time as the planet cools down. According to Equation (4.10), consequently, the He rain layer hosted g–modes with even lower frequencies in the past.

Jupiter's dilute core and the dynamo region

In general, a dynamo region requires to be convectively unstable to produce a magnetic field. A dilute core region promotes vertical stratification of the fluid, presumably shutting down any potential dynamo activity. Recent analysis of Juno observations suggests that Jupiter hosts a dynamo region at $\sim 0.8 R_J$ capable of reproducing Jupiter's magnetic field (Connerney et al., 2022). Our extended dilute core model extends up to $\sim 0.7 R_J$, allowing convection to occur within a layer of metallic hydrogen trapped between the top of the dilute core and the bottom of He rain.

4.8 Conclusions

We used simple Jupiter dilute core models to calculate the fractional dynamical correction to Jupiter's hydrostatic Love number k_{42} from the tidal excitation induced by the Galilean satellites. After considering previously understood dynamical effects, Juno's k_{42} observation at PJ17 requires an additional fractional correction $\Delta k_{42} \approx -11\%$ to reconcile a 7σ disagreement with the hydrostatic k_{42}. Our results suggest that the required Δk_{42} can be produced by an interior–orbital resonance between Io and a ${}^{2}_{4}g_{1}$ mode (i.e., $\ell, m, n = 4, 2, 1$, a g–mode with one radial node in its eigenvector) trapped in Jupiter's dilute core. The tidal dissipation in the ${}^{2}_{4}g_{1}$ mode is limited to $Q_{4} \lesssim 1000$ or the dynamical tide is damped below the required $\Delta k_{42} \approx -11\%$. Our simple dilute core model achieves a ${}^{2}_{4}g_{1}$ mode in close resonance with Io's orbital motion when it extends as far as $r \gtrsim 0.7R_{J}$, a dilute core extension previously suggested in the analysis of zonal gravity data recorded by Juno. Less extended dilute core models could explain Juno's observed k_{42} invoking a resonance of Io with higher order ${}^{2}_{4}g_{n}$ modes (i.e., additional radial nodes in the mode eigenvector), a possible scenario that cannot be ruled out.

To avoid invoking a historical coincidence in explaining Juno's observation, we propose a scenario where the ${}^{2}_{4}g_{1}$ mode evolves roughly at a similar rate compared to the rate of Io' current orbital migration, conforming a state of resonant locking that allows the invoked resonance to remain active over geological timescales. We require a tidal dissipation $Q_{4} \lesssim 1000$ to maintain the aforementioned state of resonant locking. Our proposed self–consistent scenario depends on largely unconstrained assumptions about the long–term evolution of Jupiter's dilute core. On the short term, Juno may provide the first test for our proposal from the end–mission observation of Jupiter's k_{42} associated to tides raised by Europa. On a longer term, future seismological observations of Jupiter's normal modes can test the validity of our proposal from an observation of our predicted ${}^{2}_{4}g_{1}$ mode frequency ($\omega_{g} \approx 270$ μHz).

Chapter 5

FAULT-ZONE DAMAGE PROMOTES PULSE-LIKE RUPTURE AND BACK-PROPAGATING FRONTS VIA QUASI-STATIC EFFECTS

> *"'Cause the players gonna play, play, play, play, play,*
> *and the haters gonna hate, hate, hate, hate, hate,*
> *baby, I'm just gonna shake, shake, shake, shake, shake,*
> *I shake it off, I shake it off."*
>
> — Taylor Swift, *Shake It Off*

5.1 Abstract

Damage zones are ubiquitous components of faults that may affect earthquake rupture. Simulations show that pulse-like rupture can be induced by the dynamic effect of waves reflected by sharp fault zone boundaries. Here we show that pulses can appear in a highly damaged fault zone even in the absence of reflected waves. We use quasi-static scaling arguments and quasi-dynamic earthquake cycle simulations to show that a crack turns into a pulse after the rupture has grown larger than the fault zone thickness. Accompanying the pulses, we find complex rupture patterns involving back-propagating fronts that emerge from the primary rupture front. Our model provides a mechanism for back-propagating fronts recently observed during large earthquakes. Moreover, we find that slow-slip simulations in a highly-compliant fault zone also produce back-propagating fronts, suggesting a new mechanism for the rapid-tremor-reversals observed in Cascadia and Japan.

5.2   Introduction

Pulse-like rupture (hereafter referred to as pulses) is a common mode of earthquake propagation in which the duration of slip at each point of the fault, known as the rise-time, is short compared to the total rupture duration (Heaton, 1990). Pulses play a prominent role in the theory of earthquake mechanics: they can radically affect the earthquake energy balance (Nielsen and Madariaga, 2003), reduce the apparent strength of faults (Noda et al., 2009), enhance the spatial heterogeneity of earthquake slip and stress (Aagaard and Heaton, 2008), and promote complexity of seismicity manifested by a broad range of event magnitudes (Cochard and Madariaga, 1996). Yet their origin is not completely established. Several mechanisms of pulse generation have been proposed, involving healing fronts emerging from features of the friction law (Cochard and Madariaga, 1996; Perrin et al., 1995), from early arrest of one dimension of rupture (Day, 1982; Johnson, 1990), from fault heterogeneities (Beroza and Mikumo, 1996; Day et al., 1998) or from waves reflected in a low-velocity fault damage zone (Huang and Ampuero, 2011). The present work focuses on the generation of pulses by damaged zones.

Faults are usually embedded in a damaged zone (Fig. 5.1a) characterized in field observations by distributed fractures and micro-cracks (Chester and Logan, 1986; Mitchell and Faulkner, 2009; Savage and Brodsky, 2011) and in seismological and geodetic observations by reduced wave speeds or elastic modulus relative to the host rock (Ben-Zion et al., 2003; Cochran et al., 2009; Lewis et al., 2005; Lewis and Ben-Zion, 2010; Li et al., 2007, 2006, 1990, 2002; Mizuno et al., 2008; Peng et al., 2003; Yang and Zhu, 2010; Yang et al., 2011). Seismic imaging methods resolve fault zones of strike-slip faults as flower-structures with depth-varying thickness and damage (Ben-Zion et al., 2003; Finzi et al., 2009). Hereafter, we refer to these structures as low-velocity fault zones (LVFZ).

Dynamic rupture simulations show that the presence of a LVFZ can induce complex rupture patterns: pulses promoted by healing fronts mediated by reflected waves, oscillations of slip-rate and rupture speed, and supershear rupture at low background stress (Harris and Day, 1997; Huang and Ampuero, 2011; Huang et al., 2014, 2016). Recent earthquake cycle simulations show that the generation of pulses by a LVFZ is persistent across multiple earthquake cycles, both in fully-dynamic (Thakur et al., 2020) and quasi-dynamic simulations (Idini and Ampuero, 2017). The mechanism of pulse generation by a LVFZ has been previously attributed to the dynamic effect of waves reflected at the boundary of the LVFZ, which tend to unload the fault and
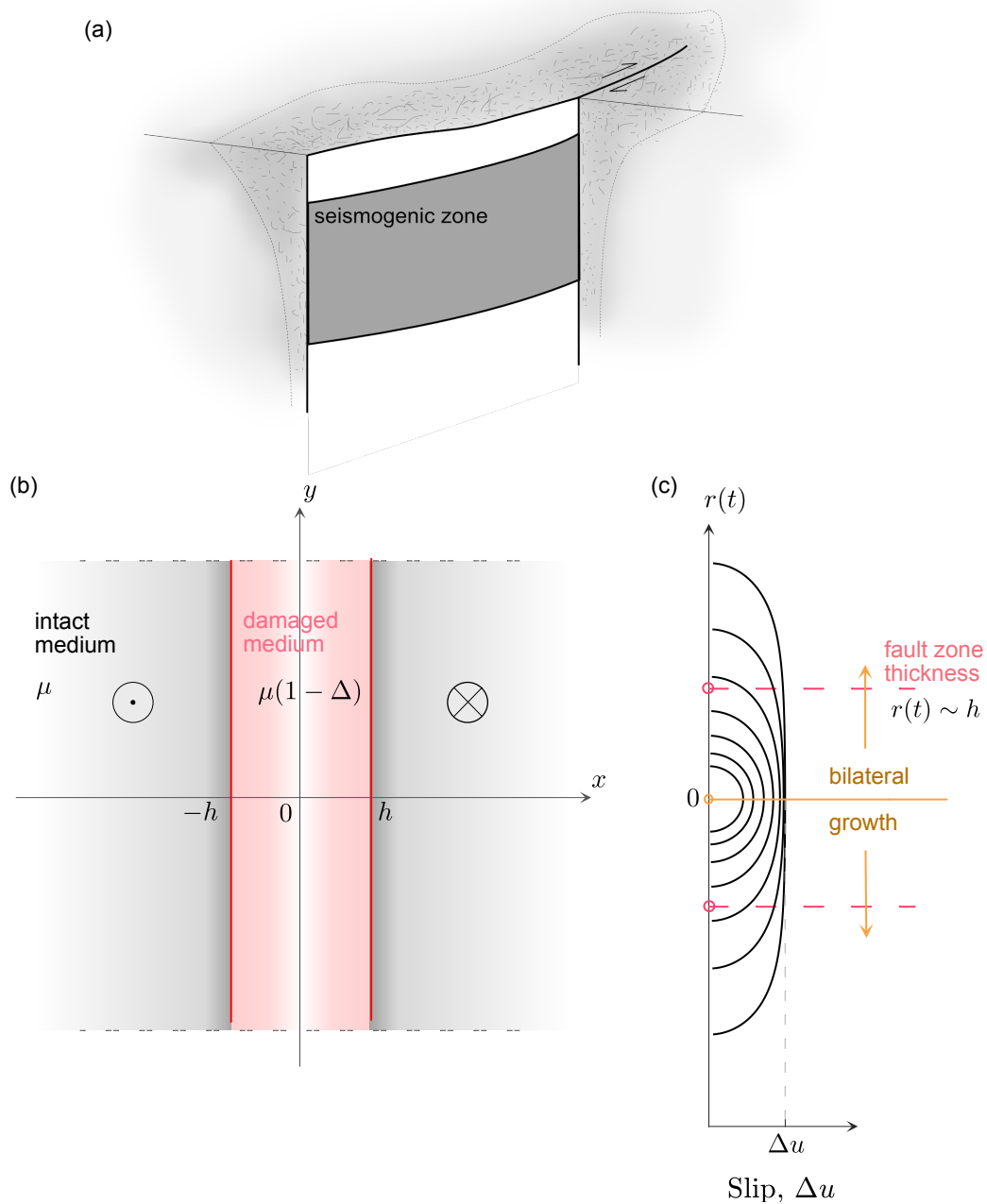
Figure 5.1: (a) Schematic representation of a fault zone. (b) Conceptualization of a fault zone as a simple tabular Low Velocity Fault Zone (LVFZ) model. The damaged and intact media have constant shear modulus, $(1 − \Delta)\mu$ and μ, respectively. (c) Quasi-static rupture growth with uniform stress drop in a LVFZ, showing a transition from crack-like (elliptical) to pulse-like (flat) slip profiles when the rupture length exceeds the LVFZ thickness. The static slip profiles are computed numerically for $\Delta = 0.99$ by the method described in Appendix J.

promote slip arrest (Huang and Ampuero, 2011; Thakur et al., 2020). However, LVFZ quasi-dynamic simulations do not include these reflected waves. Here, we explain how pulses can be promoted in LVFZs by a quasi-static mechanism.

The present work is further motivated by recent evidence of complex rupture patterns in earthquakes and tectonic tremors, in particular back-propagating fronts. While the inherent complexity of large earthquakes is abundantly highlighted by modern seismological observations (Meng et al., 2012; Ross et al., 2019), reports of secondary rupture fronts propagating in the direction opposite to the main front (i.e., towards the hypocenter) are becoming increasingly clear and robust (Beroza and Spudich, 1988; Hicks et al., 2020; Meng et al., 2011; Uchide et al., 2013; Vallée et al., 2020). Back-propagating fronts have also been identified during slow slip events (SSE) in Cascadia and Japan, appearing as tremor swarms known as Rapid Tremor Reversals (RTR) which migrate at fast speed in the direction opposite to the propagation of the large-scale slow slip (Houston et al., 2011).

Here, we show that pulses can be generated by a highly-damaged LVFZ, even without the dynamic effects of reflected waves. We follow two complementary approaches: static rupture scaling arguments (Section 2) and quasi-dynamic earthquake cycle simulations (Section 3). Our simulations also reveal that the quasi-static effects of a highly-damaged LVFZ are sufficient to generate back-propagating fronts.

5.3 Scaling arguments for quasi-static pulse generation

We consider a simple, tabular LVFZ model defined by a finite fault of length L bisecting a homogeneous low-rigidity layer, the damage zone, embedded in an intact medium (Fig. 5.1). The LVFZ is specified by its half-thickness h and its damage level Δ defined by:

$$\mu_d = (1 - \Delta)\mu, \tag{5.1}$$

where μ_d and μ are the shear moduli of the LVFZ and intact medium, respectively. We consider anti-plane deformation.

The model converges to two different homogeneous end-member models, depending on the fault zone thickness. When h/L is very small, the model approaches a homogeneous intact medium with shear modulus μ. When h/L is very large, the model tends to a homogeneous damaged medium with shear modulus $(1 - \Delta)\mu$.

Key effects of a LVFZ on rupture propagation are highlighted by analyzing the limiting case of a highly damaged fault zone ($\Delta \rightarrow 1$), which is asymptotically equivalent to the case of a rigid medium surrounding an elastic fault zone considered

by (Horowitz and Ruina, 1989). We consider a rupture growing quasi-statically with prescribed uniform stress drop $\Delta\tau$ and increasing rupture half-length $r(t)$. The fault-zone thickness h is fixed and, for illustrative purposes, we set $\Delta = 0.99$. The resulting slip profiles (Fig. 5.1c) are computed by solving numerically a static problem in which we account for static stress interactions modified by the presence of the damaged layer, as described in Appendix J. The shape of the slip profile is indicative of the style of rupture: crack-like ruptures show an elliptical slip profile whereas (steady-state) pulses have a flat slip profile (Gabriel et al., 2012). While the rupture is small ($r(t) \ll h$), it only interacts with the damaged zone and therefore has a crack-like slip profile, as in a uniformly damaged infinite medium. Its slip grows proportional to rupture length as $\Delta u(t) \sim \frac{\Delta\tau}{2\mu(1-\Delta)} r(t)$. As the rupture grows large ($r(t) \gg h$), it interacts with a thin elastic slab of thickness h and develops a pulse-like slip profile. Its slip reaches a value independent of rupture length, $\Delta u \sim \frac{\Delta\tau}{\mu(1-\Delta)} h$, as expected in a thin slab problem. Connecting these two rupture stages together, a growing rupture with constant stress drop in a highly-damaged LVFZ will initiate as a crack-like rupture and later transition into a pulse. The transition is characterized by saturation of slip caused by the LVFZ once the rupture grows larger than $2h$.

The above picture of crack-to-pulse transition provides insight into what controls rise-time in a damaged fault zone in the absence of wave reflection effects. The rise-time at the hypocenter is the time required for the appearance of a healing front. This time corresponds kinematically to the emergence of pulses, which is approximately the time required for the size of the initial crack to grow up to $r(t) = h$. Assuming a constant rupture speed v_r, the size of the rupture is $r(t) \sim v_r t$, hence the rise time at the hypocenter roughly follows

$$t \sim \frac{h}{v_r}. \tag{5.2}$$

This estimation of rise-time is valid at other locations beyond the hypocenter assuming that the propagation speed of the healing front is close to the rupture speed. Because rise-time can be shorter away from the hypocenter (Huang and Ampuero, 2011), Eq. (5.2) should be taken as an upper bound. The resulting upper bound for the pulse width, defined as the distance between the position of the rupture front and the healing front, is

$$l \sim v_r t \sim h. \tag{5.3}$$

The foregoing simplified analysis predicts the emergence of pulses from static effects alone, independently of the presence of reflected waves in the LVFZ.
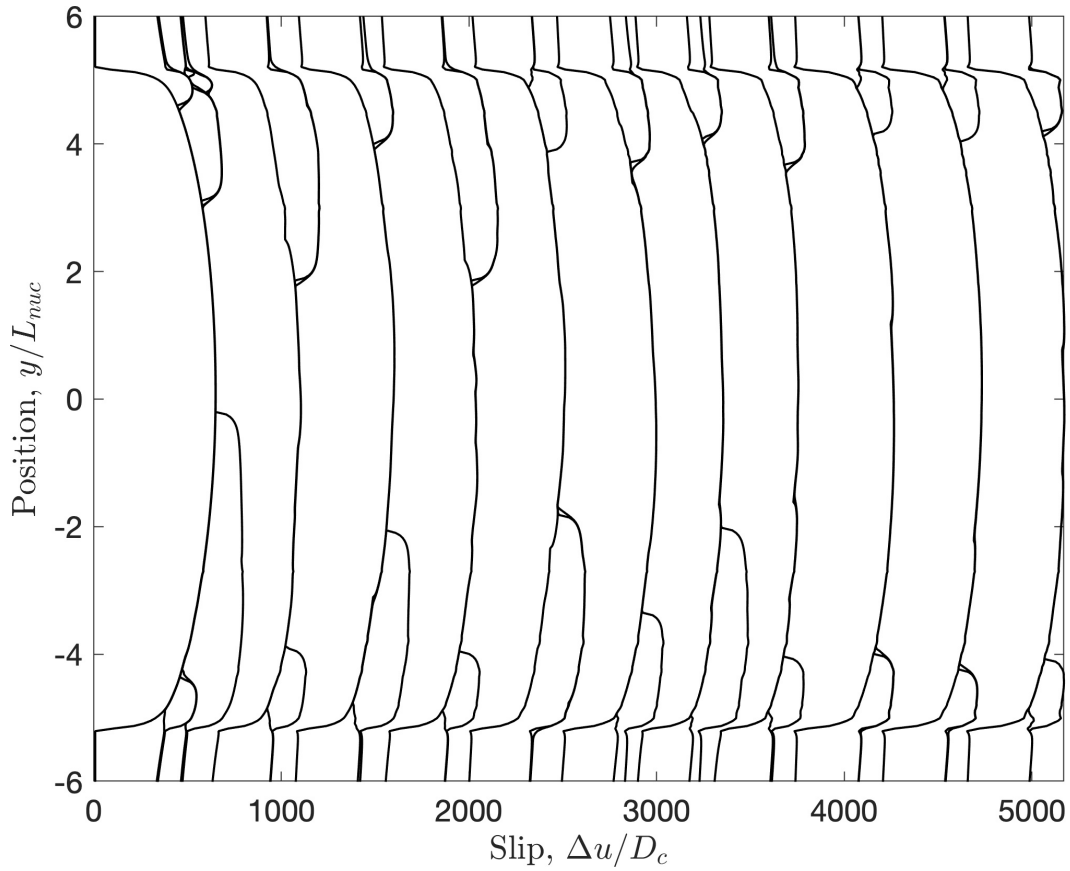
Figure 5.2: History of seismic activity in a simulation of a fault model with $\Delta = 0.9$ and $2h \approx 1/40L_{vw}$. Solid lines represent accumulated slip after an earthquake occurs.

5.4 Pulses and back-propagating fronts in quasi-dynamic multi-cycle models

We conduct quasi-dynamic earthquake cycle simulations under rate-and-state friction (Appendix I for methods), covering a wide range of values of LVFZ thickness and damage. Our simulations do not include dynamical effects from reflected waves. Each simulation produces a history of seismic activity, including earthquakes with multiple sizes (Fig. 5.2). The largest earthquakes in one simulation span the whole seismogenic length L_{vw} (Fig. I.1) and are labeled as characteristic events. In a given fault model, characteristic events have the same magnitude but may show different rupture patterns. We define an earthquake cycle as the period between two characteristic events. In some fault models, simulations show a variable duration of the earthquake cycle. We only consider results in characteristic events after a spin-up period of several initial cycles, avoiding a dependence of our results on the arbitrarily-prescribed initial conditions.
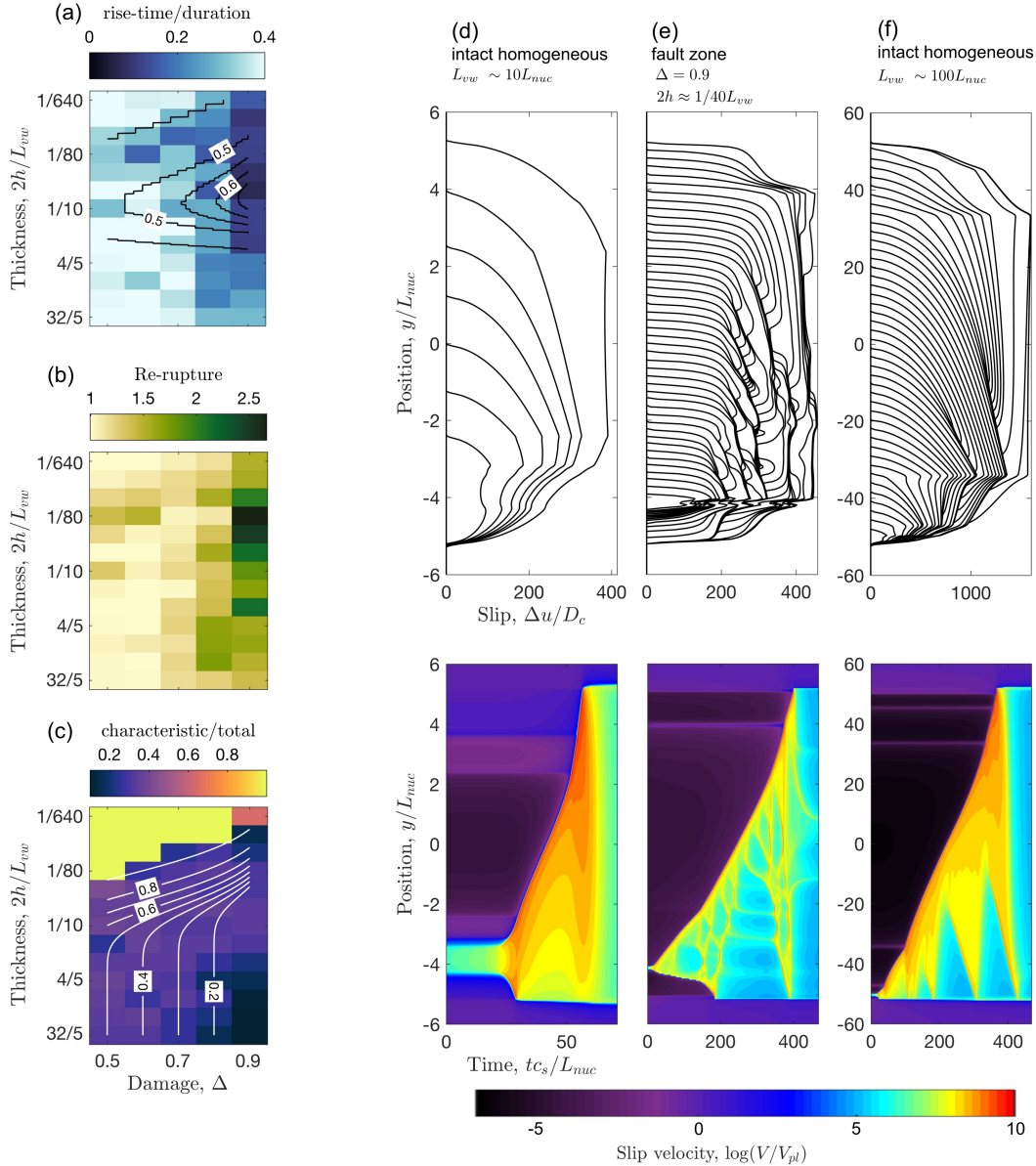
Figure 5.3: Ruptures and seismicity in fault-zone models after multiple earthquake cycles. (a) Average rise-time normalized by the total rupture duration, (b) average number of rupture fronts ($V > 1$ cm/s) during an event, and (c) number of characteristic events over the total number of events as a function of damage level Δ and fault-zone thickness $2h$ normalized by the size of the velocity-weakening fault segment L_{vw}. The rise-time is the duration of slip rate exceeding 1 cm/s. Black contours in (a) are a semi-analytical prediction of the flatness of the slip profile in a constant stress drop model (Appendix J). The slip profiles are obtained with the same method used in Fig. 5.1c. Flatness is the fraction of the fault length where slip is roughly constant, at most 20% lower than the maximum slip in the slip profile. White contours in (c) show the estimated reduction of the nucleation length due to the LVFZ (contours of L_{nuc} in LVFZ normalized by its value in a homogeneous intact medium). (d) Spatiotemporal evolution of slip and slip velocity in the characteristic event of an intact homogeneous medium, (e) a LVFZ with $\Delta = 0.9$ and $2h \approx L_{vw}/40$, and (f) an intact homogeneous medium with ten times smaller nucleation length than (d).

Complex slip patterns appear in characteristic events when damage is high ($\Delta > 0.7$) and the fault zone is thin compared to the length of the seismogenic zone ($2h < L_{vw}$). Two signatures characterize the slip complexity: the promotion of pulses (Fig. 5.3a) and the re-rupture of previously healed fault segments during the same event (Fig. 5.3b,e).

Pulses are defined here by a drastic reduction of slip rate ($V < 1$ cm/s) at a short distance behind the rupture front, leading to a short rise-time. We observe a systematic reduction of the average rise-time over a wide range of LVFZ thickness and high damage values (Fig. 5.3a). Short rise-times occur roughly within the range of LVFZ parameters that produce flat slip profiles in the static rupture models computed in Section 2 (Fig. 5.3a), consistent with the kinematic implications we drew from the static crack analysis.

The re-rupture of previously healed fault segments (Fig. 5.3b) is characterized by the emergence of secondary fronts propagating in the opposite direction to the main rupture front (Fig. 5.3e and Fig. 5.4). These back-propagating fronts have a short rise-time and can re-rupture multiple times the same fault segment. Models with seismogenic zones that are much larger than the nucleation size ($L_{vw} \gg L_{nuc}$; Appendix I) promote back-propagating fronts without requiring a LVFZ, but their rise-time is longer and their number of re-ruptures is small (Fig. 5.3f with $L_{vw} \sim 100L_{nuc}$).

In addition to characteristic events with complex slip patterns, events comprising a wide range of sizes develop in thick and highly damaged fault zones (Fig. 5.3c), where small events partially break the seismogenic zone from the edges (Fig. 5.2). Small, non-characteristic events are known to emerge in rate-and-state friction models in homogeneous media with seismogenic zones much larger than their nucleation length L_{nuc} (Barbot, 2019; Cattania, 2019). The nucleation length is the smallest size of a slip patch that can accelerate to instability (Rubin and Ampuero, 2005). In a homogeneous medium it is proportional to the shear modulus, and in a damaged zone to a reduced, effective shear modulus that depends on h and Δ (Appendix I). The LVFZ thickness and damage values promoting variable event magnitudes in our models are well explained by the increase in the L_{vw}/L_{nuc} ratio due to the reduction in L_{nuc} induced by the LVFZ (Fig. 5.3c). The smallest nucleation length is achieved in models with $\Delta = 0.9$ and $2h > L_{vw}$, which have $L_{vw} \sim 100L_{nuc}$.

The rupture speed in our homogeneous medium model (Fig. 5.3d) corresponds to $V_{rup} \sim 1$ km/s, a typical value in seismological observations. In contrast, a highly-
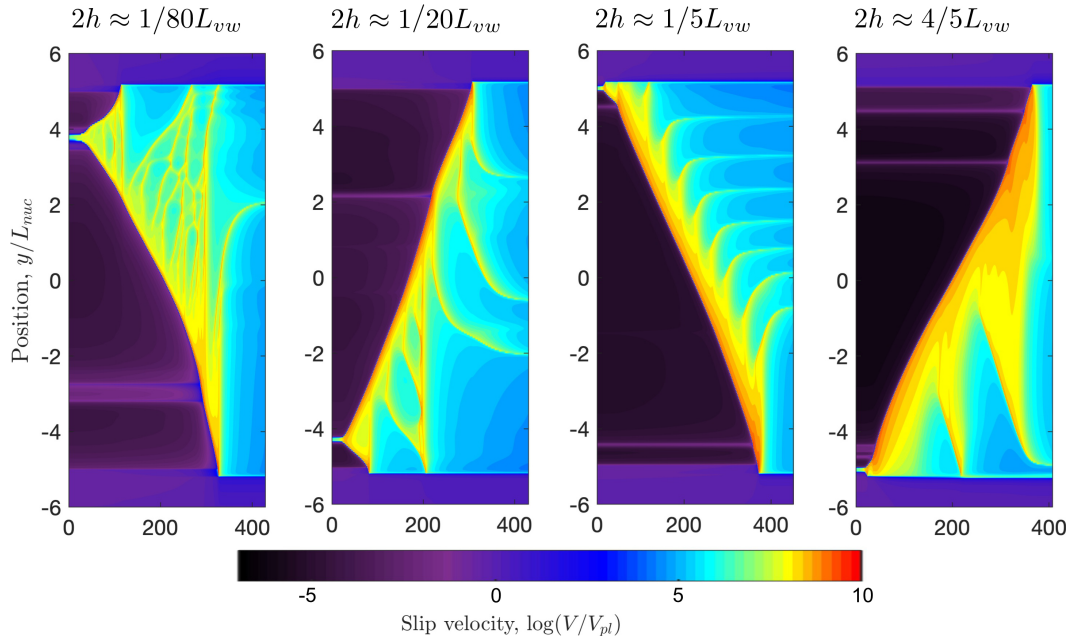
Figure 5.4: Spatiotemporal evolution of slip rate in the characteristic event of earthquake cycle models using a LVFZ with $\Delta = 0.9$ and different values of damage zone thickness.

Table 5.1: Approximated dimensions of a fault and properties of the rupture in the homogeneous and LVFZ models shown in Fig. 5.5 after assuming a value for D_c.

	Homogeneous	LVFZ ($\Delta = 0.9$)
Characteristic slip, D_c	2 mm	2 mm
Seismogenic zone, L_{vw}	2.5 km	2.5 km
Nucleation length, L_{nuc} and L_{nuc}^*	242 m	40 m
Fault-zone thickness, $2h$	-	64 m
Event duration, t	2.4 sec	32.4 sec
Average rise-time	2.1 sec	5.6 sec

damaged fault zone promotes a reduction in the rupture speed $V_{rup}^d/V_{rup} \propto (1 - \Delta)$, compatible with theoretical quasi-static predictions of rupture speed (Ampuero and Rubin, 2008) but slower than most seismological observations. The non-dimensional units in Fig. 5.3 can be converted into real scales depending on the assumed value of the characteristic slip distance of rate-and-state friction, D_c; examples of dimensional scales are given in Table 5.1 for $D_c = 2$ mm.
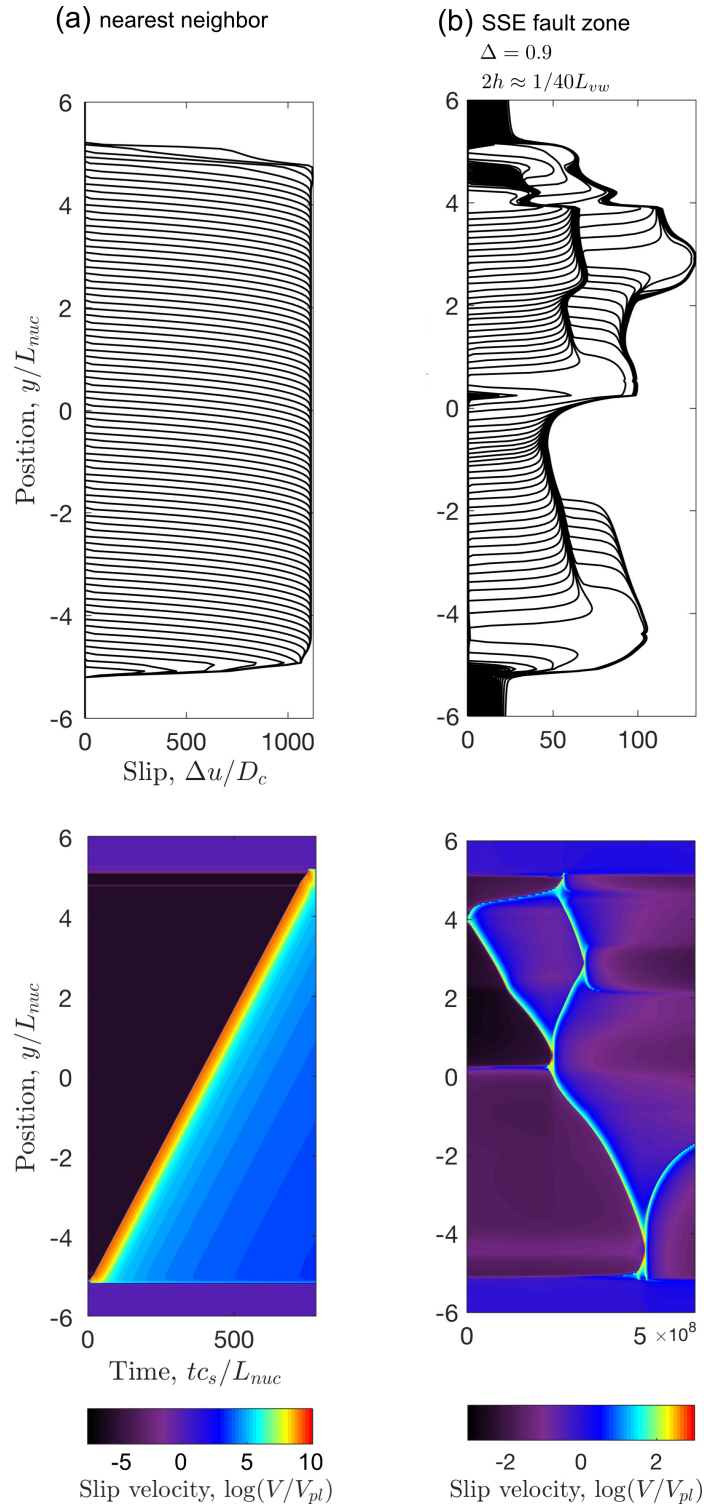
Figure 5.5: Spatiotemporal evolution of slip and slip rate in the characteristic event of earthquake cycle models assuming (a) a nearest-neighbor model with $\Delta = 0.99$ and $2h = L_{vw}/25$ and (b) a slow-slip model in a LVFZ model with $\Delta = 0.9$ and $2h \approx L_{vw}/40$ and a modified friction law with velocity-strengthening at high velocities. Axes are normalized following the convention in Fig. 5.3.

Table 5.2: Parameters used in the numerical simulations.

Parameter	Symbol	Value
Direct effect (VW/VS)	a	0.014/0.043
Evolution effect (VW/VS)	b	0.019/0.019
Characteristic slip	D_c	2 mm
Tectonic loading	V_{pl}	10^{-9} m/s
Reference slip rate	V_0	10^{-9} m/s
Reference friction coefficient	μ_0	0.6
Shear-wave speed	β	3.5 km/s
Intact shear modulus	μ	30 GPa
Effective normal stress	σ	120 MPa

5.5 Discussion

Short-range stress transfer and the origin of pulses in a LVFZ

Models with nearest-neighbour stress transfer, such as the Burridge-Knopoff (BK) model (Burridge and Knopoff, 1967), have been often used as a mechanical analog to earthquake rupture and are capable of promoting pulses in the continuum limit (Brener et al., 2018; Erickson et al., 2011). In a BK model, a chain of sliders connected by springs is loaded by a uniform displacement applied to a loading spring (Burridge and Knopoff, 1967). In a uniform stress drop rupture, the BK model produces the flat static slip profile characteristic of pulses when the loading stiffness is much higher than the static stress transfer due to the relative motion of sliders (Appendix K). Under our current model parameters (Table 5.2), ruptures propagate as pulses both in a nearest-neighbour model (Fig. 5.5a) and in a fault-zone model with large damage, $\Delta = 0.9$ (Fig. 5.3e). Here we show that the emergence of pulses in a LVFZ can be related to stress interactions approaching the nearest-neighbour regime across a wide range of slip wavelengths.

The static stress transfer in a fault-zone model due to spatially-harmonic slip with wavelength k and unit amplitude is (Appendix J, Fig. J.1)

$$\mathcal{K}(k) = \frac{1}{2}\mu(1 - \Delta)|k| \coth\left(h|k| + \operatorname{atanh}(1 - \Delta)\right). \tag{5.4}$$

Asymptotic analysis (Fig. 5.6a, Appendix K) shows that at low k the stress transfer in a LVFZ tends to that of an intact homogeneous medium, whereas at high k it tends to that of a damaged homogeneous medium. In an intermediate range of wavelengths, the stress transfer is approximately nearest-neighbour. As Δ increases, the relative bandwidth of the nearest-neighbour regime broadens (Fig. S8), and the short rise-time observed in the nearest-neighbor model (Fig. 5.5a) appears in the
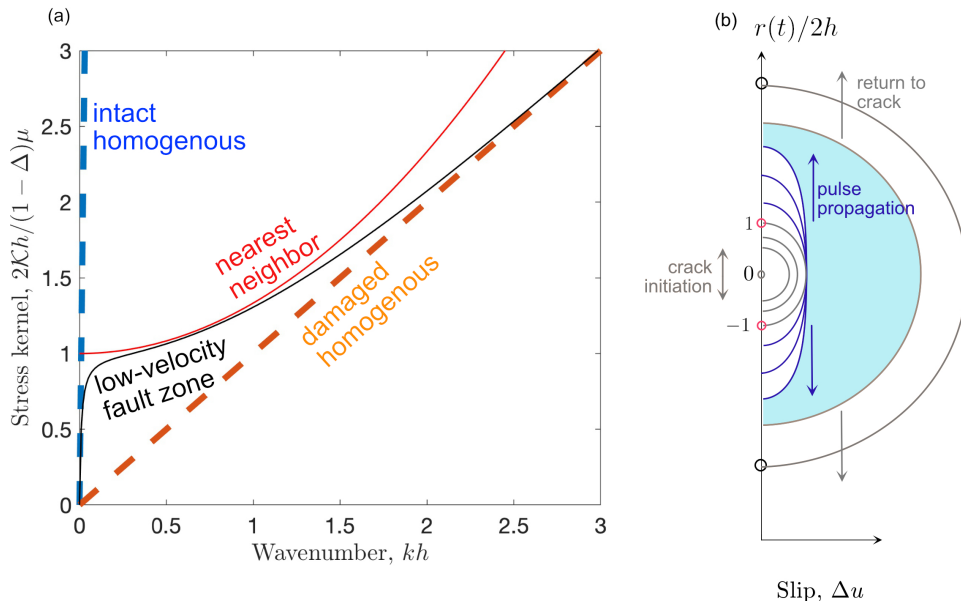
Figure 5.6: Nearest-neighbor stress transfer and promotion of slip complexity. (a) The static stress transfer kernel of a LVFZ (Eq. 5.4) with $\Delta = 0.99$ (black) in Fourier domain, as a function of the normalized wavenumber kh of slip, and its nearest-neighbor approximation (red) (Appendix K). Also shown are the asymptotic limits of a homogeneous intact medium (blue dashed) ($\mathcal{K} = \mu|k|/2$) and homogeneous damaged medium (orange dashed) ($\mathcal{K} = \mu_d|k|/2$). The exaggerated level of damage $\Delta = 0.99$ represents the asymptotic limit of a LVFZ as damage increases. (b) Conceptual interpretation of the emergence of secondary pulses. Re-rupturing is necessary to fill the slip deficit (cyan) between a pulse at intermediate rupture length ($r(t) > 2h$, purple curves) and a crack appearing at much larger lengths ($r(t) \gg 2h$, gray curves).

LVFZ model as well. In other words, increasing the LVFZ damage level extends the range of slip length scales where pulses can exist. When h is small ($h \ll \sqrt{3}L_{vw}$), a LVFZ model within the nearest-neighbour regime produces uniform stress drop ruptures with a slip profile that is flat and has an average slip $\approx 2h\Delta\tau/(1-\Delta)\mu$ (Appendix K).

The limiting case where $\Delta \to 1$, analyzed in Section 2, represents an elastic layer of thickness $2h$ bounded by an infinitely rigid medium (Horowitz and Ruina, 1989). Stress interactions in that case are nearest-neighbour at wavelengths larger than ~$2\pi h$ (Fig. S8). Such model is completely nearest-neighbour if the process zone size, the smallest characteristic length scale of slip, is larger than ~$2\pi h$.

Origin of back-propagating fronts

Highlighted in our work as a manifestation of rupture complexity, back-propagating fronts owe part of their relevance to recent earthquake observations. A recent report from a M7.1 oceanic transform earthquake features a "boomerang earthquake" slip pattern (Hicks et al., 2020) that resembles the structure of back-propagating fronts shown in our models. Seismic observations indicate that LVFZs extend throughout the seismogenic zone in oceanic transform faults (Roland et al., 2012), enhancing the relevance of our model to explain the "boomerang earthquake" slip pattern. In a different tectonic setting, a back-propagating front appears during a recently reported M8 intermediate-depth earthquake (Vallée et al., 2020). Both observations are independently supported by teleseismic back-projection imaging and finite source inversion, suggesting the ubiquity of back-propagating fronts to different tectonic environments.

The static solutions introduced in Section 2 provide insight on the origin of multiple back-propagating fronts. Relying on an idealized situation where the only deformable medium is within the LVFZ, we showed the emergence of a transition from a crack into a pulse when the rupture size exceeds $2h$. In reality the medium outside the LVFZ is deformable as well. As the rupture continues growing to sizes much larger than $2h$, stress increasingly transfers through the outer medium. Eventually, the influence of the LVFZ becomes irrelevant to the propagation of the rupture. At this point, the static analysis predicts a second, reverse transition from pulse-like behavior to the crack-like behavior of an intact homogeneous medium (Fig. 5.6b). Beyond this transition, slip increases in regions that were previously healed. Therefore, slip reactivation is required there, leading to secondary rupture fronts.

We expect re-ruptures to initiate where stresses are the highest, which is near the primary rupture front, thus the ensuing secondary rupture fronts have to propagate backwards. Furthermore, because these secondary ruptures start small, they need to go through a pulse-like phase. In summary, in the presence of a LVFZ, back-propagating pulses are necessary to complete the slip budget of a very large rupture, filling the slip gap between intermediate-size pulses and large-size cracks.

A mechanism for Rapid Tremor Reversals

While observations of back-propagating fronts during earthquakes are challenging and still incipient, slow slip and tremor phenomena offer a unique and systematic

opportunity to observe complex slip patterns in slow motion. The back-propagating fronts identified in Fig. 5.3e suggest that a highly-compliant LVFZ can provide a mechanism for Rapid Tremor Reversals (RTRs) observed in Cascadia and Japan during slow-slip events (Houston et al., 2011). Seismological observations suggest that subduction megathrusts are surrounded by low-velocity zones (Audet and Schaeffer, 2018; Nedimović et al., 2003) that are several kilometers thick near the region where tremor activity concentrates (Calvert et al., 2020). Instead of damaged rock, low-velocity zones in subduction zones mostly relate to layers of subducted material containing pressurized fluids. Previous models of RTR rely on frictional heterogeneities (Luo and Ampuero, 2017; Luo and Liu, 2019), pore fluid pressure waves (Cruz-Atienza et al., 2018), or external transient forcings such as tides (Hawthorne and Rubin, 2013a). Our models show RTR-like patterns emerging from a different mechanism: the quasi-static stress transfer of a LVFZ. Due to the ubiquity of LVFZ to both regular earthquakes and slow slip events, our model supports the idea that detailed observations of slow slip phenomena contribute to understand earthquakes in general (Michel et al., 2019).

Our simulations show that back-propagating fronts also occur in slow slip models with a LVFZ (Fig. 5.5b). Introducing strengthening at high slip rate is a known approach to model slow-slip events (Hawthorne and Rubin, 2013b). We added a linear velocity-strengthening term into the friction law (i.e., the fault strengthens proportionally to V), which is stronger than the logarithmic strengthening term of the conventional rate-and-state friction (Appendix I). We chose a velocity-strengthening coefficient 10^6 times larger than the radiation damping coefficient. Our results indicate that back-propagating fronts emerge during slow-slip events in a LVFZ model with the modified friction, although they are less vigorous than those observed in our fast-rupture results (Fig. 5.5). Slow-slip events only show pulse-like behavior and back-propagating fronts in the presence of a LVFZ (Fig. 5.7). As slow-slip models are insensitive to dynamical effects, our results confirm that back-propagating fronts emerge from quasi-static LVFZ effects alone. The SSE propagation speed in our model is ~5 m/day, about 1000 times lower than SSE propagation speeds observed in Cascadia, which range from 7 to 15 km/day (Houston et al., 2011). Further work is required to examine how low-velocity zones quantitatively affect tremor migration patterns in more detailed slow-slip models.

The damage level observed in strike-slip faults ranges from 0.45 to 0.85 and the fault zone thickness from 80 to 1500 m, with typical values $\Delta \sim 0.65$ and $2h \sim 200$ m
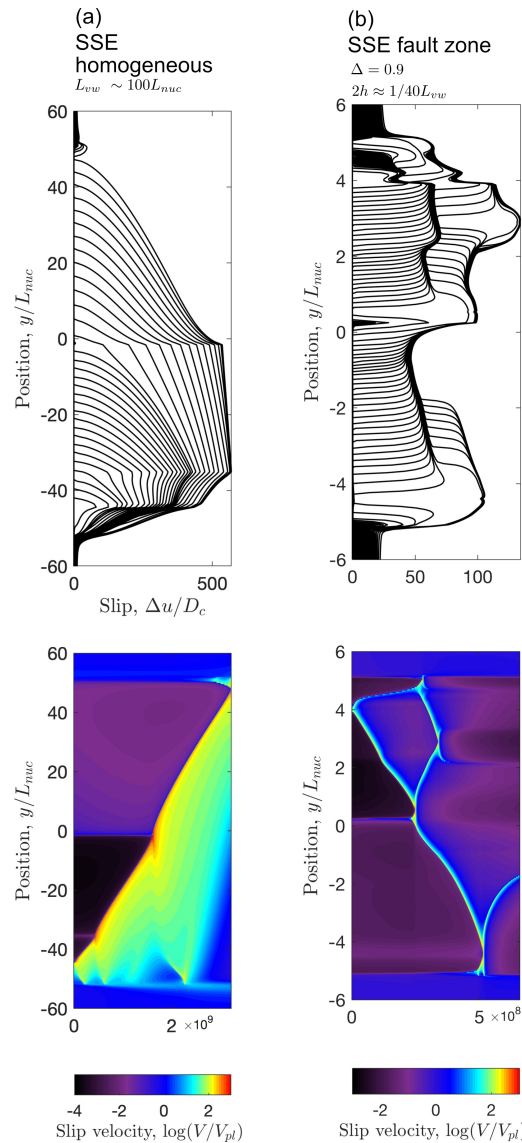
Figure 5.7: Comparison of slow-slip earthquakes (SSE) with and without a fault zone (LVFZ) modeled using a friction law of increased velocity-strengthening. (a) A slow earthquake in a fully-damaged homogeneous medium. The slip profiles are indicative of crack-like rupture propagation. (b) The addition of the LVFZ promotes multiple back-propagating secondary fronts. The main and secondary fronts show slip profiles indicative of pulse-like rupture propagation.

(Fig. 5.8). The most damaged fault-zone structures reach $\Delta \sim 0.85$ (Li et al., 2007; Yang and Zhu, 2010), which is close to the minimum value required by our model to show significant slip complexity (Fig. 5.3a,b). For $\Delta \sim 0.85$ and a reasonable fault-zone thickness $2h$ from 100 m to 1 km, the rupture length required to develop pulses and back-propagating fronts must be larger than 2 to 20 km (Fig. 5.3a,b).
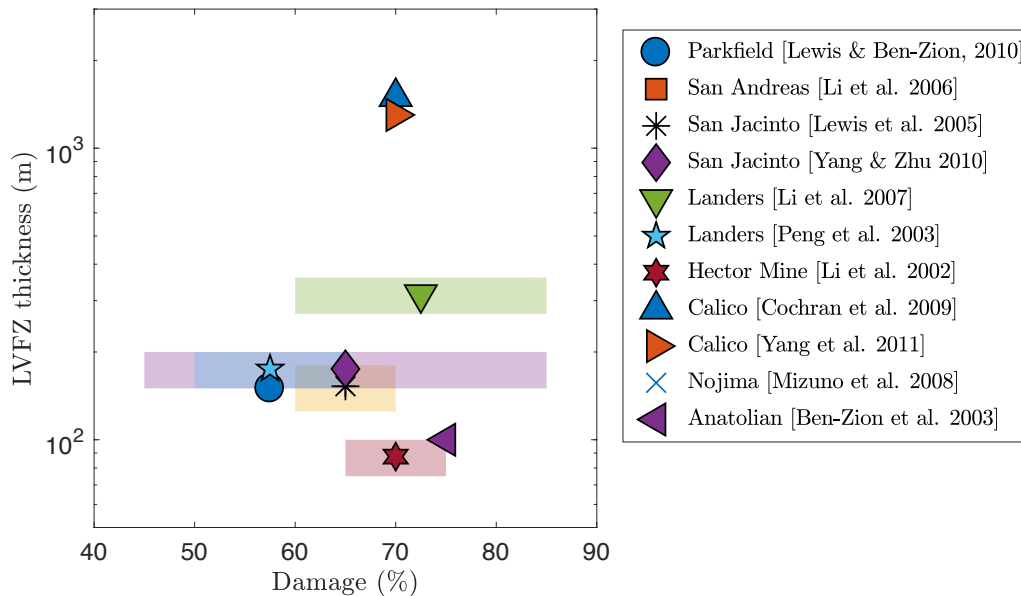
Figure 5.8: A compilation of fault-zone properties included in Huang et al. (2014). Damage represents a reduction in shear moduli, which relates to a reduction in velocity as $\Delta_\mu = 1 - (1 - \Delta_v)^2$, where Δ_μ is the damage reported in the figure and Δ_v the reduction in velocity reported in Huang et al. (2014).

It is likely then that the quasi-static LVFZ effects described here do not operate during very small slow slip events. The properties of fault zones where RTRs are observed are harder to be resolved compared to crustal faults due to the larger depths involved. Dimensions of fault zones in subduction environments have been inferred from observations in exhumed subduction zones (Rowe et al., 2013) but their elastic properties remain poorly constrained. Receiver functions suggest that the v_p/v_s ratio may increase over ~75% due to over-pressurization of fluids within the several-km-thick low-velocity zone that surrounds regions where tremors are generated (Audet and Schaeffer, 2018; Calvert et al., 2020).

Potential model limitations

Further research is warranted to investigate whether the effects observed in our idealized fault zone model remain after releasing some of the simplifying assumptions, in particular the quasi-dynamic approximation and the 2D tabular LVFZ geometry.

Quasi-dynamic simulations in the absence of a LVFZ qualitatively agree with fully-dynamic simulations under a conventional Dieterich-Ruina friction law (Thomas et al., 2014). However, dynamic simulations that include a LVFZ produce a range of

fault zone waves, including reflected, trapped and head waves (Huang and Ampuero, 2011; Huang et al., 2014), which can perturb the dynamic stress on the fault and interfere with the quasi-static mechanism highlighted in the present work. Preliminary results suggest that dynamic effects modulate, but do not obliterate the quasi-static effects reported here (Flores-Cuba et al., 2020). Similarly, in previous dynamic single-rupture simulations (Huang et al., 2014) dynamic LVFZ wave effects modulate, but do not obliterate the generation of pulses by another mechanism, enhanced velocity-weakening friction. An important open question is whether the dynamic effects of fault zone waves allow the slip complexity revealed here to operate over a broader range of LVFZ property values, including the lower, commonly observed levels of fault-zone damage.

The direction of slip is not important in the context of our quasi-dynamic model. Our anti-plane results can be transferred to in-plane slip by replacing μ with $\mu/(1 - \nu)$, where ν is Poisson's ratio. However, in-plane dynamical models can promote additional slip complexity, for instance transitions to super-shear rupture speed which are relevant for the interpretation of past earthquakes (Huang et al., 2016; Oral et al., 2020).

The 3D structure of damage zones observed in the field is more complicated than a simple 2D tabular region, usually displaying flower structures with wider thickness at shallower depth (Finzi et al., 2009; Mitchell and Faulkner, 2009; Savage and Brodsky, 2011). Moreover, LVFZ properties are not uniform along strike as the fault-zone thickness varies with along-strike changes in fault geometry and the total amount of slip locally accumulated over time (Ampuero and Mao, 2017; Mitchell and Faulkner, 2009; Perrin et al., 2016). How such systematic variations of LVFZ properties affect the rupture features highlighted here warrants further study. We expect that the promotion by LVFZ of pulses and back-propagating fronts reported in our 2D simulations should also appear in 3D simulations, as the static transfer mechanism is approximately the same (similar to Eq. 5.4 with k replaced by the modulus of the wavenumber vector).

The quasi-static pulse-generation mechanism revealed here should persist in a LVFZ without the sharp elasticity contrasts of a simple tabular damage zone, in contrast to the dynamic mechanism of pulse-generation by reflected waves (Huang et al., 2014). In fact, the static stress transfer in a model with exponential decay of damage as a function of distance from the fault (Ampuero et al., 2002) has the same essential features as in our tabular model (Eq. 5.4), in particular the same asymptotic behaviors

highlighted in Fig. 5.6.

5.6   Conclusions

Our analytical arguments and simulation results show that rupture pulses emerge and persist across multiple earthquake cycles via quasi-static effects in a fault surrounded by a highly-damaged fault zone, independently of the dynamic effects induced by fault-zone-reflected waves. We develop a formal analogy between a fault zone model and a nearest-neighbor (Burridge-Knopoff) model that explains the emergence of pulses. Nearest-neighbor models are known to produce pulses and, within a certain range of length scales, the stress transfer in a damaged fault zone is approximately nearest-neighbor. Our results suggest that the earthquake rise-time should be proportional to fault zone thickness divided by rupture speed in highly-damaged faults.

We also showed that fault-zone effects can produce complex slip patterns, including back-propagating fronts that re-rupture previously healed fault segments. Such back-propagating fronts have been most recently observed in large earthquakes. The back-propagating fronts in our slow-slip models with highly-damaged fault zones are also analogous to rapid tremor reversals observed in Cascadia and Japan.

Overall, quasi-static fault-zone effects provide a simple mechanism to promote and sustain earthquake complexity, and a mechanical link between structural fault properties and seismicity. Our results further motivate the quest for higher temporal and spatial resolution in earthquake source studies. The systematic exploration of model parameters contained in our results provide targets for laboratory experiments aimed at understanding the interactions between rupture propagation and heterogeneous media.

Chapter 6

SUMMARY OF CONCLUSIONS

In this thesis, I developed a new framework to explore the interior structure of Jupiter based on tidal gravity measurements obtained by NASA's Juno spacecraft (Fig. 6.1). My goal required further developing of the theory of dynamical tides applied to the amplitude of the tidal gravitational field of Jupiter. I divided this complex task into three smaller and simpler projects. In each of these projects, my approach involved using simple models and perturbation theory to extract meaningful results and physical insight from the complicated equations that describe tides in a gas giant planet.
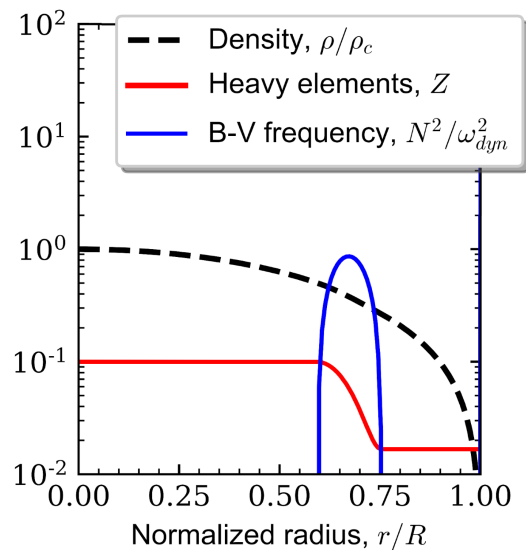
Figure 6.1: A diluted core model for Jupiter. This model satisfies Juno's zonal gravity constraints up to J_6 and tidal gravity k_2 and k_{42}.

In Chapter II, I revealed how the Coriolis effect associated to Jupiter's rotation introduces a -4% change in the tidal amplitude k_2 at the tidal frequency of Io. To the current date, this effect is enough to reconcile k_2 Juno observations with models. In fact, the present k_2 measurement is noninformative of core structure given the current observational error (Fig. 6.2). As Juno continues collecting data, future reductions in the observational error may require developing further detailed modeling or theory to fully explain the observed k_2.
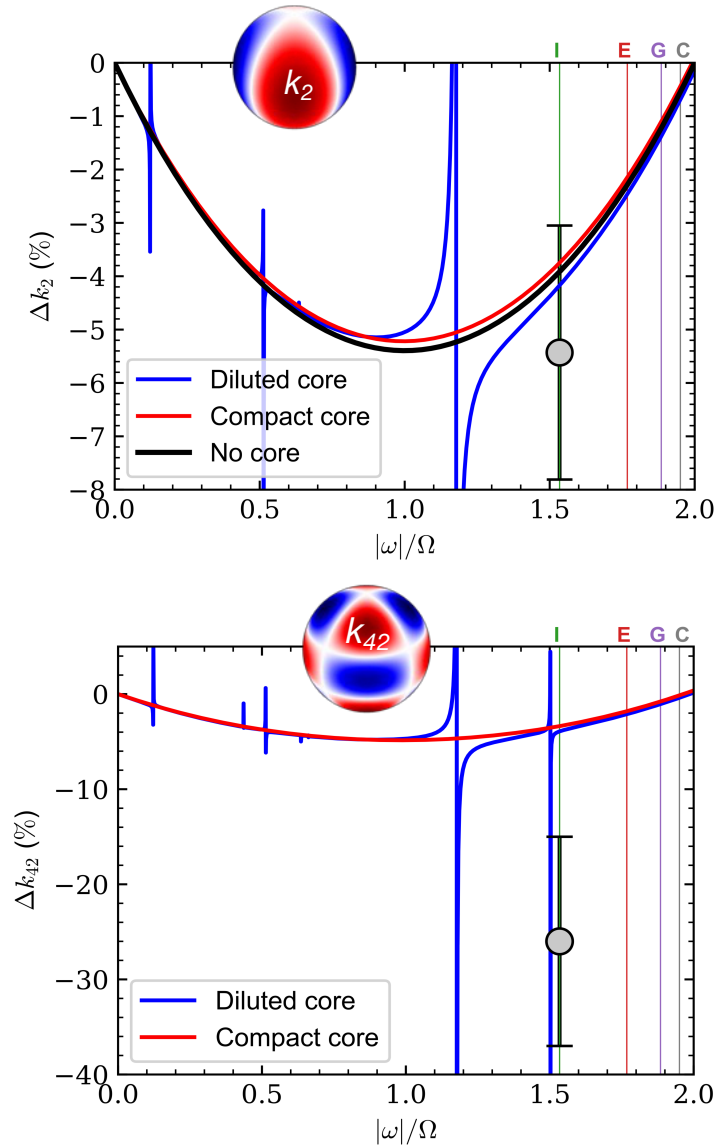
Figure 6.2: Gravitational imprint of dynamical tides as a function of tidal frequency. The fractional corrections Δk_2 and Δk_{42} represent a percentile change in the Love number of Jupiter's equilibrium tide. The diluted core is shown in Fig 6.1. The gray circle is the Juno observation with 3σ error bars at perijove 17 (mid-mission). Vertical lines are the tidal frequency of the satellites I: Io, E: Europa, C: Callisto, and G: Ganymede.

In Chapter III, I illuminated the gyrotidal effect that enhances Jupiter's tidal response in the high-order Love number k_{42}. Jupiter develops a significant oblate figure due to the centrifugal effect, resulting in Jupiter's equatorial radius being 6% larger than the polar radius. This oblate shape couples the tidal response at different scales, causing an order of magnitude increase in k_{42}. This fully analytical study provided

physical insight into a result that in the past was only accessible via numerical modeling.

In Chapter IV, I integrated lessons learned in the previous two chapters to propose a scenario that explains a 7σ anomaly in the high-order tidal gravity field of Jupiter k_{42}. In this proposed scenario, Jupiter's diluted core is shrinking over geological timescales while its oscillation frequency remains synchronized to the orbital frequency of the satellite Io. The result is a tidal resonance that introduces a high-order dynamical tide observable by Juno (Fig. 6.2). The most likely resonant scenario involves Jupiter's diluted core extending as far as ~70% of the radius (Fig. 6.1). Less extended diluted cores could also cause a similar resonance but such configuration becomes less likely due to the weaker tidal coupling associated with the resonant normal mode. Important uncertanties in this proposed scenario invite new theoretical studies and independent observational confirmations of the proposed Jupiter-Io tidal resonance. Independent observational evidence can be gathered at the end of the Juno mission by means of observing the satellite dependent k_{42} and from ground-based astronomy via Doppler seismology targeted at detecting a Jupiter normal mode with oscillation frequency ~270 μHz.

The new framework I developed here can in principle be used to study other giant planets if precise gravity measurements from an orbiting spacecraft are available. However, an important limitation is that tidal gravity is only sensitive to planetary interior structure when the satellite tidal forcing is close to a resonance with a planetary normal mode (Fig. 6.2). In that sense, tidal gravity constitutes a complement to the traditional zonal gravity analysis. Given the sensitivity of dynamical tides to tidal resonances, tidal gravity can be of particular interest to detect deeply settled compositional gradients in giant planets. The next opportunity to apply this tidal gravity analysis to a giant planet will be the Uranus Orbiter and Probe mission, a mission concept recently recommended in the 2023–2032 Planetary Science Decadal Survey as first priority for the next NASA Flagship-class mission.

In Chapter V, I revealed a new mechanism to promote pulse-like rupture and back-propagating rupture fronts based on quasi-static stress transfer. Earthquakes are dynamical processes whose study requires detailed numerical approaches that exceed the complexity of the convenient quasi-dynamic approximation used in this chapter. An immediate research question is whether the quasi-static effects identified here remain relevant when competing with overlapping dynamical effects.

6.1 Future research opportunities in giant planet's interiors

The following are questions related to the new paradigm of diluted cores in gas giant planets that remain open:

- What is the origin of diluted cores (i.e., formation versus evolution)? Current ideas suggest that the diluted core could emerge as a result of core erosion or via the particular order in which planetary materials are put into place at the time of formation.

- What influence do diluted cores have on gas giant planet tidal dissipation? A dilute core implies a change in how tidal energy is dissipated inside the planet. The tidal excitation of internal waves trapped in the diluted core influences the amount of angular momentum that is transferred from the planet into the orbiting satellites, with implications to the current structure of circumplanetary systems.

- Is Jupiter's diluted core qualitatively different from Saturn's?

- Can we resolve smaller-scale dilute core structure? The planetary scale structure of the diluted core models considered in this thesis may represent an over simplification of a finer structure where thinner regions of stratification alternate with regions of convection.

- Where do we locate the dynamo region? Dynamos most likely require the existence of a convective region to allocate the flow of a semi-conductor material. Whereas that region is shallow (i.e., top of the diluted core) or deep (within the diluted core) is an active topic of research.

- How is the planet cooling down and where is the heat coming from? The diluted core promotes stratification, countering the traditional view of Jupiter as a fully adiabatic and convective interior. Vertical heat transfer without overturning convection is inefficient, thus naturally raising questions about the origin of the planet's luminosity.

Bibliography

Aagaard, B. T. and Heaton, T. (2008). Constraining fault constitutive behavior with slip and stress heterogeneity. *Journal of Geophysical Research: Solid Earth*, 113(B4).

Aerts, C., Christensen-Dalsgaard, J., and Kurtz, D. W. (2010). *Asteroseismology*. Springer Science & Business Media.

Ampuero, J. P. and Mao, X. (2017). Upper limit on damage zone thickness controlled by seismogenic depth. *Fault Zone Dynamic Processes: Evolution of Fault Properties During Seismic Rupture*, 227:243.

Ampuero, J.-P. and Rubin, A. M. (2008). Earthquake nucleation on rate and state faults–aging and slip laws. *Journal of Geophysical Research: Solid Earth*, 113(B1).

Ampuero, J.-P., Vilotte, J.-P., and Sanchez-Sesma, F. (2002). Nucleation of rupture under slip dependent friction law: simple models of fault zone. *Journal of Geophysical Research: Solid Earth*, 107(B12).

Audet, P. and Schaeffer, A. J. (2018). Fluid pressure and shear zone development over the locked to slow slip region in cascadia. *Science advances*, 4(3):eaar2982.

Barbot, S. (2019). Slow-slip, slow earthquakes, period-two cycles, full and partial ruptures, and deterministic chaos in a single asperity fault. *Tectonophysics*, 768:228171.

Batygin, K., Bodenheimer, P., and Laughlin, G. (2009). Determination of the interior structure of transiting planets in multiple-planet systems. *The Astrophysical Journal Letters*, 704(1):L49.

Ben-Zion, Y., Peng, Z., Okaya, D., Seeber, L., Armbruster, J. G., Ozer, N., Michael, A. J., Baris, S., and Aktar, M. (2003). A shallow fault-zone structure illuminated by trapped waves in the Karadere–Duzce branch of the North Anatolian Fault, western Turkey. *Geophysical Journal International*, 152(3):699–717.

Beroza, G. C. and Mikumo, T. (1996). Short slip duration in dynamic rupture in the presence of heterogeneous fault properties. *Journal of Geophysical Research: Solid Earth*, 101(B10):22449–22460.

Beroza, G. C. and Spudich, P. (1988). Linearized inversion for fault rupture behavior: Application to the 1984 morgan hill, california, earthquake. *Journal of Geophysical Research: Solid Earth*, 93(B6):6275–6296.

Bodenheimer, P., Stevenson, D. J., Lissauer, J. J., and D'Angelo, G. (2018). New formation models for the kepler-36 system. *The Astrophysical Journal*, 868(2):138.

Bolton, S. J., Adriani, A., Adumitroaie, V., Allison, M., Anderson, J., Atreya, S., Bloxham, J., Brown, S., Connerney, J., DeJong, E., et al. (2017). Jupiter's interior and deep atmosphere: The initial pole-to-pole passes with the juno spacecraft. *Science*, 356(6340):821–825.

Boyd, J. P. (2001). *Chebyshev and Fourier spectral methods*. Courier Corporation.

Brener, E. A., Aldam, M., Barras, F., Molinari, J.-F., and Bouchbinder, E. (2018). Unstable slip pulses and earthquake nucleation as a nonequilibrium first-order phase transition. *Physical review letters*, 121(23):234302.

Burridge, R. and Knopoff, L. (1967). Model and theoretical seismicity. *Bulletin of the seismological society of america*, 57(3):341–371.

Calvert, A. J., Bostock, M. G., Savard, G., and Unsworth, M. J. (2020). Cascadia low frequency earthquakes at the base of an overpressured subduction shear zone. *Nature Communications*, 11(1):1–10.

Cattania, C. (2019). Complex earthquake sequences on simple faults. *Geophysical Research Letters*.

Chachan, Y. and Stevenson, D. J. (2019). A linear approximation for the effect of cylindrical differential rotation on gravitational moments: Application to the non-unique interpretation of saturn's gravity. *Icarus*, 323:87–98.

Chester, F. and Logan, J. M. (1986). Implications for mechanical properties of brittle faults from observations of the punchbowl fault zone, california. *Pure and applied geophysics*, 124(1-2):79–106.

Christensen-Dalsgaard, J., Gough, D., and Toomre, J. (1985). Seismology of the sun. *Science*, 229(4717):923–931.

Cochard, A. and Madariaga, R. (1996). Complexity of seismicity due to highly rate-dependent friction. *Journal of Geophysical Research: Solid Earth*, 101(B11):25321–25336.

Cochard, A. and Rice, J. R. (1997). A spectral method for numerical elastodynamic fracture analysis without spatial replication of the rupture event. *Journal of the Mechanics and Physics of Solids*, 45(8):1393–1418.

Cochran, E. S., Li, Y.-G., Shearer, P. M., Barbot, S., Fialko, Y., and Vidale, J. E. (2009). Seismic and geodetic evidence for extensive, long-lived fault damage zones. *Geology*, 37(4):315–318.

Connerney, J., Timmins, S., Oliversen, R., Espley, J., Joergensen, J., Kotsiaros, S., Joergensen, P., Merayo, J., Herceg, M., Bloxham, J., et al. (2022). A new model of jupiter's magnetic field at the completion of juno's prime mission. *Journal of Geophysical Research: Planets*, 127(2):e2021JE007055.

Cruz-Atienza, V. M., Villafuerte, C., and Bhat, H. S. (2018). Rapid tremor migration and pore-pressure waves in subduction zones. *Nature communications*, 9(1):1–13.

Dahlen, F. and Tromp, J. (1998). *Theoretical global seismology*. Princeton university press.

Day, S. M. (1982). Three-dimensional finite difference simulation of fault dynamics: rectangular faults with fixed rupture velocity. *Bulletin of the Seismological Society of America*, 72(3):705–727.

Day, S. M., Yu, G., and Wald, D. J. (1998). Dynamic stress changes during earthquake rupture. *Bulletin of the Seismological Society of America*, 88(2):512–522.

Debras, F. and Chabrier, G. (2019). New models of jupiter in the context of juno and galileo. *The Astrophysical Journal*, 872(1):100.

Dewberry, J. W. and Lai, D. (2022). Dynamical tidal love numbers of rapidly rotating planets and stars. *The Astrophysical Journal*, 925(2):124.

Dieterich, J. H. (1981). Constitutive properties of faults with simulated gouge. *Mechanical behavior of crustal rocks: the Handin volume*, 24:103–120.

Durante, D., Parisi, M., Serra, D., Zannoni, M., Notaro, V., Racioppa, P., Buccino, D., Lari, G., Gomez Casajus, L., Iess, L., et al. (2020). Jupiter's gravity field halfway through the juno mission. *Geophysical Research Letters*, 47(4):e2019GL086572.

Erickson, B. A., Birnir, B., and Lavallée, D. (2011). Periodicity, chaos and localization in a burridge–knopoff model of an earthquake with rate-and-state friction. *Geophysical Journal International*, 187(1):178–198.

Finzi, Y., Hearn, E. H., Ben-Zion, Y., and Lyakhovsky, V. (2009). Structural properties and deformation patterns of evolving strike-slip faults: Numerical simulations incorporating damage rheology. *Pure and Applied Geophysics*, 166(10-11):1537–1573.

Flores-Cuba, J. M., Ampuero, J.-P., Oral, E., and Idini, B. (2020). Fault damage zones enhance earthquake rupture complexity over multiple cycles.

Fuller, J. (2014). Saturn ring seismology: Evidence for stable stratification in the deep interior of saturn. *Icarus*, 242:283–296.

Fuller, J., Luan, J., and Quataert, E. (2016). Resonance locking as the source of rapid tidal migration in the jupiter and saturn moon systems. *Monthly Notices of the Royal Astronomical Society*, 458(4):3867–3879.

Gabriel, A.-A., Ampuero, J.-P., Dalguer, L. A., and Mai, P. M. (2012). The transition of dynamic rupture styles in elastic media under velocity-weakening friction. *Journal of Geophysical Research: Solid Earth*, 117(B9).

Gaulme, P., Schmider, F.-X., Gay, J., Guillot, T., and Jacob, C. (2011). Detection of jovian seismic waves: a new probe of its interior structure. *Astronomy & Astrophysics*, 531:A104.

Gavrilov, S. and Zharkov, V. (1977). Love numbers of the giant planets. *Icarus*, 32(4):443–449.

Goodman, J. and Lackner, C. (2009). Dynamical tides in rotating planets and stars. *The Astrophysical Journal*, 696(2):2054.

Greenspan, H. P. et al. (1968). *The theory of rotating fluids*. CUP Archive.

Guillot, T. (2005). The interiors of giant planets: Models and outstanding questions. *Annu. Rev. Earth Planet. Sci.*, 33:493–530.

Hansen, C. J., Kawaler, S. D., and Trimble, V. (2012). *Stellar interiors: physical principles, structure, and evolution*. Springer Science & Business Media.

Harris, R. A. and Day, S. M. (1997). Effects of a low-velocity zone on a dynamic rupture. *Bulletin of the Seismological Society of America*, 87(5):1267–1280.

Hawthorne, J. and Rubin, A. (2013a). Tidal modulation and back-propagating fronts in slow slip events simulated with a velocity-weakening to velocity-strengthening friction law. *Journal of Geophysical Research: Solid Earth*, 118(3):1216–1239.

Hawthorne, J. and Rubin, A. M. (2013b). Laterally propagating slow slip events in a rate and state friction model with a velocity-weakening to velocity-strengthening transition. *Journal of Geophysical Research: Solid Earth*, 118(7):3785–3808.

Heaton, T. H. (1990). Evidence for and implications of self-healing pulses of slip in earthquake rupture. *Physics of the Earth and Planetary Interiors*, 64(1):1–20.

Helled, R. and Stevenson, D. (2017). The fuzziness of giant planets' cores. *The Astrophysical Journal Letters*, 840(1):L4.

Helled, R., Stevenson, D. J., Lunine, J. I., Bolton, S. J., Nettelmann, N., Atreya, S., Guillot, T., Militzer, B., Miguel, Y., and Hubbard, W. B. (2022). Revelations on jupiter's formation, evolution and interior: Challenges from juno results. *Icarus*, page 114937.

Hicks, S. P., Okuwaki, R., Steinberg, A., Rychert, C. A., Harmon, N., Abercrombie, R. E., Bogiatzis, P., Schlaphorst, D., Zahradnik, J., Kendall, J.-M., et al. (2020). Back-propagating supershear rupture in the 2016 m w 7.1 romanche transform fault earthquake. *Nature Geoscience*, pages 1–7.

Horowitz, F. G. and Ruina, A. (1989). Slip patterns in a spatially homogeneous fault model. *Journal of Geophysical Research: Solid Earth*, 94(B8):10279–10298.

Houston, H., Delbridge, B. G., Wech, A. G., and Creager, K. C. (2011). Rapid tremor reversals in Cascadia generated by a weakened plate interface. *Nature Geoscience*, 4(6):404.

Huang, Y. and Ampuero, J.-P. (2011). Pulse-like ruptures induced by low-velocity fault zones. *Journal of Geophysical Research: Solid Earth*, 116(B12).

Huang, Y., Ampuero, J.-P., and Helmberger, D. V. (2014). Earthquake ruptures modulated by waves in damaged fault zones. *Journal of Geophysical Research: Solid Earth*, 119(4):3133–3154.

Huang, Y., Ampuero, J.-P., and Helmberger, D. V. (2016). The potential for super-shear earthquakes in damaged fault zones–theory and observations. *Earth and Planetary Science Letters*, 433:109–115.

Hubbard, W. B. (1984). *Planetary interiors*. Van Nostrand Reinhold.

Hubbard, W. B. and Marley, M. S. (1989). Optimized jupiter, saturn, and uranus interior models. *Icarus*, 78(1):102–118.

Idini, B. and Ampuero, J.-P. (2017). Rupture complexity promoted by damaged fault zones in earthquake cycle models.

Idini, B. and Stevenson, D. J. (2021). Dynamical tides in jupiter as revealed by juno. *The Planetary Science Journal*, 2(2):69.

Iess, L., Folkner, W., Durante, D., Parisi, M., Kaspi, Y., Galanti, E., Guillot, T., Hubbard, W. B., Stevenson, D., Anderson, J., et al. (2018). Measurement of jupiter's asymmetric gravity field. *Nature*, 555(7695):220–222.

Iess, L., Jacobson, R. A., Ducci, M., Stevenson, D. J., Lunine, J. I., Armstrong, J. W., Asmar, S. W., Racioppa, P., Rappaport, N. J., and Tortora, P. (2012). The tides of titan. *Science*, 337(6093):457–459.

Johnson, E. (1990). On the initiation of unidirectional slip. *Geophysical Journal International*, 101(1):125–132.

Kaneko, Y., Ampuero, J.-P., and Lapusta, N. (2011). Spectral-element simulations of long-term fault slip: Effect of low-rigidity layers on earthquake-cycle dynamics. *Journal of Geophysical Research: Solid Earth*, 116(B10).

Kulowski, L., Cao, H., and Bloxham, J. (2020). Contributions to jupiter's gravity field from dynamics in the dynamo region. *Journal of Geophysical Research: Planets*, 125(5):e2019JE006165.

Lai, D. (2021). Jupiter's dynamical love number. *The Planetary Science Journal*, 2(4):122.

Lainey, V., Arlot, J.-E., Karatekin, Ö., and Van Hoolst, T. (2009). Strong tidal dissipation in io and jupiter from astrometric observations. *Nature*, 459(7249):957–959.

Lainey, V., Casajus, L. G., Fuller, J., Zannoni, M., Tortora, P., Cooper, N., Murray, C., Modenini, D., Park, R. S., Robert, V., et al. (2020). Resonance locking in giant planets indicated by the rapid orbital expansion of titan. *Nature Astronomy*, pages 1–6.

Lainey, V., Jacobson, R. A., Tajeddine, R., Cooper, N. J., Murray, C., Robert, V., Tobie, G., Guillot, T., Mathis, S., Remus, F., et al. (2017). New constraints on saturn's interior from cassini astrometric data. *Icarus*, 281:286–296.

Lewis, M., Peng, Z., Ben-Zion, Y., and Vernon, F. (2005). Shallow seismic trapping structure in the san jacinto fault zone near anza, california. *Geophysical Journal International*, 162(3):867–881.

Lewis, M. A. and Ben-Zion, Y. (2010). Diversity of fault zone damage and trapping structures in the Parkfield section of the San Andreas Fault from comprehensive analysis of near fault seismograms. *Geophysical Journal International*, 183(3):1579–1595.

Li, H., Zhu, L., and Yang, H. (2007). High-resolution structures of the Landers fault zone inferred from aftershock waveform data. *Geophysical Journal International*, 171(3):1295–1307.

Li, Y.-G., Chen, P., Cochran, E. S., Vidale, J. E., and Burdette, T. (2006). Seismic evidence for rock damage and healing on the san andreas fault associated with the 2004 m 6.0 parkfield earthquake. *Bulletin of the Seismological Society of America*, 96(4B):S349–S363.

Li, Y.-G., Leary, P., Aki, K., and Malin, P. (1990). Seismic trapped modes in the oroville and san andreas fault zones. *Science*, 249(4970):763–766.

Li, Y.-G., Vidale, J. E., Day, S. M., and Oglesby, D. D. (2002). Study of the 1999 M 7.1 Hector Mine, California, earthquake fault plane by trapped waves. *Bulletin of the Seismological Society of America*, 92(4):1318–1332.

Liu, S.-F., Hori, Y., Müller, S., Zheng, X., Helled, R., Lin, D., and Isella, A. (2019). The formation of jupiter's diluted core by a giant impact. *Nature*, 572(7769):355–357.

Lockitch, K. H. and Friedman, J. L. (1999). Where are the r-modes of isentropic stars? *The Astrophysical Journal*, 521(2):764.

Love, A. E. H. (1909). The yielding of the earth to disturbing forces. *Proceedings of the Royal Society of London. Series A, Containing Papers of a Mathematical and Physical Character*, 82(551):73–88.

Luo, Y. and Ampuero, J.-P. (2017). Tremor migration patterns and the collective behavior of deep asperities mediated by creep.

Luo, Y., Ampuero, J.-P., Galvez, P., van den Ende, M., and Idini, B. (2017). QDYN: a Quasi-DYNamic earthquake simulator (v1.1). Zenodo. doi:10.5281/zenodo.322459.

Luo, Y. and Liu, Z. (2019). Rate-and-state model casts new insight into episodic tremor and slow-slip variability in cascadia. *Geophysical Research Letters*.

Mankovich, C. and Fuller, J. (2021). A diffuse core in saturn revealed by ring seismology. *arXiv preprint arXiv:2104.13385*.

Mankovich, C., Marley, M. S., Fortney, J. J., and Movshovitz, N. (2019). Cassini ring seismology as a probe of saturn's interior. i. rigid rotation. *The Astrophysical Journal*, 871(1):1.

Mankovich, C. R. (2020). Saturn's rings as a seismograph to probe saturn's internal structure. *AGU Advances*, 1(2):e2019AV000142.

Markham, S., Durante, D., Iess, L., and Stevenson, D. (2020). Possible evidence of p-modes in cassini measurements of saturn's gravity field. *The Planetary Science Journal*, 1(2):27.

Marley, M. S. and Porco, C. C. (1993). Planetary acoustic mode seismology: Saturn's rings. *Icarus*, 106(2):508–524.

Meng, L., Ampuero, J., Page, M., and Hudnut, K. (2011). Seismological evidence and dynamic model of reverse rupture propagation during the 2010 m7. 2 el mayor cucapah earthquake. In *AGU Fall Meeting Abstracts*.

Meng, L., Ampuero, J.-P., Stock, J., Duputel, Z., Luo, Y., and Tsai, V. (2012). Earthquake in a maze: Compressional rupture branching during the 2012 mw 8.6 sumatra earthquake. *Science*, 337(6095):724–726.

Michel, S., Gualandi, A., and Avouac, J.-P. (2019). Similar scaling laws for earthquakes and cascadia slow-slip events. *Nature*, 574(7779):522–526.

Miguel, Y., Bazot, M., Guillot, T., Howard, S., Galanti, E., Kaspi, Y., Hubbard, W., Militzer, B., Helled, R., Atreya, S., et al. (2022). Jupiter's inhomogeneous envelope. *arXiv preprint arXiv:2203.01866*.

Mitchell, T. and Faulkner, D. (2009). The nature and origin of off-fault damage surrounding strike-slip fault zones with a wide range of displacements: A field study from the Atacama fault system, northern Chile. *Journal of Structural Geology*, 31(8):802–816.

Mizuno, H. (1980). Formation of the giant planets. *Progress of Theoretical Physics*, 64(2):544–557.

Mizuno, H., Nakazawa, K., and Hayashi, C. (1978). Instability of a gaseous envelope surrounding a planetary core and formation of giant planets. *Progress of Theoretical Physics*, 60(3):699–710.

Mizuno, T., Kuwahara, Y., Ito, H., and Nishigami, K. (2008). Spatial variations in fault-zone structure along the nojima fault, central japan, as inferred from borehole observations of fault-zone trapped waves. *Bulletin of the Seismological Society of America*, 98(2):558–570.

Müller, S., Helled, R., and Cumming, A. (2020). The challenge of forming a fuzzy core in jupiter. *arXiv preprint arXiv:2004.13534*.

Munk, W. H. and MacDonald, G. J. (1960). The rotation of the earth; a geophysical discussion. *regd*.

Murray, C. D. and Dermott, S. F. (1999). *Solar system dynamics*. Cambridge university press.

Nedimović, M. R., Hyndman, R. D., Ramachandran, K., and Spence, G. D. (2003). Reflection signature of seismic and aseismic slip on the northern cascadia subduction interface. *Nature*, 424(6947):416.

Nielsen, S. and Madariaga, R. (2003). On the self-healing fracture mode. *Bulletin of the Seismological Society of America*, 93(6):2375–2388.

Noda, H., Dunham, E. M., and Rice, J. R. (2009). Earthquake ruptures with thermal weakening and the operation of major faults at low overall stress levels. *Journal of Geophysical Research: Solid Earth*, 114(B7).

Notaro, V., Durante, D., and Iess, L. (2019). On the determination of jupiter's satellite-dependent love numbers from juno gravity data. *Planetary and Space Science*, 175:34–40.

Ogilvie, G. I. (2009). Tidal dissipation in rotating fluid bodies: a simplified model. *Monthly Notices of the Royal Astronomical Society*, 396(2):794–806.

Ogilvie, G. I. and Lin, D. (2004a). Tidal dissipation in rotating giant planets. *The Astrophysical Journal*, 610(1):477.

Ogilvie, G. I. and Lin, D. (2004b). Tidal dissipation in rotating giant planets. *The Astrophysical Journal*, 610(1):477.

Ojakangas, G. W. and Stevenson, D. (1986). Episodic volcanism of tidally heated satellites with application to io. *Icarus*, 66(2):341–358.

Oral, E., Weng, H., and Ampuero, J. P. (2020). Does a damaged-fault zone mitigate the near-field impact of supershear earthquakes?—application to the 2018 7.5 palu, indonesia, earthquake. *Geophysical Research Letters*, 47(1):e2019GL085649.

Peng, Z., Ben-Zion, Y., Michael, A. J., and Zhu, L. (2003). Quantitative analysis of seismic fault zone waves in the rupture zone of the 1992 landers, california, earthquake: evidence for a shallow trapping structure. *Geophysical Journal International*, 155(3):1021–1041.

Perri, F. and Cameron, A. G. (1974). Hydrodynamic instability of the solar nebula in the presence of a planetary core. *Icarus*, 22(4):416–425.

Perrin, C., Manighetti, I., Ampuero, J.-P., Cappa, F., and Gaudemer, Y. (2016). Location of largest earthquake slip and fast rupture controlled by along-strike change in fault structural maturity due to fault growth. *Journal of Geophysical Research: Solid Earth*, 121(5):3666–3685.

Perrin, G., Rice, J. R., and Zheng, G. (1995). Self-healing slip pulse on a frictional surface. *Journal of the Mechanics and Physics of Solids*, 43(9):1461–1495.

Pollack, J. B., Hubickyj, O., Bodenheimer, P., Lissauer, J. J., Podolak, M., and Greenzweig, Y. (1996). Formation of the giant planets by concurrent accretion of solids and gas. *icarus*, 124(1):62–85.

Rice, J. R. (1993). Spatio-temporal complexity of slip on a fault. *Journal of Geophysical Research: Solid Earth*, 98(B6):9885–9907.

Roland, E., Lizarralde, D., McGuire, J. J., and Collins, J. A. (2012). Seismic velocity constraints on the material properties that control earthquake behavior at the quebrada-discovery-gofar transform faults, east pacific rise. *Journal of Geophysical Research: Solid Earth*, 117(B11).

Ross, Z. E., Idini, B., Jia, Z., Stephenson, O. L., Zhong, M., Wang, X., Zhan, Z., Simons, M., Fielding, E. J., Yun, S.-H., et al. (2019). Hierarchical interlocked orthogonal faulting in the 2019 ridgecrest earthquake sequence. *Science*, 366(6463):346–351.

Rowe, C. D., Moore, J. C., Remitti, F., and Scientists, I. E. T. (2013). The thickness of subduction plate boundary faults from the seafloor into the seismogenic zone. *Geology*, 41(9):991–994.

Rubin, A. and Ampuero, J.-P. (2005). Earthquake nucleation on (aging) rate and state faults. *J. Geophys. Res.-Sol. Ea.*, 110(B11).

Ruina, A. (1980). Friction laws and instabilities: a quasi-static analysis of some dry friction behaviour. *Ph. D. thesis, Division of Engineering, Brown University*.

Ruina, A. (1983). Slip instability and state variable friction laws. *J. Geophys. Res.-Sol. Ea.*, 88(B12):10359–10370.

Safranov, V. (1969). Evolution of the protoplanetary cloud and formation of the earth and planets. *NASA Tech. Transl. F-677; Moscow, Nauka*.

Savage, H. M. and Brodsky, E. E. (2011). Collateral damage: Evolution with displacement of fracture distribution and secondary fault strands in fault damage zones. *Journal of Geophysical Research: Solid Earth*, 116(B3).

Stevenson, D. and Salpeter, E. (1977). The dynamics and helium distribution in hydrogen-helium fluid planets. *The Astrophysical Journal Supplement Series*, 35:239–261.

Stevenson, D. J. (1982). Interiors of the giant planets. *Annual Review of Earth and Planetary Sciences*, 10(1):257–295.

Stevenson, D. J. (2020). Jupiter's interior as revealed by juno. *Annual Review of Earth and Planetary Sciences*, 48.

Storch, N. I. and Lai, D. (2014). Viscoelastic tidal dissipation in giant planets and formation of hot jupiters through high-eccentricity migration. *Monthly Notices of the Royal Astronomical Society*, 438(2):1526–1534.

Thakur, P., Huang, Y., and Kaneko, Y. (2020). Effects of low-velocity fault damage zones on long-term earthquake behaviors on mature strike-slip faults. *Journal of Geophysical Research: Solid Earth*, page e2020JB019587.

Thomas, M. Y., Lapusta, N., Noda, H., and Avouac, J.-P. (2014). Quasi-dynamic versus fully dynamic simulations of earthquakes and aseismic slip with and without enhanced coseismic weakening. *Journal of Geophysical Research: Solid Earth*, 119(3):1986–2004.

Townsend, R. and Teitler, S. (2013). Gyre: an open-source stellar oscillation code based on a new magnus multiple shooting scheme. *Monthly Notices of the Royal Astronomical Society*, 435(4):3406–3418.

Uchide, T., Yao, H., and Shearer, P. M. (2013). Spatio-temporal distribution of fault slip and high-frequency radiation of the 2010 el mayor-cucapah, mexico earthquake. *Journal of Geophysical Research: Solid Earth*, 118(4):1546–1555.

Vallée, M., Grandin, R., Nocquet, J.-M., Villegas, J.-C., Vaca, S., Xie, Y., Meng, L., Ampuero, J.-P., Mothes, P., and Jarrin, P. (2020). Rupture characteristics of the 2019 north peru intraslab earthquake (mw8. 0). In *EGU General Assembly Conference Abstracts*, page 10429.

Vazan, A., Helled, R., and Guillot, T. (2018). Jupiter's evolution with primordial composition gradients. *Astronomy & Astrophysics*, 610:L14.

Vorontsov, S., Gavrilov, S., Zharkov, V., and Leontev, V. (1984). Dynamical theory of the tides on the giant planets. *Astronomicheskii Vestnik*, 18:8–18.

Vorontsov, S., Zharkov, V., and Lubimov, V. (1976). The free oscillations of jupiter and saturn. *Icarus*, 27(1):109–118.

Wahl, S. M., Hubbard, W. B., and Militzer, B. (2016). Tidal response of preliminary jupiter model. *The Astrophysical Journal*, 831(1):14.

Wahl, S. M., Hubbard, W. B., and Militzer, B. (2017a). The concentric maclaurin spheroid method with tides and a rotational enhancement of saturn's tidal response. *Icarus*, 282:183–194.

Wahl, S. M., Hubbard, W. B., Militzer, B., Guillot, T., Miguel, Y., Movshovitz, N., Kaspi, Y., Helled, R., Reese, D., Galanti, E., et al. (2017b). Comparing jupiter interior structure models to juno gravity measurements and the role of a dilute core. *Geophysical Research Letters*, 44(10):4649–4659.

Wahl, S. M., Parisi, M., Folkner, W. M., Hubbard, W. B., and Militzer, B. (2020). Equilibrium tidal response of jupiter: Detectability by the juno spacecraft. *The Astrophysical Journal*, 891(1):42.

Wolfram, S. (1999). The mathematica book. *Assembly Automation*.

Wu, Y. (2005). Origin of tidal dissipation in jupiter. i. properties of inertial modes. *The Astrophysical Journal*, 635(1):674.

Yang, H. and Zhu, L. (2010). Shallow low-velocity zone of the San Jacinto fault from local earthquake waveform modelling. *Geophysical Journal International*, 183(1):421–432.

Yang, H., Zhu, L., and Cochran, E. S. (2011). Seismic structures of the calico fault zone inferred from local earthquake travel time modelling. *Geophysical Journal International*, 186(2):760–770.

A p p e n d i x   A

HYDROSTATIC TIDES IN AN INDEX-ONE POLYTROPE

In hydrostatic tides, the tidal frequency becomes $\omega \approx 0$, and the tidal flow is slow enough to set $\mathbf{v} \approx 0$. After projecting ϕ^0 into spherical harmonics by setting a solution in the form

$$\phi^0 = \sum_{\ell,m} \phi^0_{\ell,m}(x) Y^\ell_m(\theta, \varphi) e^{-i\omega t}, \tag{A.1}$$

the radial part of ϕ^0 at a given harmonic that satisfies equation (2.13) follows

$$\partial_{x,x} \phi^0_\ell + \frac{2}{x} \partial_x \phi^0_\ell + \left(1 - \frac{\ell(\ell+1)}{x^2}\right) \phi^0_\ell = -\left(\frac{x}{\pi}\right)^\ell, \tag{A.2}$$

where Y^m_ℓ are the normalized spherical harmonics defined by

$$Y^m_\ell(\theta, \varphi) = \sqrt{\frac{(2\ell+1)}{4\pi} \frac{(\ell-m)!}{(\ell+m)!}} \mathcal{P}^m_\ell(\cos\theta) e^{im\varphi}, \tag{A.3}$$

and $\mathcal{P}^m_\ell$ are the associated Legendre polynomials corresponding to

$$\mathcal{P}^m_\ell(\mu) = \frac{(-1)^m}{2^\ell l!} (1 - \mu^2)^{m/2} \frac{d^{\ell+m}}{d\mu^{\ell+m}} (\mu^2 - 1)^\ell. \tag{A.4}$$

The normalized radial coordinate follows $x = kr$, which leads to a planet with radius π. Note that equation (A.2) is non-dimensional and should be scaled by the factor

$$U_{\ell,m} = \left(\frac{\mathcal{G}m_s}{a}\right) \left(\frac{R_p}{a}\right)^\ell \left(\frac{4\pi(\ell-m)!}{(2\ell+1)(\ell+m)!}\right)^{1/2} \mathcal{P}^m_l(0). \tag{A.5}$$

The order m does not appear in equation (A.2), indicating a degeneracy on m of the hydrostatic tide. As $x^\ell Y^m_\ell$ is a solution to Laplace's equation (i.e., $\nabla^2(x^\ell Y^m_\ell) = 0$), a complete solution to equation (A.2) is

$$\phi^0_\ell = A j_\ell(x) + B n_\ell(x) - \left(\frac{x}{\pi}\right)^\ell. \tag{A.6}$$

We require ϕ^0 to be finite at the center of the planet and thus set $B = 0$. According to the outer boundary condition, we set a external gravitational potential $\Phi^0_\ell(x)$ that extends outward from the planet and matches the internal tidal potential at the planetary radius as

$$\Phi^0_\ell(x) = \left(\frac{\pi}{x}\right)^{\ell+1} \phi^0_\ell(\pi) = \left(\frac{\pi}{x}\right)^{\ell+1} (A_\ell j_\ell(\pi) - 1). \tag{A.7}$$

The continuity of the gradients of the internal and external potentials at the surface of the planet sets the constant A_ℓ to

$$A_\ell = \frac{2\ell + 1}{\pi j_{\ell-1}(\pi)}.$$ (A.8)

Consequently, the gravitational potential of hydrostatic tides at degree ℓ is

$$\phi_\ell^0 = \left(\frac{2\ell + 1}{\pi}\right) \frac{j_\ell(x)}{j_{\ell-1}(\pi)} - \left(\frac{x}{\pi}\right)^\ell,$$ (A.9)

and the hydrostatic Love number follows

$$k_\ell = \left(\frac{2\ell + 1}{\pi}\right) \frac{j_\ell(\pi)}{j_{\ell-1}(\pi)} - 1.$$ (A.10)

PROJECTION OF THE DYNAMICAL TIDE EQUATIONS INTO SPHERICAL HARMONICS

Here we project into spherical harmonics the equation for the potential ψ in a non-rotating (2.23) and rotating (2.14) $n = 1$ polytrope. The equation for the gravitational potential of dynamical tides is equation (2.15), forced by a different potential ψ depending on rotation. We evaluate solutions in the form

$$\psi = \sum_{\ell,m} \psi_{\ell,m}(x) Y_\ell^m(\theta, \varphi) e^{-i\omega t}, \tag{B.1}$$

$$\phi^{dyn} = \sum_{\ell,m} \phi_{\ell,m}^{dyn}(x) Y_\ell^m(\theta, \varphi) e^{-i\omega t}. \tag{B.2}$$

In the following, we conveniently drop the time-dependent part $e^{i\omega t}$ out of our derivation. Notice that we normalize the radial coordinate following $x = kr$, leading to a body of normalized radius $\pi = kR_p$.

B.1 The Coriolis-free $n = 1$ polytrope

We project into spherical harmonics the potential ψ (2.23) and the dynamical gravitational potential (2.15) of the non-rotating polytrope,

$$j_0(x) \left(\partial_{x,x}(\psi_{\ell,m}) + \left(\frac{2}{x} - \frac{j_1(x)}{j_0(x)} \right) \partial_x(\psi_{\ell,m}) + \left(1 - \frac{\ell(\ell+1)}{x^2} \right) \psi_{\ell,m} \right)$$
$$= \frac{\omega^2 j_\ell(x) (2\ell+1)}{4\pi^2 \mathcal{G} \rho_c j_{\ell-1}(\pi)}, \tag{B.3}$$

$$\partial_{x,x} \left(\phi_{\ell,m}^{dyn} \right) + \frac{2}{x} \partial_x \left(\phi_{\ell,m}^{dyn} \right) + \left(1 - \frac{\ell(\ell+1)}{x^2} \right) \phi_{\ell,m}^{dyn} = \psi_{\ell,m}. \tag{B.4}$$

B.2 The $n = 1$ polytrope

Relative to the left-hand side of equation (2.14), the projections of the first, second, and third terms, respectively follow

$$\nabla \cdot (j_0 \nabla \psi_{\ell,m}) = j_0 \left(\partial_{x,x} + \left(\frac{2}{x} - \frac{j_1}{j_0} \right) \partial_x - \frac{\ell(\ell+1)}{x^2} \right) \psi_{\ell,m} Y_\ell^m, \tag{B.5}$$

$$\frac{2}{i\omega} \nabla \cdot (j_0 \boldsymbol{\Omega} \times \nabla \psi_{lm}) = \frac{2m\Omega j_1}{\omega x} \psi_{\ell,m} Y_\ell^m, \tag{B.6}$$

$$-\frac{4}{\omega^2}\nabla\cdot\left(j_0\boldsymbol{\Omega}(\boldsymbol{\Omega}\cdot\nabla\psi_{\ell,m})\right) = -\frac{4\Omega^2}{\omega^2}\left(\left(j_0\partial_{x,x} - \left(j_1 + \frac{j_0}{x}\right)\partial_x\right)\psi_{\ell,m}Y_\ell^m\cos^2\theta\right.$$

$$+\frac{j_0}{x}\partial_x\psi_{\ell,m}Y_\ell^m + \left(\frac{2j_0}{x^2} + \frac{j_1}{x} - \frac{2j_0}{x}\partial_x\right)\psi_{\ell,m}\cos\theta\sin\theta\partial_\theta Y_\ell^m$$

$$\left.+\frac{j_0}{x^2}\psi_{\ell,m}\sin^2\theta\partial_{\theta,\theta}Y_\ell^m\right). \quad \text{(B.7)}$$

The multiplication of spherical harmonics with trigonometric functions expresses a physical statement about the coupling effect that Coriolis produces in the tidal gravitational response of a rotating body. The partial derivatives in the spherical harmonics indicate changes in quantum numbers described in the following differential relations (Lockitch and Friedman, 1999),

$$\sin\theta\partial_\theta Y_\ell^m = \ell Q_{\ell+1}Y_{\ell+1}^m - (\ell+1)Q_\ell Y_{\ell-1}^m, \quad \text{(B.8)}$$

$$\cos\theta Y_\ell^m = Q_{\ell+1}Y_{\ell+1}^m + Q_\ell Y_{\ell-1}^m, \quad \text{(B.9)}$$

where

$$Q_\ell = \left(\frac{\ell^2 - m^2}{4\ell^2 - 1}\right)^{1/2}. \quad \text{(B.10)}$$

Combining the previous differential relations, we arrive to expressions for each of the angular terms in equation (B.7),

$$Y_\ell^m\cos^2\theta = Q_{\ell-1}Q_\ell Y_{\ell-2}^m + (Q_\ell^2 + Q_{\ell+1}^2)Y_\ell^m + Q_{\ell+1}Q_{\ell+2}Y_{\ell+2}^m, \quad \text{(B.11)}$$

$$\cos\theta\sin\theta\partial_\theta Y_\ell^m = -(\ell+1)Q_{\ell-1}Q_\ell Y_{\ell-2}^m - \left((\ell+1)Q_\ell^2 - \ell Q_{\ell+1}^2\right)Y_\ell^m$$

$$+\ell Q_{\ell+1}Q_{\ell+2}Y_{\ell+2}^m, \quad \text{(B.12)}$$

$$\sin^2\theta\partial_{\theta,\theta}Y_\ell^m = (\ell+1)^2 Q_{\ell-1}Q_\ell Y_{\ell-2}^m + \left((2+\ell-\ell^2)Q_\ell^2 - \ell(\ell+3)Q_{\ell+1}^2\right)Y_\ell^m$$

$$+\ell^2 Q_{\ell+1}Q_{\ell+2}Y_{\ell+2}^m. \quad \text{(B.13)}$$

After grouping terms with the same spherical harmonic, equation (2.14) becomes an infinite set of ℓ-coupled radial equations following the structure of a Sturm-Liouville problem,

$$\left((P_{\ell,m}^{(1)}\partial_{x,x} + Q_{\ell,m}^{(1)}\partial_x + R_{\ell,m}^{(1)}\right)\psi_{\ell,m} + \left(P_{\ell,m}^{(2)}\partial_{x,x} + Q_{\ell,m}^{(2)}\partial_x + R_{\ell,m}^{(2)}\right)\psi_{l+2,m}$$

$$+\left(P_{\ell,m}^{(0)}\partial_{x,x} + Q_{\ell,m}^{(0)}\partial_x + R_{\ell,m}^{(0)}\right)\psi_{l-2,m}$$

$$= U_{\ell,m}\left(\frac{\omega^2 - 4\Omega^2}{4\pi G\rho_c}\right)\left(\frac{2\ell+1}{\pi}\right)\frac{j_\ell(x)}{j_{\ell-1}(\pi)}. \quad \text{(B.14)}$$

The nine radial coefficients correspond to

$$P_{\ell,m}^{(0)} = -\frac{4\Omega^2}{\omega^2} j_0 Q_{\ell-1} Q_\ell, \tag{B.15}$$

$$P_{\ell,m}^{(1)} = j_0 \left(1 - \frac{4\Omega^2}{\omega^2}(Q_\ell^2 + Q_{\ell+1}^2)\right), \tag{B.16}$$

$$P_{\ell,m}^{(2)} = -\frac{4\Omega^2}{\omega^2} j_0 Q_{\ell+1} Q_{\ell+2}, \tag{B.17}$$

$$Q_{\ell,m}^{(0)} = \frac{4\Omega^2}{\omega^2} \left((2\ell - 3)\frac{j_0}{x} + j_1\right) Q_{\ell-1} Q_\ell, \tag{B.18}$$

$$Q_{\ell,m}^{(1)} = \frac{2j_0}{x} - j_1 - \frac{4\Omega^2}{\omega^2} \left(\frac{j_0}{x}\left(1 + (2\ell + 1)(Q_\ell^2 - Q_{\ell+1}^2)\right) - j_1(Q_\ell^2 + Q_{\ell+1}^2)\right), \tag{B.19}$$

$$Q_{\ell,m}^{(2)} = -\frac{4\Omega^2}{\omega^2} \left((2\ell - 3)\frac{j_0}{x} - j_1\right) Q_{\ell+1} Q_{\ell+2}, \tag{B.20}$$

$$R_{\ell,m}^{(0)} = -\frac{4\Omega^2}{\omega^2}(\ell - 2)\left(\ell\frac{j_0}{x^2} + \frac{j_1}{x}\right) Q_{\ell-1} Q_\ell, \tag{B.21}$$

$$R_{\ell,m}^{(1)} = -\frac{l(l+1)j_0}{x^2} + \frac{2m\Omega j_1}{\omega x}$$
$$+ \frac{4\Omega^2}{\omega^2}\left(\frac{j_1}{x}((\ell+1)Q_\ell^2 - \ell Q_{\ell+1}^2) + \frac{j_0}{x^2}\ell(\ell+1)(Q_\ell^2 + Q_{\ell+1}^2)\right), \tag{B.22}$$

$$R_{\ell,m}^{(2)} = -\frac{4\Omega^2}{\omega^2}\left((\ell(\ell+4) + 11)\frac{j_0}{x^2} - (\ell - 1)\frac{j_1}{x}\right) Q_{\ell+1} Q_{\ell+2}. \tag{B.23}$$

The projection into the spherical harmonics of the boundary condition (2.38) leads to

$$Y_\ell^m \left(\partial_x \psi_{\ell,m} - \frac{2m\Omega}{\omega\pi}\psi_{\ell,m}\right) \quad - \quad \frac{4\Omega^2}{\omega^2}\left(Y_\ell^m \cos^2\theta \partial_x \psi_{\ell,m} - \frac{\psi_{\ell,m}}{\pi}\sin\theta\cos\theta\partial_\theta Y_\ell^m\right)$$
$$= \quad U_{\ell,m}\left(\frac{4\Omega^2 - \omega^2}{g}\right)\left(\frac{2\ell+1}{\pi}\right)\frac{j_\ell(x)}{j_{\ell-1}(\pi)} Y_\ell^m. \tag{B.24}$$

The previous differential relations still apply to deal with coupled spherical harmonics in the boundary condition. Grouping terms for each spherical harmonic Y_ℓ^m, we reach an ℓ-coupled boundary condition with the structure

$$\sum_{j=0}^{2}\left(\hat{Q}_{\ell,m}^{(j)}\partial_x + \hat{R}_{\ell,m}^{(j)}\right)\psi_{\ell+2j-2}^m = U_{\ell,m}\left(\frac{4\Omega^2 - \omega^2}{g}\right)\left(\frac{2\ell+1}{\pi}\right)\frac{j_\ell(\pi)}{j_{\ell-1}(\pi)}. \tag{B.25}$$

The six radial coefficients correspond to

$$\hat{Q}^{(0)}_{\ell,m} = -\frac{4\Omega^2}{\omega^2} Q_{\ell-1} Q_\ell, \tag{B.26}$$

$$\hat{Q}^{(1)}_{\ell,m} = 1 - \frac{4\Omega^2}{\omega^2} \left(Q_\ell^2 + Q_{\ell+1}^2 \right), \tag{B.27}$$

$$\hat{Q}^{(2)}_{\ell,m} = -\frac{4\Omega^2}{\omega^2} Q_{\ell+1} Q_{\ell+2}, \tag{B.28}$$

$$\hat{R}^{(0)}_{\ell,m} = \frac{4\Omega^2}{\pi\omega^2} (\ell - 2) Q_{\ell-1} Q_\ell, \tag{B.29}$$

$$\hat{R}^{(1)}_{\ell,m} = -\frac{2m\Omega}{\pi\omega} - \frac{4\Omega^2}{\pi\omega^2} \left((\ell + 1) Q_\ell^2 - \ell Q_{\ell+1}^2 \right), \tag{B.30}$$

$$\hat{R}^{(2)}_{\ell,m} = -\frac{4\Omega^2}{\pi\omega^2} (\ell - 1) Q_{\ell+1} Q_{\ell+2}. \tag{B.31}$$

A p p e n d i x C

CHEBYSHEV PSEUDOSPECTRAL METHOD

We solve the Sturn-Liouville differential problem (Boyd, 2001) defined by

$$p(r)u''(r) + q(r)u'(r) + r(r)u(r) = f(r), \tag{C.1}$$

and constrained to the boundary conditions

$$\alpha_0 u'(a) + \alpha_1 u(a) = \alpha_2, \tag{C.2}$$

$$\beta_0 u'(b) + \beta_1 u(b) = \beta_2, \tag{C.3}$$

where a and b are the two ends of a boundary value problem. We shift the domain of equation (C.1) from $r \in [a, b]$ to the domain of Chebyshev polynomials $\mu \in [-1, 1]$ and seek for a solution that is a truncated sum of an infinite Chebyshev series,

$$u(\mu) \approx \sum_{n=0}^{N_{max}} a_n T_n(\mu), \tag{C.4}$$

with the Chebyshev polynomials defined by

$$T_n(\mu) = \cos(nt), \tag{C.5}$$

and $t = \arccos(\mu)$. Our objective is to obtain the coefficients a_n by solving a linear inverse problem,

$$La = f. \tag{C.6}$$

The square matrix L and the vector f come from the evaluation of equation (C.1) into Gauss-Lobatto collocation points defined by

$$\mu_i = \cos\left(\frac{\pi i}{N-1}\right), \qquad i = 1, 2, \ldots, N-1, \tag{C.7}$$

plus the constraints from boundary conditions. The partial derivatives in equation (C.1) assume the analytical form

$$\frac{\partial T_n(\mu)}{\partial \mu} = n\frac{\sin(nt)}{\sin(t)}, \tag{C.8}$$

$$\frac{\partial^2 T_n(\mu)}{\partial \mu^2} = -n^2\frac{\cos(nt)}{\sin^2(t)} + \left(\frac{n\cos(t)}{\sin^3(t)}\right)\sin(nt). \tag{C.9}$$

A p p e n d i x   D

TIDAL FLOW IN A UNIFORM-DENSITY SPHERE

We calculate the tidal flow from projecting equation (2.9) into Cartesian coordinates,

$$\mathbf{v} = -\left(\frac{i\omega}{4\Omega^2 - \omega^2}\right)\left(\hat{x}\left(\partial_x + \frac{2i\Omega}{\omega}\partial_y\right) + \hat{y}\left(\partial_y - \frac{2i\Omega}{\omega}\partial_x\right) + \hat{z}\left(\frac{4\Omega^2}{\omega^2} - 1\right)\partial_z\right)\psi.$$
(D.1)

The potential ψ depends on the potential of the gravitational pull (2.19) and the tidal potential internal to the thin shell disturbed by tides. Analogous to what we did for the external potential, we obtain the tidal gravitational potential (i.e., $r < R_p$) from integration throughout the volume,

$$\phi'_2 = \frac{3}{5}\left(\frac{r}{R_p}\right)^2 g\xi_2,$$
(D.2)

which leads to

$$\psi_2 = \frac{R_p\omega(2\Omega - \omega)}{2g}\tilde{\phi_2}' = \frac{AR_p\omega(2\Omega - \omega)}{2g}(x - iy)^2.$$
(D.3)

The constant A comes from the numerical factor of the relevant potentials, corresponding to

$$A = \frac{3}{16}\frac{Gm_s}{a^3} + \frac{3}{20}\sqrt{\frac{15}{2\pi}}\frac{g\xi_2}{R_p^2}.$$
(D.4)

As shown in equation (D.3), ψ_2 is independent of z, leading to a 2-D tidal flow in equatorial planes. Replacing equation (D.3) into equation (D.1), the degree-2 tidal flow becomes

$$\mathbf{v}_2 = -\frac{A\omega R_p}{g}\left(\hat{x}(ix + y) + \hat{y}(x - iy)\right).$$
(D.5)

A p p e n d i x   E

THE OBLATE FIGURE OF A GAS GIANT PLANET

In this appendix, we revise the classical result of calculating the first–order figure of a gas giant planet mostly made of H-He (i.e., an $n = 1$ polytrope) after being perturbed by the centrifugal effect (Hubbard, 1984). The external potential of a body perturbed by the centrifugal effect follows

$$\phi \approx \frac{\mathcal{G}M}{r} \left(1 - \left(\frac{s}{r} \right)^2 J_2 \mathcal{P}_2(\cos \theta) \right), \tag{E.1}$$

and the rotational forcing potential follows

$$\phi_R = \frac{\Omega^2 r^2}{3} \left(1 - \mathcal{P}_2(\cos \theta) \right), \tag{E.2}$$

where $\mathcal{G}$ is the gravitational constant, M is the mass of the planet, s is the average planetary radius, Ω is the planet's rotational frequency, J_2 is the zonal gravitational coefficient of degree $\ell = 2$, and $\mathcal{P}_2$ the Legendre Polynomial of degree $\ell = 2$. The outer boundary of the planet represents an equipotential surface where pressure is constant. If $R(\theta)$ represents the outer boundary of the planet, we require to satisfy

$$\phi(R) + \phi_R(R) = \text{constant} = \phi(\theta = 0), \tag{E.3}$$

or

$$\frac{\mathcal{G}M}{R} \left(1 - \left(\frac{s}{R} \right)^2 J_2 \mathcal{P}_2(\cos \theta) \right) + \frac{\Omega^2 R^2}{3} \left(1 - \mathcal{P}_2(\cos \theta) \right) = \frac{\mathcal{G}M}{b} \left(1 - \left(\frac{s}{b} \right)^2 J_2 \right), \tag{E.4}$$

where b is the polar radius. We consider the first–order expansion on the oblate figure of the planet as

$$R(\theta) = \sum_{\ell=0}^{\infty} \delta r_{2\ell} \mathcal{P}_{2\ell}(\cos \theta) \approx s + \delta r_2 \mathcal{P}_2(\cos \theta), \tag{E.5}$$

where δr_2 is a $\ell = 2$ perturbation to the figure of the planet. After replacing the first–order expansion of $R(\theta)$ into Equation (E.4), we obtain the classical result

$$\frac{\delta r_2}{s} \approx - \left(J_2 + \frac{q}{3} \right), \tag{E.6}$$

which is accurate to first order in q, and q is the adimensional rotational parameter.

To obtain J_2 in an $n = 1$ polytrope, we equal the external potential in Equation (E.1) to the $\ell = 2$ rotational gravitational response of the polytrope to the centrifugal effect, both evaluated at $r = s$,

$$J_2 = (5j_2(\pi) - 1)\frac{q}{3},$$ (E.7)

where j_2 is the spherical Bessel function of the first kind. The rotational gravitational response in a $n = 1$ polytrope follows the same equations and boundary conditions than the tidal gravitational response with ϕ_T replaced by ϕ_R in Equation (3.6). Finally, we obtain the first–order oblate figure of a rotating gas giant planet perturbed by the centrifugal effect,

$$R(\theta) \approx s\left(1 - \frac{5}{\pi^2}q\mathcal{P}_2(\cos\theta)\right).$$ (E.8)

A p p e n d i x   F

DYNAMICAL LOVE NUMBERS OF GAS GIANT PLANETS

The dynamical Love number describes dynamical tides where inertial effects in the response of the planet are taken into account. The associated tradional equation of motion corresponds to $F = M\dot{v}$, where F includes the tidal forcing and self–gravitation of the tidally displaced mass, M the tidally displaced mass, and v the tidal flow. Alternatively, the hydrostatic Love number describes an instantaneous response where the equation of motion to solve reduces to the traditional $F = 0$. In a gas giant planet, the linearly perturbed equation of motion for dynamical tides becomes (Idini and Stevenson, 2021)

$$- i\omega \mathbf{v} + 2\mathbf{\Omega} \times \mathbf{v} = -\frac{\nabla p'}{\rho} + \frac{\rho'}{\rho^2}\nabla p + \nabla \tilde{\phi}', \tag{F.1}$$

where ω is the tidal frequency, $\mathbf{\Omega}$ is the spin rate of the planet, p is pressure, ρ is density, and $\tilde{\phi}$ is the resulting tidal potential after adding the tidal forcing potential and the self-gravitation potential. The primes represent Eulerian linear perturbations.

Alternatively to solve the tidal equation of motion (Equation F.1 coupled to Poisson's and continuity equations; for an example, see Idini and Stevenson (2021)), the dynamical Love number can be obtained from considering the dynamical response of periodically excited harmonic oscillators with oscillation frequency ω_0 (Idini and Stevenson, 2021)

$$\Delta k = \frac{\omega^2}{\omega_0^2 - \omega^2}, \tag{F.2}$$

where Δk represents the fractional correction to the hydrostatic Love number due to dynamical effects. In Equation (F.2), the frequency ω_0 represents the f–mode oscillation frequency of the planet, which is forced by a periodic loading with frequency ω associated to the gravitational pull of the companion satellite.

Several additional effects complicate a practical use of Equation (F.2), which is qualitatively illuminating but fails at delivering useful predictions. In Jupiter and Saturn, fast rotation introduces the Coriolis effect as an important new term in the equation of motion (i.e., the term $2\mathbf{\Omega} \times \mathbf{v}$ in Equation F.1). Even in this case, the dynamical Love number can still be represented by periodically forced normal

modes, but the new dynamics change the tidal motion in important ways. The f–mode dynamical response changes in sign and amplitude (Idini and Stevenson, 2021), and a new set of modes restored by the Coriolis force join the already existent p– and f–modes (Dewberry and Lai, 2022).

When rotation is treated as a linear perturbation, we can write the dynamical Love number as (Lai, 2021)

$$k_{\ell m} \simeq \left(\frac{4\pi}{2\ell + 1}\right) \sum_\alpha \frac{Q_\alpha^2}{\omega_\alpha^2 - (mC_\alpha\Omega + \omega)^2}, \tag{F.3}$$

where the sum over α represents a sum over all normal modes trapped inside the planet, ω_α is the mode frequency, Q_α is the coupling integral defined in Equation (4.3), C_α is the rotational coefficient defined in Equation (4.4), ℓ is degree, and m is azimuthal order.

The hydrostatic Love number emerges from f–modes in Equation (F.3) when $\omega = 0$. Other modes (i.e., p–, g–, and inertial modes restored by Coriolis) weakly couple to the tidal forcing (i.e., they have a small Q_α), thus only contribute to the dynamical Love number when the mode frequency ω_α approaches the forcing frequency ω. The dynamical contribution from inertial modes restored by Coriolis requires a nonperturbative treatment of rotation, which complicates the numerical calculation of mode properties but preserves the main idea behind Equation (F.3) (Dewberry and Lai, 2022).

RESONANT LOCKING APPLIED TO A PLANET–SATELLITE SYSTEM

In a state of resonant locking, the migration rate $\dot{a}$ of the satellite depends only on the planetary evolution of the central planet (Fuller et al., 2016),

$$\frac{\dot{a}}{a} = \frac{2}{3} \left(\frac{\Omega}{\omega_s} \left(\frac{\dot{\omega}_\alpha}{\omega_\alpha} - \frac{\dot{\Omega}}{\Omega} \right) - \frac{\dot{\omega}_\alpha}{\omega_\alpha} \right), \tag{G.1}$$

where Ω is the spin–rate of the planet, ω_s is the orbital frequency of the satellite, and ω_α is the oscillation frequency of the resonant mode trapped inside the planet. Resonant locking extends the lifetime of interior–orbital resonances to geological timescales, diminishing the secular tidal Q of the tidal bulge associated to the resonant mode and modifying the secular amplitude of dynamical tides.

The basic conditions required to maintain a state of resonant locking are the following (Fuller et al., 2016):

1. The resonance must greatly increase the amount of tidal dissipation after it kicks in, so that satellite migration accelerates when $\omega \approx \omega_\alpha$.

2. The resonance must migrate in the same direction of satellite migration. For a satellite migrating outwards, the mode frequency should increase in time to encounter the also increasing tidal frequency $\omega = m(\Omega - \omega_s)$, where m is the azimuthal order and ω_s diminishes as the orbit expands.

3. Tidal dissipation at resonance must accelerate the satellite migration to match the evolution of the resonant mode. If satellite migration cannot match the mode evolution $\dot{\omega}_\alpha$ before saturation of the resonance, the resonance migrates past the orbital frequency and resonant locking fails.

A p p e n d i x   H

A SIMPLIFIED EQUATION OF STATE OF MIXTURES

We compute the pressure p in a mixture of H-He fluid with density ρ and heavy elements with density ρ_z using volume additivity of the individual constituents (Equation (4.6)). For H-He fluid following an $n = 1$ polytropic equation of state with a He cosmic abundance, the pressure follows

$$p = K\rho^2 f^2, \tag{H.1}$$

where the radial function $f(r)$ is

$$f(r) = \frac{1 - Z}{1 - \frac{\rho}{\rho_z}Z}. \tag{H.2}$$

The ratio ρ/ρ_z becomes small near the atmosphere but non-negligible near the core region. To a good approximation, the pressure-density relation for an adiabatic distribution of 'rocky' heavy elements follows (Hubbard and Marley, 1989):

$$p \approx \left(\frac{1.4}{1000}\right)\rho_z^{4.4}, \tag{H.3}$$

with p in Mbar and ρ_z in g/cm^3. Near the center of Jupiter, pressure reaches $p \sim \mathcal{G}M_J^2/4R_J^4 \sim 30$Mbar and fluid density $\rho \sim 4.4$ g/cm^3, which leads to a ratio $\rho/\rho_z \sim 0.4$. We approximate the ratio ρ/ρ_z by treating ρ as the density of pure H-He fluid and ρ_Z as the density of 'rocky' heavy elements (Equation H.3) subjected to the hydrostatic pressure obtained from a body made of pure H-He fluid (i.e., $p = K\rho_c^2 j_0^2(kr)$)

$$\frac{\rho}{\rho_z} \approx 0.42\,(j_0(kr))^{0.6}. \tag{H.4}$$

We can now rewrite $f(r)$ as

$$f(r) = \frac{1 - Z}{1 - 0.42\,(j_0(kr))^{0.6}\,Z}. \tag{H.5}$$

The hydrostatic density profile of the mixture comes from solving a differential equation similar to Lane-Emden's equation. After defining the auxiliary variable $\tilde{\rho} = \rho f$, hydrostatic equilibrium imposes

$$\frac{1}{\rho}\frac{\partial p}{\partial r} = 2Kf\frac{\partial \tilde{\rho}}{\partial r} = -g. \tag{H.6}$$

After substituting the previous equation into the resulting equation from differentiating with respect to r, we reach a second-order differential equation on $\tilde{\rho}$,

$$\frac{\partial^2 \tilde{\rho}}{\partial r^2} + \left(\frac{\partial \log f}{\partial r} + \frac{2}{r}\right) \frac{\partial \tilde{\rho}}{\partial r} + \left(\frac{k}{f}\right)^2 \tilde{\rho} = 0. \tag{H.7}$$

The usual boundary conditions $\rho = \rho_c$ and $\rho' = 0$ at the center lead to a new set of boundary conditions

$$\tilde{\rho}(0) = f(0)\rho_c = \left(\frac{1 - Z_c}{1 - 0.42 Z_c}\right)\rho_c, \tag{H.8}$$

$$\left.\frac{\partial \tilde{\rho}}{\partial r}\right|_{r=0} = 0. \tag{H.9}$$

We solve Equation (H.7) numerically after normalizing $\tilde{\rho}$ by the central density ρ_c. We use the result to calculate ρ_c from Jupiter's mean density $\bar{\rho}_J$, according to

$$\bar{\rho}_J = \left(\frac{3}{R_J^3}\right) \int_0^{R_J} \rho r^2 dr. \tag{H.10}$$

A p p e n d i x   I

EARTHQUAKE CYCLE SIMULATIONS

I.1   Methods

We characterize the effect of a LVFZ on rise-time and slip profile in earthquake cycle simulations covering a wide range of values of LVFZ thickness and damage. We adopt a spectral boundary integral equation method (SBIEM) (Luo et al., 2017) and a quasi-dynamic approximation where wave-related effects are crudely represented by a radiation-damping term (Rice, 1993). The static stress transfer kernel required in the SBIEM for a LVFZ is derived in Text S2. The modeling approach captures the static LVFZ effects described in Section 2 of the main text, without including any dynamic effect of fault zone reflected waves, and its computational efficiency enables a comprehensive exploration of the parameter space.

The fault strength is prescribed by the Dieterich-Ruina rate-and-state friction law coupled with the "ageing law" of state evolution (Dieterich, 1981; Ruina, 1980, 1983),

$$\tau/\sigma = \mu_0 + a \ln \left(\frac{V}{V_0} \right) + b \ln \left(\frac{V_0 \theta}{D_c} \right), \tag{I.1}$$

$$\dot{\theta} = 1 - \frac{V\theta}{D_c}, \tag{I.2}$$

where τ and σ are the shear and normal fault stresses, respectively, V is slip rate and θ a fault state variable. The parameter a quantifies the direct effect, b the evolution effect, and D_c is the characteristic slip related to the state evolution. Under steady-state, $b > a$ leads to stick-slip behavior (velocity-weakening, VW) whereas $b < a$ leads to stable sliding behavior (velocity-strengthening, VS). We represent a seismogenic zone driven by surrounding creep by prescribing a VW patch of length L_{vw} in the middle of the fault, surrounded by two VS segments of total length $3L_{vw}$ and, at further distance, by steady uniform creep at slip rate V_{pl} (Fig. I.1). The parameter values of our numerical model are given in Table S2.

Ruptures that start as a crack and later turn into a pulse require a minimum rupture distance to develop the transition, therefore a sufficiently large ratio between L_{vw} and the nucleation length L_{nuc} (Rubin and Ampuero, 2005),

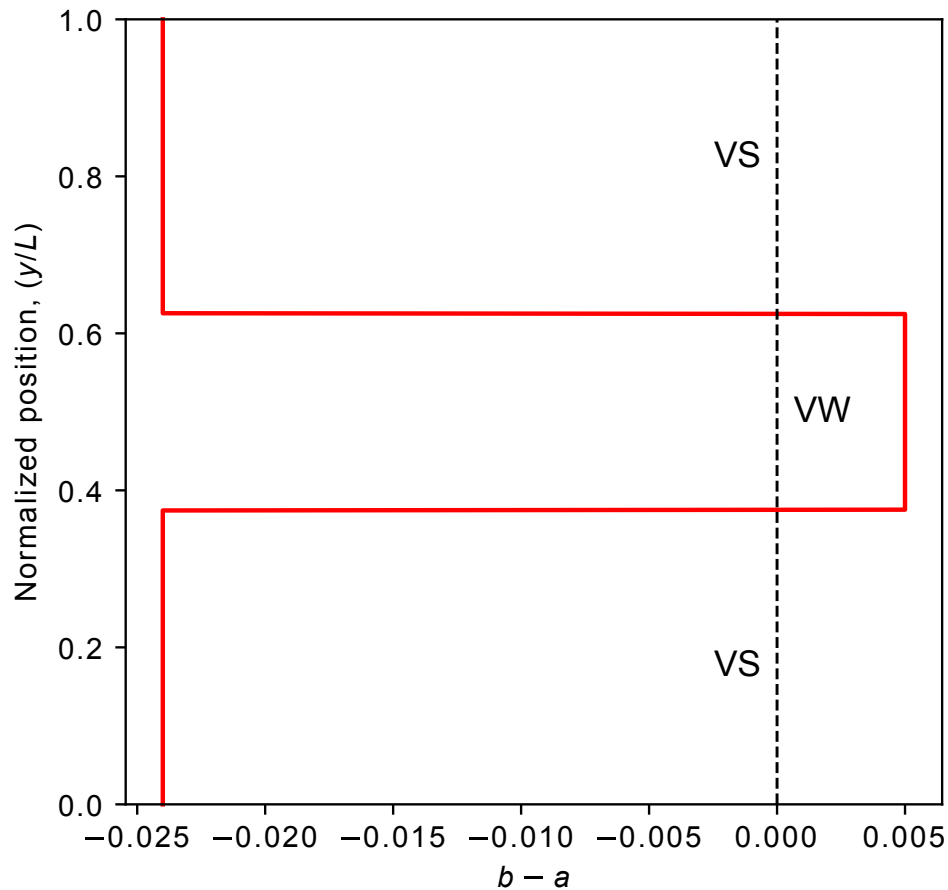$$L_{nuc} = \frac{2}{\pi} \frac{\mu D_c b}{\sigma (b-a)^2}. \tag{I.3}$$

Figure I.1: The $b - a$ parameter along position in the fault. The seismogenic zone is indicated as a velocity-weakening zone (VW) surrounded by two stably sliding velocity-strengthening (VS) segments.

Previous earthquake cycle simulations including a LVFZ model did not show significant reductions in rise-time for $L_{vw} \sim 1.5 L_{nuc}$ and $\Delta = 0.36$ (Kaneko et al., 2011), so we extended the seismogenic length to $L_{vw} \sim 10 L_{nuc}$. Moreover, we explored values of Δ ranging from moderate damage to the upper bound inferred from current seismological observations ($\Delta = 0.5 - 0.9$) and values of h extending over a range wide enough to encompass most geological and seismological observations ($2h/L_{vw} \sim 10^{-3} - 10$). A compilation of observed or estimated levels of damage and fault-zone thickness in natural faults is given in Fig. S6.

We prescribed a minimum of five elements within an effective cohesive zone,

$$L_b^* = \frac{9\pi}{32} \frac{\mu^* D_c}{\sigma b}, \tag{I.4}$$

where μ^* is an effective shear modulus that accounts for the LVFZ derived bellow. A well-resolved cohesive zone was verified a posteriori in all our simulation results, characterized by a smooth and properly sampled stress distribution near the rupture tips.

I.2   Estimation of the process zone size in a LVFZ.

The components of slip and stress drop at a wavenumber k^* are related by an effective shear modulus, μ^*, which represents an effective value of the shear modulus profile $\mu(x)$ up to an off-fault distance comparable to $\lambda^* = 2\pi/k^*$. As is the case of a homogeneous medium, the static stress transfer at this effective length scale can be written as

$$\mathcal{K}(k^*) = \frac{1}{2}\mu^*|k^*|. \tag{I.5}$$

Combining equations (J.9) and (I.5), we obtain

$$\mu^* = \mu(1 - \Delta) \coth(h|k^*| + \mathrm{atanh}(1 - \Delta)). \tag{I.6}$$

An estimate of the process zone size in a LVFZ, L_b^*, is related to the process zone size in an intact medium, L_b, by

$$L_b^* = L_b \frac{\mu^*}{\mu}. \tag{I.7}$$

After replacing Eq. (I.6) into Eq. (I.7) and setting $\lambda^* \approx L_b^*$, the process zone in a LVFZ satisfies

$$L_b^* = L_b(1 - \Delta) \coth\left(\frac{2\pi h}{L_b^*} + \mathrm{atanh}(1 - \Delta)\right). \tag{I.8}$$

This equation is solved numerically to obtain L_b^*/L_b as a function of Δ and h/L_b.

Appendix J

THE STATIC STRESS TRANSFER KERNEL IN A LVFZ MODEL

J.1   Problem statement

Let us consider a 2D elastic medium where the fault is located on the line $x = 0$. The medium is heterogeneous with the shear modulus μ depending only on x. Slip is anti-plane in the direction out of the $x - y$ plane. A static slip distribution $\mathcal{D}(y)$ produces a shear stress on the fault $\mathcal{T}(y)$. Because the elasticity problem is linear, slip and stress are related by a linear relation,

$$\mathcal{T}(y) = -\int_{-\infty}^{\infty} \mathcal{K}(y, y')\mathcal{D}(y')dx', \tag{J.1}$$

where $\mathcal{K}$ is the static stress transfer kernel. The minus sign is introduced to give $\mathcal{K}$ a meaning analogous to stiffness in a spring-block system. As the problem is invariant by translation along y ($\mathcal{K}(y, y') = \mathcal{K}(y - y')$), Eq. (J.1) is a convolution,

$$\mathcal{T}(y) = -\int_{-\infty}^{\infty} \mathcal{K}(y - y')\mathcal{D}(y')dy'. \tag{J.2}$$

After a Fourier transform, the convolution simplifies into a product,

$$\mathcal{T}(k) = -\mathcal{K}(k)\mathcal{D}(k), \tag{J.3}$$

where k is the wavenumber along the fault direction, y. In order to connect stress and slip in the fault, the goal is to derive an expression for the static kernel in spectral domain, the so-called spectral stiffness $\mathcal{K}(k)$.

The equation of anti-plane elasticity governing the displacement field $u(x, y)$ parallel to z is

$$\mu(x)u_{,yy} + (\mu(x)u_{,x})_{,x} = 0. \tag{J.4}$$

A first boundary condition is the symmetric distribution of applied slip on each side of the fault,

$$u(0^{\pm}, y) = \pm\frac{1}{2}\mathcal{D}(y). \tag{J.5}$$

A second boundary condition requires that displacement u must be finite at $x = \pm\infty$. As the boundary conditions are symmetric, the resulting displacements are symmetric as well and follow $u(-x, y) = -u(x, y)$. Therefore, we solve for the

half-plane $x \geq 0$ only. After applying a Fourier transform over Eq. (J.4), our task is reduced to find $u(x, k)$ such that

$$-k^2 \mu(x) u + (\mu(x) u_{,x})_{,x} = 0$$
$$u(0^+, k) = \frac{1}{2} \mathcal{D}(k) \tag{J.6}$$
$$u(\infty, k) < 0$$

and then evaluate the fault shear stress $\mathcal{T}(k) = \mu(0) u(0, k)_{,x}$.

The problem has analytical solutions only for certain shear-modulus distributions $\mu(x)$. In the following we address two cases: a homogeneous medium and a two-layer medium. An analytical solution for an exponential distribution of $\mu(x)$ is possible as well but not exposed here (Ampuero et al., 2002).

J.2 Homogeneous medium

In a homogeneous medium, Eq. (J.4) reduces to

$$-k^2 u + u_{,xx} = 0. \tag{J.7}$$

Its well-known general solution is $u(x, k) = A \exp(-|k|x) + B \exp(|k|x)$. The finite displacement boundary condition imposes $B = 0$, and the fault boundary condition at $x = 0$ implies $A = \frac{1}{2} \mathcal{D}$. The resulting displacement is $u(x, k) = \frac{1}{2} \mathcal{D}(k) \exp(-|k|x)$. After evaluating the shear stress on the fault, $\mathcal{T}(k) = -\frac{1}{2}\mu|k|\mathcal{D}(k)$, the spectral stiffness is

$$\mathcal{K}(k) = -\mathcal{T}(k)/\mathcal{D}(k) = \frac{1}{2}\mu|k|. \tag{J.8}$$

J.3 Two-layer medium

Consider a fault in a homogeneous medium surrounded by two layers of uniform half-thickness h and homogeneous but reduced shear modulus (Fig. 1b). Within the layers the shear modulus is $\mu(1 - \Delta)$ and outside the layers it is μ. The derivation of the kernel in a layered medium follows the same steps as the previously addressed case. The differential equation is Eq. (J.7). Its general solution is a combination of exponential functions for each layer, together with a total of four new constants analogous to A and B. Two new boundary conditions arise: continuity of displacement and stress across the interface between the layers, $u(h^+, k) = u(h^-, k)$ and $(1 - \Delta)u(h^-, k)_{,x} = u(h^+, k)_{,x}$.

It is possible to obtain the displacement $\mathcal{D}(x, k)$ after some algebraic work, then derive the shear stress at the fault and finally the spectral kernel,

$$\mathcal{K}(k) = \frac{1}{2}\mu|k|(1 - \Delta)\coth(h|k| + \operatorname{atanh}(1 - \Delta)). \tag{J.9}$$

J.4   Static slip profiles with constant stress drop

A first application of Eq. (J.9) is to numerically compute the static slip profiles of a rupture with prescribed constant stress drop propagating in a fault with a LVFZ (Fig. 1c). By applying an inverse fast Fourier transform to Eq. (J.9) over a very long fault, we obtained a static stress transfer kernel in space domain, $\mathcal{K}(y)$. Then assuming a uniform stress drop, we solved numerically the discretized version of Eq. (J.2) to obtain the slip profiles.

J.5   Numerical implementation of a LVFZ

Our numerical implementation of a LVFZ on multi-cycle earthquake simulations consists of combining the time-domain kernel of a fault with finite length (Cochard and Rice, 1997) with Eq. (J.9) in the frequency domain. The numerical models shown in Fig. 3 are based on this implementation. We verified that the values of the obtained kernel are similar to those obtained by the more expensive approach of applying Eq. (J.9) to a periodic homogeneous fault 32 times longer (Fig. J.1).
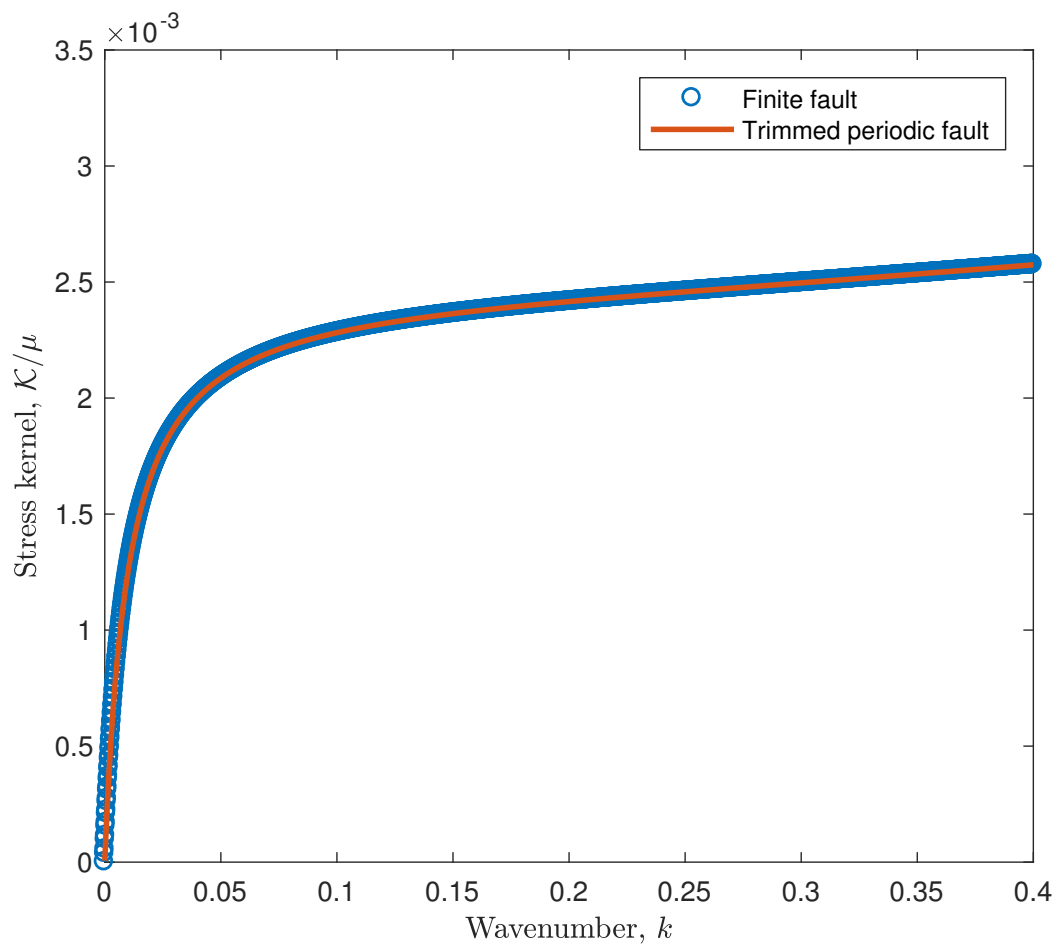
Figure J.1: Static stress kernel in a LVFZ versus wavenumber based on two numerical implementations. The blue circles represent the combination of the kernel of a finite fault with Eq. (J.9) in the wavenumber domain. The continuous orange line is an approximated kernel using Eq. (J.9) over a periodic fault 32 times longer.

A p p e n d i x   K

THE STRESS TRANSFER IN A LVFZ AND A BURRIDGE-KNOPOFF MODEL

K.1   Burridge-Knopoff (BK) model

In a BK model (Burridge and Knopoff, 1967), the quasi-static slip $\mathcal{D}_i$ and stress $\mathcal{T}_i$ at the base of the i-th block of area dy^2 relate to each other as

$$\mathcal{T}_i dy^2 = -k_L(\mathcal{D}_i - \mathcal{D}_L) + \bar{\mathcal{K}}(\mathcal{D}_{i-1} - 2\mathcal{D}_i + \mathcal{D}_{i+1}), \tag{K.1}$$

where $\mathcal{D}_L$ is the loading displacement, k_L the loading stiffness, and $\bar{\mathcal{K}}$ the stress transfer due to the relative motion of the sliders. We furthermore introduce a loading stiffness per unit area of block surface defined as

$$\bar{\mathcal{K}}_L = k_L/dy^2. \tag{K.2}$$

Taking the continuum limit ($dy \to 0$) in Eq. (K.1):

$$\mathcal{T}(y) = -\bar{\mathcal{K}}_L(\mathcal{D}(y) - \mathcal{D}_L) + \bar{\mathcal{K}}\mathcal{D}_{,yy}. \tag{K.3}$$

The second term in the right-hand side in the equation above is derived by expanding terms in a Taylor series up to second order at small dy,

$$\mathcal{D}_{,yy} \approx \frac{\mathcal{D}(y - dy) - 2\mathcal{D}(y) + \mathcal{D}(y + dy)}{dy^2} = \frac{\mathcal{D}_{i-1} - 2\mathcal{D}_i + \mathcal{D}_{i+1}}{dy^2}. \tag{K.4}$$

Taking the Fourier transform for non-zero wavenumbers ($|k| > 0$),

$$\mathcal{T}(k) = -\bar{\mathcal{K}}_L\mathcal{D}(k) - \bar{\mathcal{K}}k^2\mathcal{D}(k) = -(\bar{\mathcal{K}}_L + \bar{\mathcal{K}}k^2)\mathcal{D}(k). \tag{K.5}$$

The loading displacement $\mathcal{D}_L$ is spatially uniform, hence it only contributes when $k = 0$. We get the following static kernel in spectral domain,

$$\mathcal{K}(k) = \bar{\mathcal{K}}_L + \bar{\mathcal{K}}k^2. \tag{K.6}$$

K.2   Static slip induced by uniform stress drop in the continuum BK model

Consider a uniform stress drop within a rupture segment of size r, i.e.

$$\Delta\tau = \bar{\mathcal{K}}_L\mathcal{D}(y) - \bar{\mathcal{K}}\mathcal{D}_{,yy}, \tag{K.7}$$

for $y \in [-r/2, r/2]$, and zero slip elsewhere. The solution to the second-order linear ODE above is the sum of a particular solution satisfying the ODE (here, a uniform slip profile) and the general solution to the homogeneous version of the ODE,

$$\mathcal{D}(y) = \frac{\Delta\tau}{\bar{\mathcal{K}}_L} + Ae^{\kappa y} + Be^{-\kappa y}, \tag{K.8}$$

where $\kappa = \sqrt{\bar{\mathcal{K}}_L/\bar{\mathcal{K}}}$. The constants A and B are determined by enforcing the boundary conditions at the rupture tips, $\mathcal{D}(\pm r/2) = 0$,

$$A = B = -\frac{\Delta\tau}{2\bar{\mathcal{K}}_L \cosh(\kappa r/2)}. \tag{K.9}$$

Thus, the slip profile is

$$\mathcal{D}(y) = \frac{\Delta\tau}{\bar{\mathcal{K}}_L} \left(1 - \frac{\cosh(\kappa y)}{\cosh(\kappa r/2)} \right). \tag{K.10}$$

Figure K.1 shows the resulting slip profiles for a range of values of the dimensionless number κr. For large κr values, the slip is flat over most of the rupture, as in pulse-like ruptures, with slip approximately equal to $\Delta\tau/\bar{\mathcal{K}}_L$.

K.3 Comparison between LVFZ and BK kernels

For a LVFZ model, we rewrite the kernel given in Eq. (J.9) as

$$\mathcal{K}(k) = \frac{1}{2}\mu_d|k| \left(\frac{1 + (1 - \Delta)\tanh(1 - \Delta)}{1 - \Delta + \tanh(h|k|)} \right). \tag{K.11}$$

In a highly damaged fault zone where $\Delta \to 1$, the kernel reduces to

$$\mathcal{K}(k) \approx \frac{1}{2}\mu_d|k| \left(\frac{1}{1 - \Delta + \tanh(h|k|)} \right). \tag{K.12}$$

The high-frequency regime is defined by $\tanh(h|k|) \gg 1 - \Delta$ and leads to

$$\mathcal{K}(k) \approx \frac{1}{2}\mu_d|k| \coth(h|k|). \tag{K.13}$$

Moreover, if $h|k| \ll 1$, by Taylor expansion we obtain

$$\mathcal{K}(k) \approx \frac{\mu_d}{2h} + \frac{1}{6}\mu_d hk^2. \tag{K.14}$$

This shows that, under certain conditions for $h|k|$, the stress transfer of the LVFZ model is equivalent to that of the BK model, with the following formal analogies,

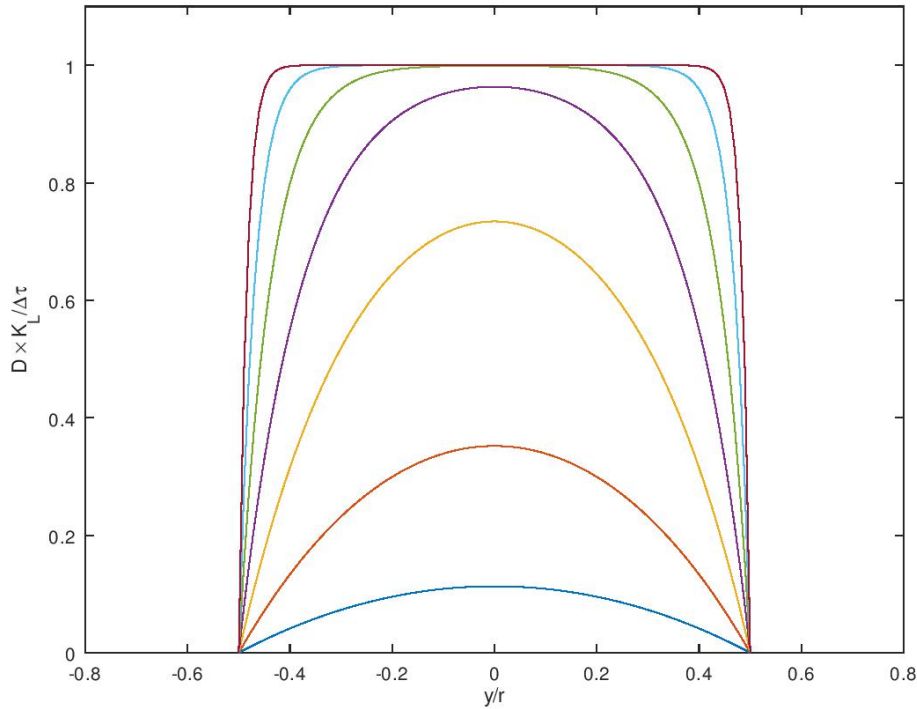$$\bar{\mathcal{K}}_L = \frac{\mu_d}{2h}, \tag{K.15}$$

Figure K.1: Static slip profiles for ruptures with uniform stress drop $\Delta\tau$ in a continuum Burridge-Knopoff model, with loading stiffness K_L. Each curve is for a different value of κr in $\{1, 2, 4, 8, 16, 32, 64\}$, from bottom to top.

$$\bar{\mathcal{K}} = \frac{\mu_d h}{6}. \tag{K.16}$$

Figure K.2a shows the LVFZ kernels (Eq. J.9) for various damage levels and their BK-like approximation (Eq. K.14). Figure K.2 shows their ratio as a function of normalized wavenumber kh and for all damage levels Δ above 0.5. The bandwidth over which the two kernels agree expands with increasing damage.

Under the conditions described above, the similarity between the LVFZ and BK kernels implies a formal analogy between the two models, which we now exploit to develop implications on pulse-like rupture. Eqs. (K.15) and (K.16) give $\kappa = \sqrt{3}/h$. The condition $\kappa r \gg 1$ for a flat, pulse-like slip profile in the BK model becomes, for the LVFZ model, $r \gg h/\sqrt{3}$. Under that condition and assuming a uniform stress drop $\Delta\tau$, a LVFZ produces ruptures with the flat slip profile characteristic of pulses and average slip of

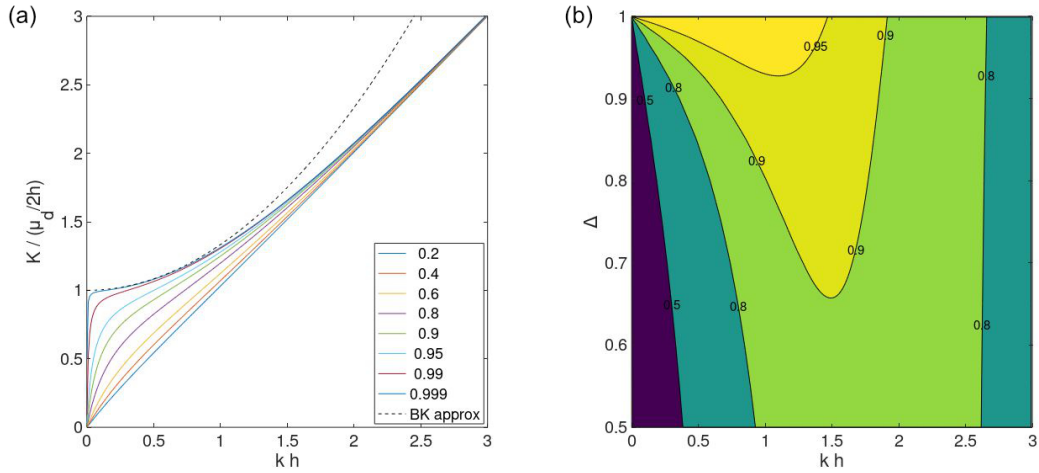$$\mathcal{D} \approx \frac{\Delta\tau}{\bar{\mathcal{K}}_L} = \frac{2h\Delta\tau}{(1-\Delta)\mu}. \tag{K.17}$$

Figure K.2: Comparison of LVFZ and BK static stress transfer kernels. (a) LVFZ kernels for a range of damage levels Δ (see legend) and their BK approximation (dashed) as a function of normalized wavenumber kh. Kernels are normalized by $\mu_d/2h$. (b) Ratio between LVFZ kernels and their BK-like approximation, as a function of kh and damage level Δ. The bandwidth over which the two kernels agree expands with increasing damage (see for instance the contours 0.9 and 0.95).

In the low-frequency regime defined by $\tanh(h|k|) \ll 1 - \Delta$, the LVFZ is too narrow to have an effect on the stress transfer, and the kernel tends to that of a homogeneous medium,

$$\mathcal{K}(k) \approx \frac{1}{2}\mu|k|. \tag{K.18}$$